EXPERIMENTAL AND THEORETICAL STUDIES IN PLANETARY AERONOMY

F. F. Marmo

GCA CORPORATION
Bedford, Massachusetts

FINAL REPORT
CONTRACT NO. NASw-1726

PREPARED FOR
NATIONAL AERONAUTICS AND SPACE ADMINISTRATION
HEADQUARTERS
WASHINGTON, D. C.

July 1970

GCA-TR-70-8-N

EXPERIMENTAL AND THEORETICAL STUDIES IN PLANETARY AERONOMY

By F. F. Marmo

GCA CORPORATION
GCA TECHNOLOGY DIVISION
Bedford, Massachusetts

FINAL REPORT

Contract No. NASw-1726

July 1970

Prepared for
NATIONAL AERONAUTICS AND SPACE ADMINISTRATION
HEADQUARTERS
WASHINGTON, D.C.

TABLE OF CONTENTS

I. INTRODUCTION

This Final Report summarizes the work performed under Contract No. NASw-1726 for the period 24 May 1968 through 24 November 1969. The overall problems associated with the physics of planetary atmospheres and the broad variety of scientific areas which have been considered are discussed most conveniently under the following major categories:

Experimental Studies
Theoretical Studies

During the performance of the subject contract, a number of reports were generated which have been submitted and/or accepted and/or published in accredited journals. In some cases, a more detailed discussion of the material is available in the form of published GCA Technical Reports. In any event, the pertinent information concerning the journal publication is presented below for each of the categories previously cited.

A. Experimental Studies

"Primary Processes in the Photolysis of SO_2 at 1849Å," P. Warneck, et al. J. Chem. Phys. 72, 3736 (1968).

"Photoelectron Spectroscopy of the Rare Gases," J. Samson, et al. Phys. Rev. 173, 80 (1968).

"Scattering Cross Sections of Argon and Krypton in the VUV," J. Samson, et als. J. Opt. Soc. Am. 58 (1968).

"Photo-Attenuation Cross Sections of Xe and Xe_2 between 1050 and 1550Å," Shardanand. J. Quant. Spectrosc. Radiat. Transfer 8, 1373 (1968).

"Angular Distributions of Photoelectrons and Partial Photoionization Cross Sections," J. Samson. Proc. Roy. Soc.(in press).

"Absorption Cross Sections of Minor Constituents in Planetary Atmospheres from 1050 - 2100Å," J. A. R. Samson, GCA Technical Report No. TR-69-7-N.

"Angular Distribution of Photoelectrons," J. Samson. J. Opt. Soc. Am. 59 (1969).

"Conversion Table for Wavelengths to eVs and cm^{-1}," J. Samson. GCA Technical Report No. TR-69-2-N.

"Formation of N_4^+ in Nitrogen," P. Warneck. J. Geo. Res. 74, #1, 1396 (1969).

"Higher Ionization Potentials of Nitric Oxide," J. A. R. Samson. Phys. Letters, 28A, #5, 391 (1968).

"Simultaneous Photoexcitation and Photoionization of Helium," J. Samson Phys. Rev. Letters 22, 693 (1969).

"Vacuum Ultraviolet Absorption Cross Sections of CO, HCℓ, and ICN between 1050 and 2100Å," J. Myer and J. Samson. J. Chem. Phys. 52, 266 (1970).

"Heats of Formation of CHO^+ and $C_3H_3^+$ by Photoionization," C. Matthews and P. Warneck. J. Chem. Phys. 51, 854 (1969).

"Absorption Cross Section and Photoionization Yield of I_2 between 1050 and 2200Å," J. Myer and J. Samson. J. Chem. Phys. 52, 716 (1970).

"Photon Scattering by Argon in the VUV," R. Cairns, F. Marmo and J. Samson. J. Opt. Soc. Am. 60, 211 (1970).

"Electronic States of $C_6H_6^+$ (J. Samson) Chem. Phys. Letters 4, 247 (1969).

"Line Broadening in Photoelectron Spectroscopy," Rev. Sci. Instr. 40, 1174 (1969).

"On the Measurement of Rayleigh Scattering," J. Samson. J. Quant. Spectroscopy and Radiative Transfer 9, 875 (1969).

B. Theoretical Studies

"The Effect of Oxygen Cooling on Ionospheric Electron Temperatures," A. Dalgarno, et al. Planet. & Space Sci. 16, #11, 1371 (1968)

"Dipole Properties of Molecular Hydrogen," G. A. Victor and A. Dalgarno J. Chem. Phys. 50, #6, 2535 (1969).

"Mariner 6: Origin of Mars Ionized Carbon Dioxide Ultraviolet Spectrum," A. Dalgarno, T. Degges, and A. Stewart. Science 167,#3924, 1490 (1970).

"Electron Impact Excitation of the Dayglow," A. Dalgarno. J. Atmos. Sci. 26, #4, 753 (1969).

"CO_2^+ Dayglow on Mars and Venus," A. Dalgarno and T. Degges. Proc. I.A.U. Symposium 40 on Planetary Atmospheres, Marfa, Texas(October 27, 1969).

"Carbon Atoms in the Upper Atmosphere of Venus," F. F. Marmo and A. Engelman, ICARUS 12, 128-130 (1970).

II. SUMMARY OF TECHNICAL WORK PERFORMED FOR THE PERIOD 24 MAY 1968 THROUGH 24 NOVEMBER 1969

The technical progress accomplished under the program is described in the present section in two general categories: (A) experimental studies and (B) theoretical studies. Each major category in turn is presented in two subsections, namely (1) published data, and (2) unpublished data. The first category contains all data which have been published in the open literature and are available to the interested reader. Accordingly, in these cases the actual published abstracts are repeated in the present section for general information and scientific content. The category of unpublished data contains descriptions of the studies performed which have not as yet appeared in the open literature. Accordingly, in these cases, it is considered appropriate to offer more detailed discussions since the data are not readily available elsewhere.

A. Experimental Studies

Published Data.

"Heats of Formation of CHO^+ and $C_3H_3^+$ by Photoionization"

C. Matthews and P. Warneck

Journal of Chemical Physics, 51, #2, 854 (1969)

The ions CHO^+ and $C_3H_3^+$ occur with significant yields in the mass spectra of many oxygenated and unsaturated hydrocarbons, respectively, so that their heat of formation is of general interest. A particular need for the thermochemical properties has arisen from observations indicating that CHO^+ and $C_3H_3^+$ are major ions in the chemi-ionization of hydrocarbon flames (Refs 1-3). For a specification of the detailed reaction sequences generating these ions, reliable values for their heat of formation are required.

"Formation of N_4^+ in Nitrogen"

P. Warneck

Journal of Geophysical Research, Space Physics
74, #1, 396 (1969)

This paper is concerned with the discrepancies reported in the literature over the preceding 15 years on N_4^+ formation in nitrogen, specifically, whether the process

$$N_2^+ + N_2 \rightarrow N_4^+$$

is a two body or a three body recombination process. Reports by Fite, et al. (Ref. 4) Saperoschenko (Ref. 5), Varney (Ref. 6), and Kovar, et al. (Ref. 7)

had indicated a two body process, whereas the more recent data by Warneck (Ref. 8) and Asundi, et al. (Ref. 9) displayed third order kinetics. The photoionization mass spectrometer technique established by Warneck (Ref. 10) should give straightforward results, but to counter a criticism voiced by Varnet (Ref. 11) new experiments were performed. The ionizing radiation used in these experiments was centered at 790Å, close to the threshold of N_2 ionization, in order that the formation of vibrationally excited N_2^+ ions was precluded. Previous experiments had been performed with 764Å radiation.

Rate coefficients for N_4^+ formation were determined in one series of experiments in which the ratio of electric field strength to pressure, E/P, in the reaction region was held constant for several field strengths and pressures; and in another series of experiments, the pressure was varied while the field strength was held constant but differed for each set of values. All observations showed a pressure dependence of the derived bimolecular rate constant similar to that found previously (Ref. 10) thereby demonstrating third order kinetics. Moreover, the third order rate coefficients derived from all these experiments agree within the experimental error, the value being $k = (4.4 \pm 0.6) \times 10^{-29}$ cm^2/molecule^2 sec. Thus, the variation with pressure is due to the influence of third body and not due to a variation in E/P in the region of field strengths covered ($8 < E/P < 33$ volts/cm torr).

"On the Measurement of Rayleigh Scattering"

J.A.R. Samson

J. Quant. Spectrosc. Radiat. Transfer 9, 875(1969)

The general expression for the angular distribution of Rayleigh scattered radiant energy from a gas is developed for the case of partially plane polarized incident radiant energy. It is shown that, if measurements are made at specific angles, then both the total scattering cross section and the normal depolarization factor can be determined without knowing the degree of polarization of the incident radiant energy.

"Line Broadening in Photoelectron Spectroscopy"

J.A.R. Samson

Review of Scientific Instruments 40, #9, 1174 (1969)

The factors causing line broadening in photoelectron spectroscopy are discussed. Experimental results are given for the half-width of the 584Å helium line emitted from a variety of sources. Typical half-width values lie between 1 and 6.5 mV, which corresponds to 0.027 and 0.18Å, respectively.

Curves are presented showing the contribution of the thermal motion of the photoionized gas to the spread in the energy of the ejected photoelectrons.

"Electronic States of $C_6H_6^+$"

J.A.R. Samson

Chemical Phys. Letters 4, #5, 257 (1969)

The photoelectron energy spectrum of benzene has been measured with monochromatic radiation of wavelengths between 1253 and 584Å. The first two ionization potentials are shown to be 9.25 and 11.5 eV. Explanations are given which account for previously observed structure lying between the first two ionization potentials.

"Simultaneous Photoexcitation and Photoionization of Helium

J.A.R. Samson

Physical Review Letters 22, #14, 693(1969)

The probability of simultaneously photoexciting and photoionizing helium has been measured near threshold at a wavelength of 186Å. It was found that about 8 $\pm$ 2 percent of the ions formed at that wavelength were excited into the n = 2 state.

"Angular Distribution of Photoelectrons"

J.A.R. Samson

Journal of the Optical Society of America 59,#3,356(1969)

Transition probabilities for transitions from the ground state to the ionic state of atoms or molecules can be determined by using the technique of photoelectron spectroscopy. This technique measures the kinetic energy of the ejected photoelectrons and the relative numbers of these electrons within each energy group. Knowing the relative numbers of electrons in each group and the total photoionization cross section at a specific wavelength we can obtain the transition probabilities at that wavelength. However, it is important to obtain the true representation of the relative numbers of electrons within each energy group.

"Higher Ionization Potentials of
Nitric Oxide"

J.A.R. Samson

Physics Letters 28A,#5, 391 (1968)

Higher ionization potentials of nitric oxide are reported using the technique of photoelectron spectroscopy. Previously unreported ionization potentials of 21.72 and 23.1 eV were observed.

"Vacuum Ultraviolet Absorption Cross Sections of CO, HCℓ, and ICN Between 1050 and 2100Å"

J.A.R. Samson

Journal of Chemical Physics 52, #1, 266 (1970)

Absorption cross sections have been measured under intermediate resolution (0.25Å) for CO, HCℓ, and ICN in the spectral region from 1050 to 2100Å. An attempt has been made to analyze the spectra in terms of the reactions responsible for the observed features. A Rydberg series has been identified in the absorption spectrum of ICN with a series limit of 1140.6 ± 0.1Å.

"Photoelectron Spectroscopy of the Rare Gases"

J.A.R. Samson

Physical Review 173, #1, 80 (1968)

A spherical retarding potential analyzer was used to measure the kinetic energies of electrons ejected by photoionization of the rare gases as a function of wavelength from the $^2P_{1/2}$ ionization threshold down to about 400Å. The ratio of the number of ions produced in the ground $^2P_{3/2}$ state to the number produced in the excited $^2P_{1/2}$ state was found to be constant with respect to wavelength and had the following values: 2.18, 1.98, 1.79, and 1.60 for Ne, Ar, Kr, and Xe, respectively. From these data the specific photoionization cross sections for the rare gases were obtained. At wavelengths shorter than the M_1, N_1, and O_1 thresholds for Ar, Kr, and Xe, respectively, the ejection of s-electrons was observed and the specific cross sections for their production measured.

"Absorption Cross Section and Photoionization Yield of I_2 Between 1050 & 2200Å"

J.A.R. Samson

Journal of Chemical Physics 52, #2, 716 (1970)

The total absorption cross section and photoionization yield of molecular iodine were measured from 1050 to 2200Å. Two thresholds were observed in the photoionization yield curve. The first was associated with the ion-pair production $I^+ + I^-$ and the second to direct ionization of I_2. From the appearance potential for ion-pair production and the accurate ionization potential of I_2 it was possible to calculate the value of the electron affinity of iodine, namely, 3.073 ± 0.014 eV.

"Primary Processes in the Photolysis of SO_2 at 1849Å"

J. N. Driscoll and P. Warneck

Journal of Physical Chemistry 72, 3736 (1968)

The production of SO_3 in the 1849Å photolysis of pure SO_2 and in mixtures containing 5-75 percent SO_2 in O_2 was studied at atmospheric pressure. An interference filter isolated the 1849Å-1924Å lines from a mercury arc and eliminated the emission at longer wavelengths. The quantum yield found for SO_3 formation in pure SO_2 was 0.50 ± 0.07. The addition of oxygen increased the SO_3 quantum yield to a plateau value of 1.04 ± 0.13, but for mixtures containing less than 30 percent SO_2 the quantum yield declined again. The photodecomposition of SO_2 at 1849Å is complicated by the occurrence of several primary processes including direct dissociation due to an absorption continuum, excited SO_2 molecule formation, and predissociation. The observed SO_3 quantum yield was utilized to evaluate the relative importance of the various primary processes.

"Photon Scattering by Argon in the Vacuum Ultraviolet"

R. Cairns, F. Marmo & J. Samson

Journal of the Optical Society of America 60, #2, 211 (1970)

Scattering cross sections were measured with the method of Gill and Heddle, but with dispersed incident flux. These measurements constitute a sensitive test for the presence of rare-gas quasimolecules. The ratio of Ar_2 to Ar at 100 torr was deduced to be 8.6×10^{-5}. At 1090Å the molecular cross section is estimated to be 1.6×10^{-18} cm^2. The attenuation cross section is 8.0×10^{-18} cm^2.

Unpublished Data.-"High Resolution Quantitative Absorption Data of Minor Constituents in Planetary Atmospheres." The fact that high-resolution data are of significant importance in isolating the contribution due to minor constituents in a planetary atmosphere has been amply demonstrated in the infrared spectra of planetary atmospheres. For certain specific cases, similar potential exists in the VUV region so long as the appropriate data are available. For example, it is propitious to perform measurements in those vacuum ultraviolet (VUV) spectral regions where the minor atmospheric constituent displays a cross section which far exceeds all others associated with the major constituents. These features can be even more easily isolated if the absorption features are discrete. Performance of this laboratory task is facilitated by employing a new special McPherson vacuum monochromator which GCA has recently acquired. A description of the salient features and the performance capabilities of this monochromator is included in the discussion below.

During the current period , the general experimental capability of obtaining VUV high resolution spectra was investigated. For these preliminary measurements, two gases were examined, namely methane and benzene. The results of these investigations are given below.

The monochromator is a McPherson model No. 225 which is a one-meter normal incidence instrument equipped with a 1200-ℓ/mm grating. The monochromator is capable of resolving 0.2Å in the first order. Attached to the exit slit of the monochromator is a double-beam system which consists of a wedge shaped mirror oscillating a 6 cps. The radiations from the monochromator strikes each face of the wedge at a grazing angle and is reflected into a reference and a sample cell. The surfaces of the wedge are concave which focuses the radiation into the absorption cells and prevents loss of light due to a diverging beam (see Figure 1). The cells are completely enclosed with LiF windows in front and in back of the cells. After passing through the cells, the radiation impinges onto sodium salicylate screens converting the vacuum UV radiation into near UV radiation centered around 4100Å. This radiation is then detected by two matched photomultipliers. The most important and difficult problem is the matching up of the two pairs of LiF windows in both the reference and sample cells. Once this has been achieved, the log-ratio of the output signals of the two photomultipliers is proportional to the total absorption cross section of the gas in the sample cell.

The McPherson log-ratiometer is skillfully designed to allow log-ratios to be made with the many-lined spectrum of H_2. In order to facilitate the ratioing of rapidly varying intensities over several orders of magnitude in intensity, the unit first takes the signal i_r and i_f from the reference and sample-cell photomultipliers, respectively, and feeds the signals into a time sharing log amplifier. The outputs of the log amplifier (log i_r and log i_f) are then fed into a difference amplifier giving an output

$$\log i_r - \log i_f = \log (i_r/i_f)$$

That is, the output gives the logarithm to the base ten of the ratio (i_r/i_f), (See Figure 2) which is related to the total absorption cross section as follows:

$$\sigma = \frac{2.303}{nL} \log (i_r/i_f),$$

where n is the number density of the gas in the sample cell and L is the length of the sample cell.

Preliminary results:

The total absorption cross sections of methane and benzene have been measured from 1100 to 2100Å. The results are shown in Figures 3, 4, & 5.

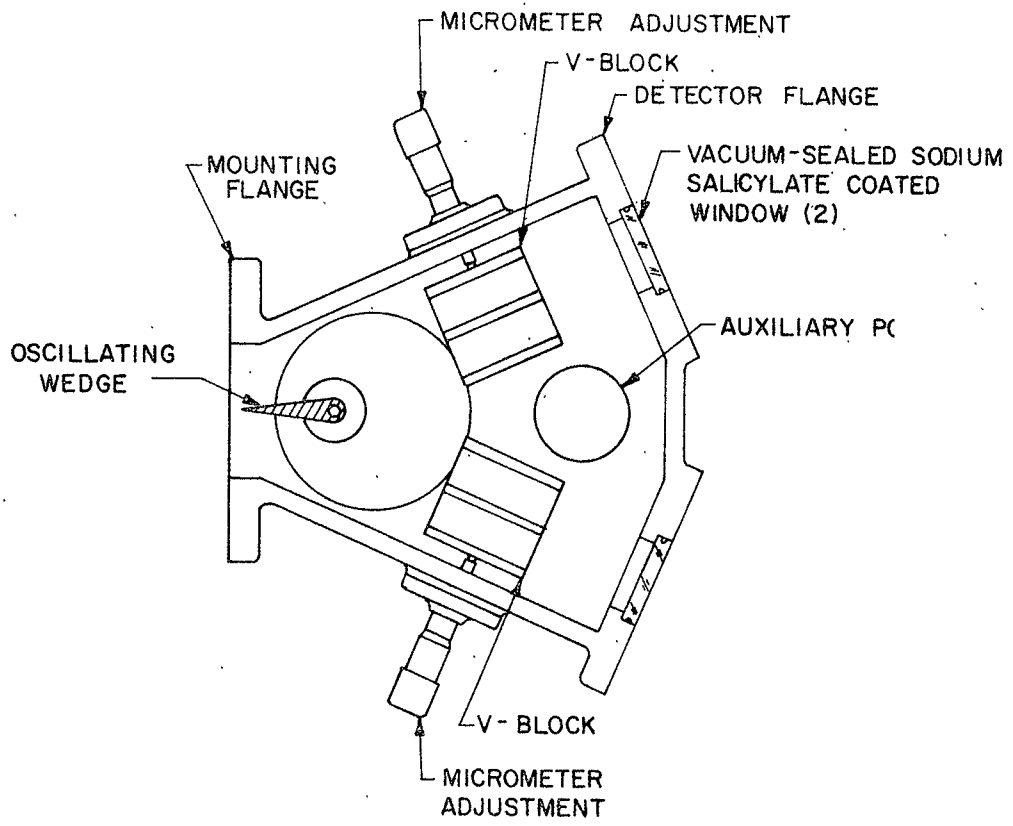

Figure 1. Diagram of double beam absorption cell housing

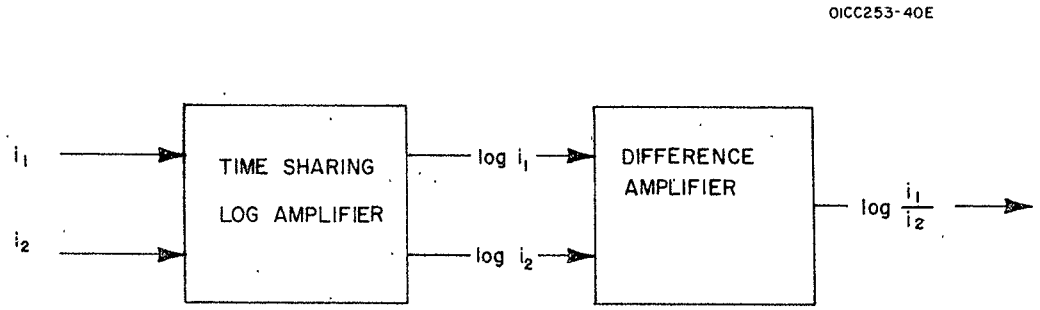

Figure 2. Block diagram of logarithmic ratiometer circuit.

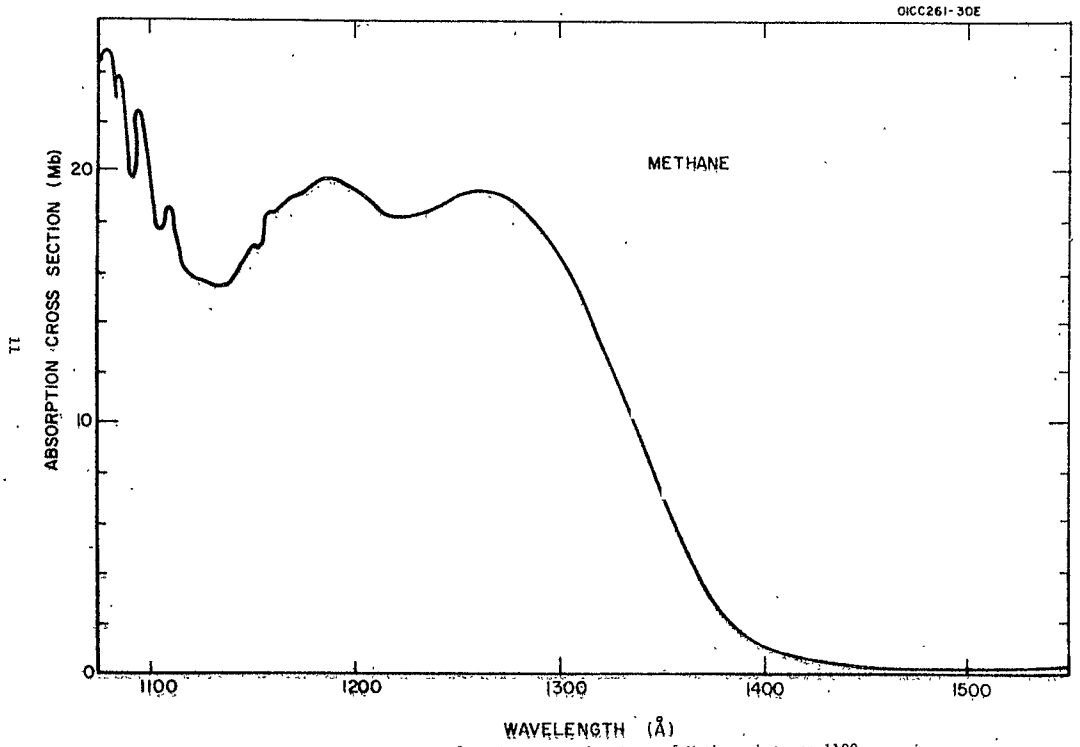

Figure 3. Absorption Spectrum of Methane between 1100 and 1500Å.

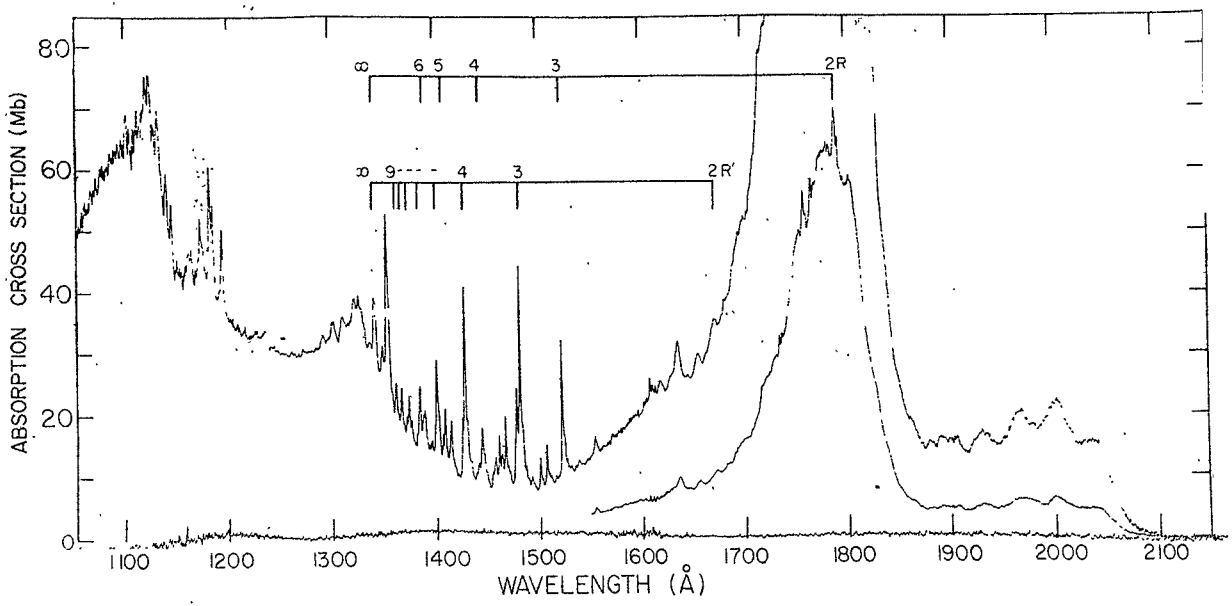

Figure 4. Absorption Spectrum of Benzene between 1100 and 2100Å.

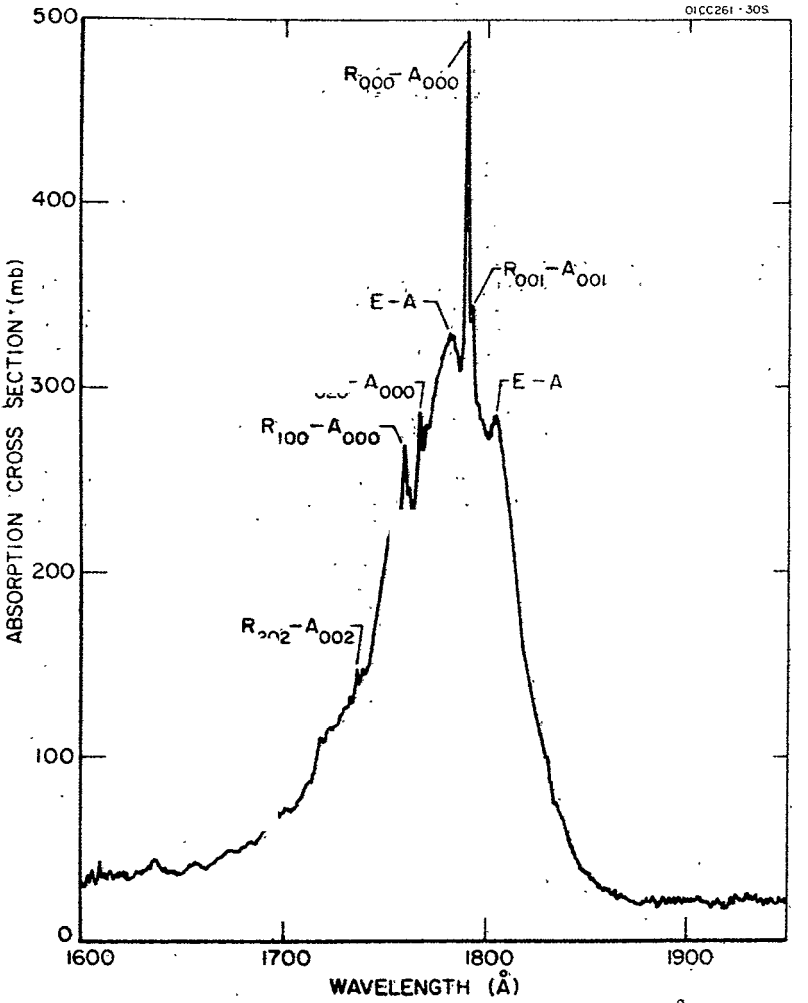

Figure 5. Absorption spectrum of Benzene between 1600 and 1900Å.

Methane

The only previous cross-sectional data which exists in the spectral region for methane is that of Sun and Weissler (Ref. 12) and of Watanabe, et al. (Ref. 13). Weissler's data has a long-wavelength limit of 1300Å and furthermore was taken at only a few points with a line spectrum. Thus, the data of Watanabe, et al. in 1953 represents the only comparable data with the presently reported results. However, their wavelength resolution was only 1Å whereas the present data was obtained with a resolution of 0.45Å. Watanabe's absolute cross sections agree with the present results over most of the wavelength region. However, the present data resolves structure below 1125Å, which they could not observe. With the exception of this structure, the absorption of methane is continuous from about 1450Å to shorter wavelengths. No absorption was observed between 1450Å and 2100Å.

Benzene

The benzene spectrum has been studied thoroughly by Wilkinson (Ref. 14) using photographic techniques at high resolution. However, total absorption cross sections have only been made in a few isolated wavelength regions or else made at low wavelength resolution. The present data shown in Figures 4 and 5 shows considerable detailed absorption structure not readily seen with poor resolution. In Figure 4, two Rydberg series, denoted at R and R', can be seen leading up to the first ionization potential of benzene at 1340Å

"Drift Velocity Measurements for Atmospheric Ions." In the course of investigating drift velocities of N_2^+ ions formed by photoionization of nitrogen, it was found that when the ionizing wavelength was 790Å, the observed drift velocities were in excellent agreement with data obtained by other experimenters using techniques different from ours; however, when the spectral setting of the monochromator was 764Å, the drift velocities observed were by about a factor of two greater. Simultaneously, the ion density profile observed on the screen of the oscilloscope was no longer symmetric, but became skewed, indicating the presence of two groups of ions with different velocities. At the wavelength setting of 790Å (close to the threshold of N_2^+ formation) only ground state N_2^+ ions can be generated. At 764Å excitation to the first vibrational level is also possible. This channel would be significant if an appreciable fraction of the ions were formed by autoionization. The observation that two groups of ions are involved at 764Å makes evident that autoionization is significant and that N_2^+ ($v = 1$) ions are endowed with a higher mobility than N_2^+ ($v = 0$) ions.

The formation of N_4^+ occurs at both wavelengths. The rate coefficient for this reaction had been measured previously with the photoionization

technique at 764Å. Third body kinetics were observed. This observation has been criticized as being inconsistent with a number of other data in the literature. In view of the participation of N_2^+ ($v = 1$) ions at 764Å it was considered necessary to re-investigate the process of N_4^+ formation at 790Å where only ground state N_2^+ ions are initially present. The details of the results and their implications are given in the present section in the form of a paper submitted for publication in the Journal of Geophysical Research.

In a recent comment concerning a discussion (Ref. 8) of atmosphere ion neutral reaction rates, Varney (Ref. 6) objected to listing the formation of N_4^+ via the association

$$N_2^+ + N_2 \rightarrow N_4^+ \qquad (1)$$

as a three body reaction, and he cited experimental results which indicated that it proceeds as a two-body process. Specifically, the after glow data of Fite, et al. (Ref. 4), the mass spectrometer results of Saporoschenko (Ref. 5), and variety of drift experiments (Refs. 6, 7, 15) have indicated a direct two-body association whereas the more recent photoionization mass spectrometer experiments by Warneck (Ref. 10) and the low pressure electron impact mass spectrometer observations by Asundi, Schulz, and Chantry (Ref. 9) displayed third order kinetics. Since the discrepancy is serious, we have performed a new set of experiments with the photoionization technique, following the suggestions by Varney (Ref. 11) that the parameter E/p, the ratio of the electric field strength to the pressure, be kept constant in the ion source so that the energy of the reacting ions remains unchanged. The new results and their implications are the topic of this note.

Initially, the former results with constant E and varying p were verified, using for the production of N_2^+ radiation centered at 764Å, as described previously (Ref. 10). Since this permits the production of vibrationally excited nitrogen ions, the new experiments were performed at 790Å, near the threshold of nitrogen ionization, where the formation of excited nitrogen ions is precluded. At 790Å the measured drift velocities of N_2^+ agreed well with those reported in the literature (Refs. 15, 16) whereas the drift velocities at 764Å were by a factor of two higher, presumably due to the presence of a considerable portion of vibrationally excited nitrogen ions formed by autoionization. Rate coefficients for N_4^+ formation were determined at 790Å in a series of experiments for which E/p was held constant for various field strengths and pressures; and in another series of experiments for which the pressure was varied while the field strength was held constant but differed for each set of values. All observations showed a pressure dependence of the derived bimolecular rate constant similar to that found previously (Ref. 10), thereby demonstrating third order kinetics. Moreover, the third order rate coefficients derived from all

these experiments agree within the experimental error, the value being $k = (4.4 \pm 0.6) \times 10^{-29}$ $cc^2/molecule^2$ sec. Accordingly, the variation with pressure is due to the influence of the third body and not due to a variatior with E/p in the region of relative field strengths covered ($8 < E/p < 33$ volt/cm/torr). The new results, therefore, corroborate our previous conclusion that for the conditions employed in the photoionization mass spectrometer an equilibrium between N_2^+ and N_4^+ is not established.

The ionizing energies employed here in photoionizing nitrogen are in a region where corresponding electron impact experiments have demonstrated N_4^+ formation from neutral excited nitrogen via the process:

$$e + N_2 \rightarrow N_2^* + e \qquad (2)$$

$$N_2^* + N_2 \rightarrow N_4^+ + e \qquad (3)$$

occurring in addition to N_4^+ formation from N_2^+ (Refs. 9, 17).

In view of the knowledge that in the wavelength region 658Å - 850Å the absorption spectrum of nitrogen is at least partially discrete, and that photoionization efficiencies are less than unity, the formation of excited nitrogen molecules is certain to occur also in the present experiments. Although the excited states reached by UV radiation and by electron impact are not necessarily the same, it is clear that allowance must be made for the possibility of reaction (3) participating in the photoionization mass spectrometer experiments. However, no experimental evidence has been found for any occurrence of the process. Specifically, no N_4^+ formation was detected at energies below (i.e. at wavelengths above) the onset of the N_2^+ formation -- in contrast to the electron impact results, and approximately the same rate of N_4^+ formation as at 790Å was observed when the wavelength was set to 685Å, where the ionization efficiency is nearly unity. Thus, while reaction (3) cannot be entirely precluded, it does not appear to occur to a significant extent in the present experiments. It is concluded that the observed formation of N_4^+ is due predominantly to reaction (1) in its termolecular mode, in agreement with our earlier conclusion (Ref. 10).

There remains to explain the discrepancy arising from the various data in the respect to third or second order kinetics of N_4^+ formation. Evidently, this problem is connected with the observation that at high E/p values N_4^+ ions gain sufficient energy in the field to dissociate upon collision. Mass spectrometrically identified ion transients in drift tubes are nearly identical for N_2^+ and N_4^+ when E/p is high, demonstrating that a rapid equilibrium between the two species is achieved (Refs. 15, 16). In low feilds, however, the two ion transients are well separated even though a significant $N_2^+ - N_4^+$ conversion occurs. In this region, therefore, a

rapid interchange is not operative. The low field region is well suited to studies of reaction (1) and in this region, the formation of N_4^+ is third body dependent. On the other hand, in the high field region, reaction (1) is in equilibrium with the dissociation of N_4^+, so that in this case, the abundance of N_4^+ will depend only linearly on the nitrogen pressure. It appears that in those cases where bimolecular N_4^+ formation was deduced (Refs. 4,5,15) the high field conditions favored equilibration of N_2^+ and N_4^+. The mass spectrometer results of Asundi, Schulz and Chantry (Ref.9) provide direct evidence for such an interpretation.

"VUV ($\lambda\lambda$ 1050-2000Å) High Resolution Absorption Cross Section Data with Emphasis on Minor Constituents in Planetary Atmospheres." With reference to the statement of work under this contract, Task Item #3 has been completed. The VUV absorption cross sections have been measured for a number of gases that represent possible atmospheric constituents. In most cases high resolution absorption spectra have not been heretofor obtained in this spectral range, in spite of the fact that such data are directly applicable to the determination of planetary atmospheric constituency. For example, such data could be of particular value in those spectral regions where the absorption properties of the major constituents are relatively weak and/or constant whereas the minor constituents display strong discrete absorption features due to resonance bands, Rydberg series, etc. In addition, high resolution VUV absorption data are important in the interpretation of the physical mechanisms responsible for the absorption processes. For example, such data provide information which can define the produce radical of a given photodissociation, the energy distribution of the products, the possibilities of their reacting with other species to form new products, etc. These investigations were accomplished with a McPherson Model 225 one-meter VUV scanning monochromator equipped with a McPherson 630 VUV light source. The optical features are described elsewhere (Ref. 18) so that they are not repeated here. However, the unique feature of the experimental arrangement is the employment of a McPherson Model 665 double beam attachment that was incorporated with the monochromator.

The unique feature of the present experimental arrangement is a McPherson Model 665 double beam attachment that was incorporated with the monochromator. This attachment has two optical paths with identical absorption cells (one is a reference cell) and a vibrating mirror that alternately reflects the dispersed light beam through each cell. The alternating signals are measured by two independent photomultiplier tubes (EMI 9635 B with sodium salycylate coatings) and the logarithm of the ratio of the two signals as evaluated by a logarithmic ratiometer and then registered on a linear strip chart recorder. If a known gas pressure is introduced into one of the absorption cells whose length is accurately known, then the absorption cross section in units of cm^2 can be determined directly from the recording.

For this technique to be most effective, it is necessary for the optical paths including the window transmissions of the cells to be as identical as possible at all wavelengths considered. When the optical paths are properly balanced then one will obtain a smooth horizontal base line for effective zero cross section when there is no absorbing gas in either cell.

The gases and vapors to be studied were introduced and controlled with a gas filling system which included a needle leak valve, a diffusion pump and several vapor traps, a McLeod gauge, a thermocouple gauge (0-100 microns), and an oil monometer for pressures up to 30 torr. Vapors were introduced through a double stopcock-flask arrangement on the same system. The gas pressures for the cross section measurements were read with the oil monometer over the range from 0.05 torr - 30.00 torr ($\pm$ 0.05 torr) which was adequate for most of the measurements.

The gases investigated included CO, NH_3, CH_4, NO, SO_2, H_2O, CO_2, O_2, $HC\ell$, I_2 and ICN; the resultant data are shown in Figures 6-19 inclusive.

The data on the several gases shown in the figures have been discussed, analyzed, and interpreted in terms of the applicability to atmospheric physics in a GCA technical report, i.e. GCA TR 69-7-N by James A. R. Samson and James Myer. The interested reader can consult the cited reference so that it is unnecessary to include any further discussion on these investigations.

"Ion Molecule Reactions in Hydrocarbon Systems." From spectroscopic observations, it is known that the Jovian planets contain appreciable amounts of methane and ammonia in their atmospheres, in addition to hydrogen and helium. McNesby (Ref. 19) recently has studied the photochemistry of such a system and has shown that, with hydrogen in excess, the first order photodissociation products of methane and ammonia essentially recombine, resulting in no net change of the system except to heat the atmosphere. Nevertheless, a small amount of higher hydrocarbons would be formed as a second order perturbation. For example, Sagan (Ref. 20) has argued for the formation of adenine and other amino products. With this background, it becomes of interest to investigate ion reactions involving hydrocarbons. A great number of such reactions has been studied in the past with conventional electron impact mass spectrometers. With the applied techniques, these investigations have been complicated by the many ions produced simultaneously in the ion source, and their reactions with the parent gas. It appears, that the photoionization mass spectrometer technique, by virtue of the selective ionization processes involved, can reduce the complexities of the reaction system sufficiently to allow a less ambiguous analysis of the data.

On this basis, we have studied ion reactions in the systems ethylene-acetylene, acetylene-methane and methane-ethylene. The results have already lead to some interesting conclusions, although all the data have not yet

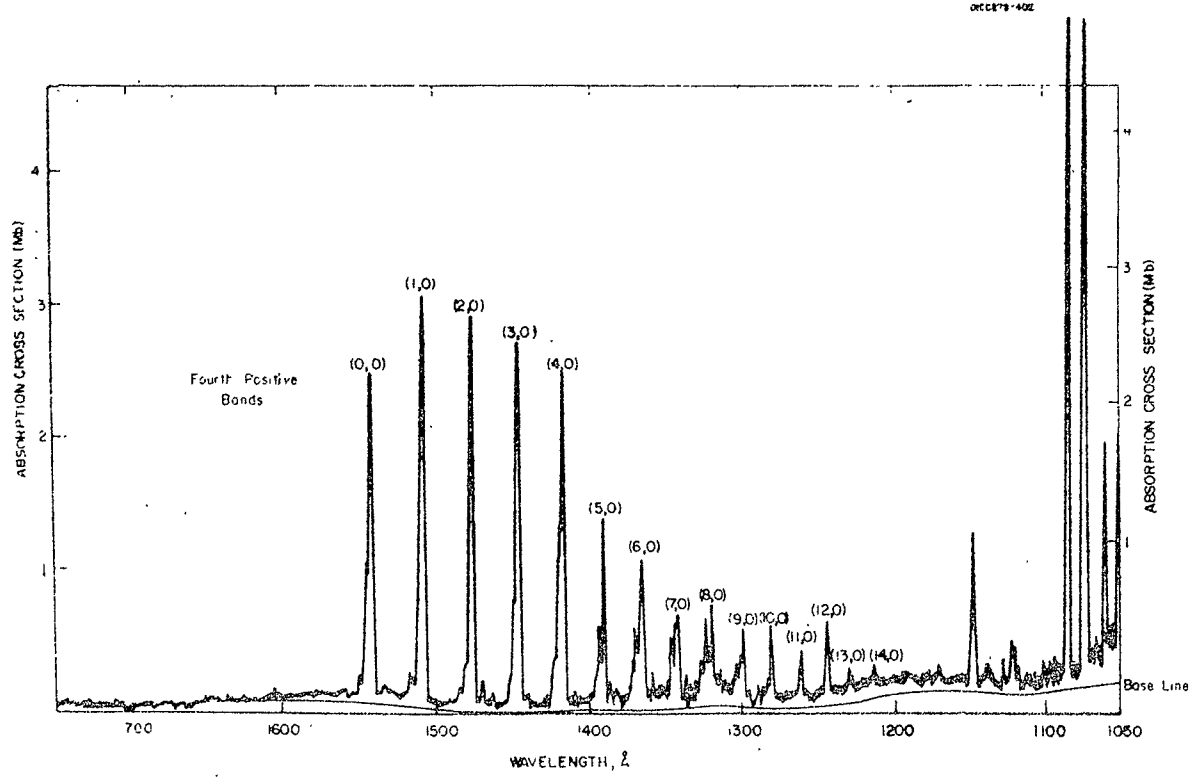

Figure 6. Absorption cross section of CO as a function of wavelength between 1750Å and 1050Å.

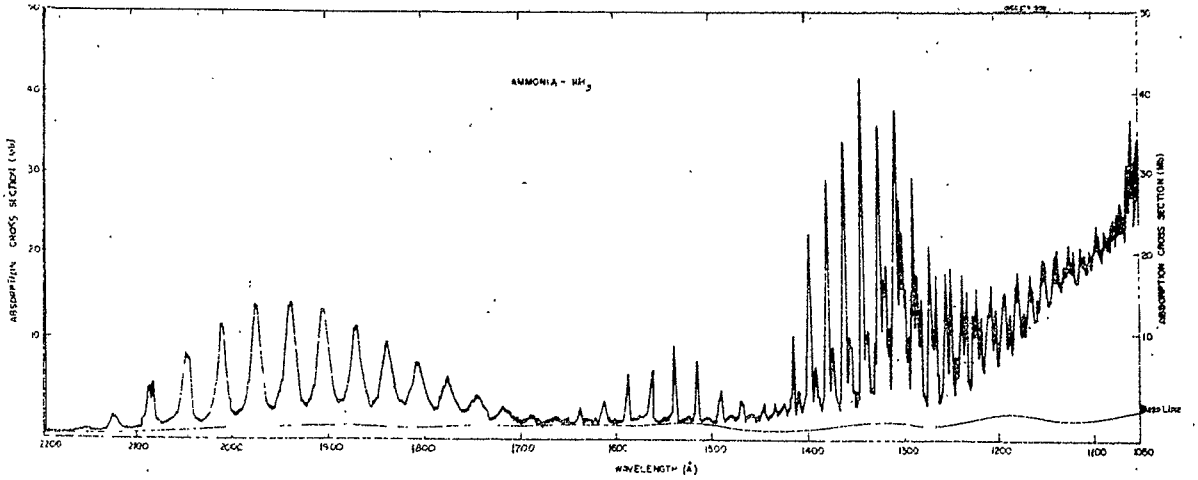

Figure 7. Absorption cross section of NH_3 as a function of wavelength between 2200Å and 1050Å.

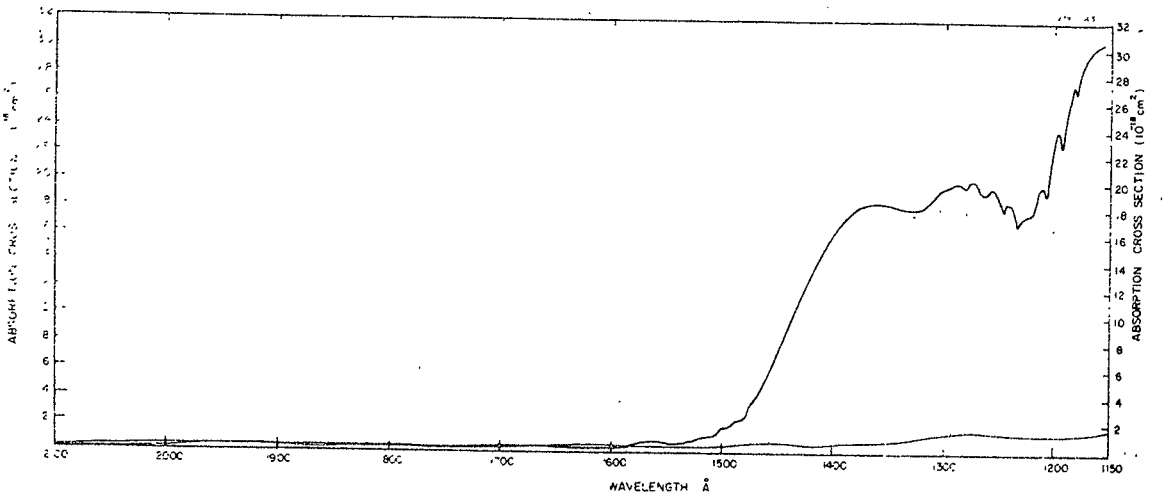

Figure 8. Absorption cross section of CH_4 as a function of wavelength between 2100 and 1050Å.

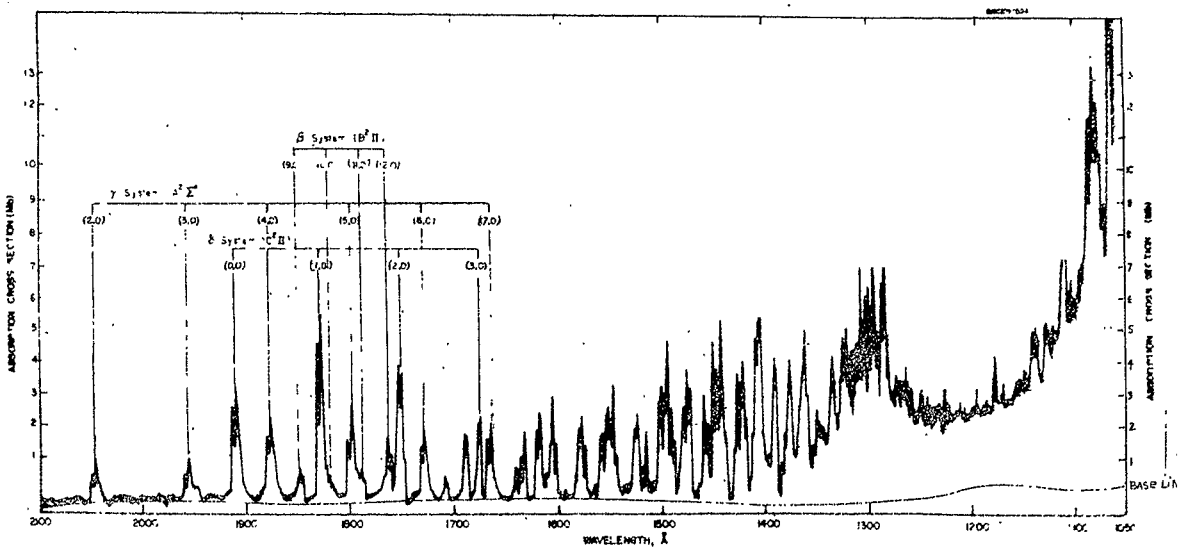

Figure 9 . Absorption cross section of NO.

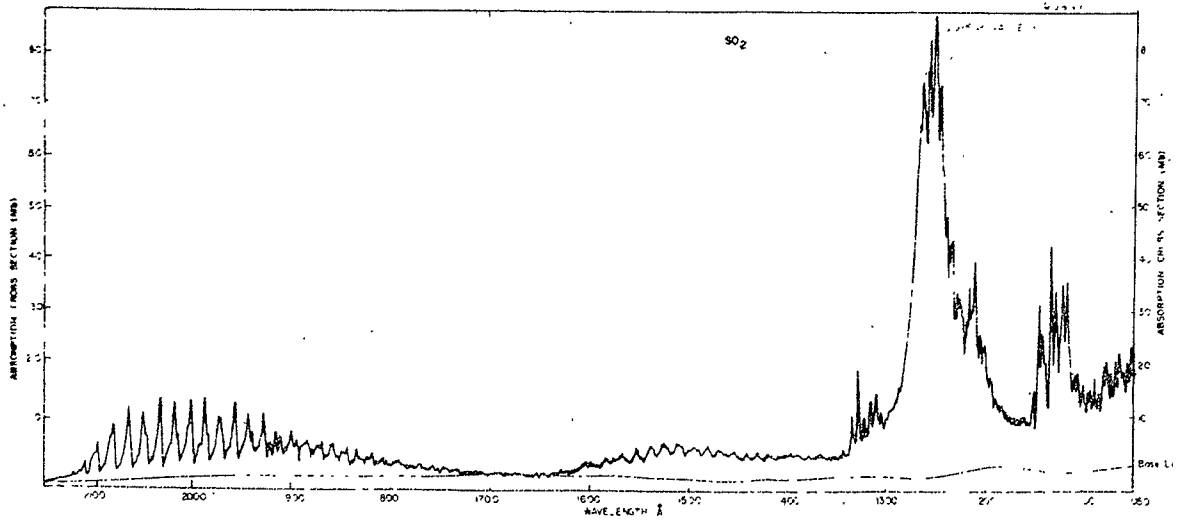

Figure 10. Absorption cross section of SO_2.

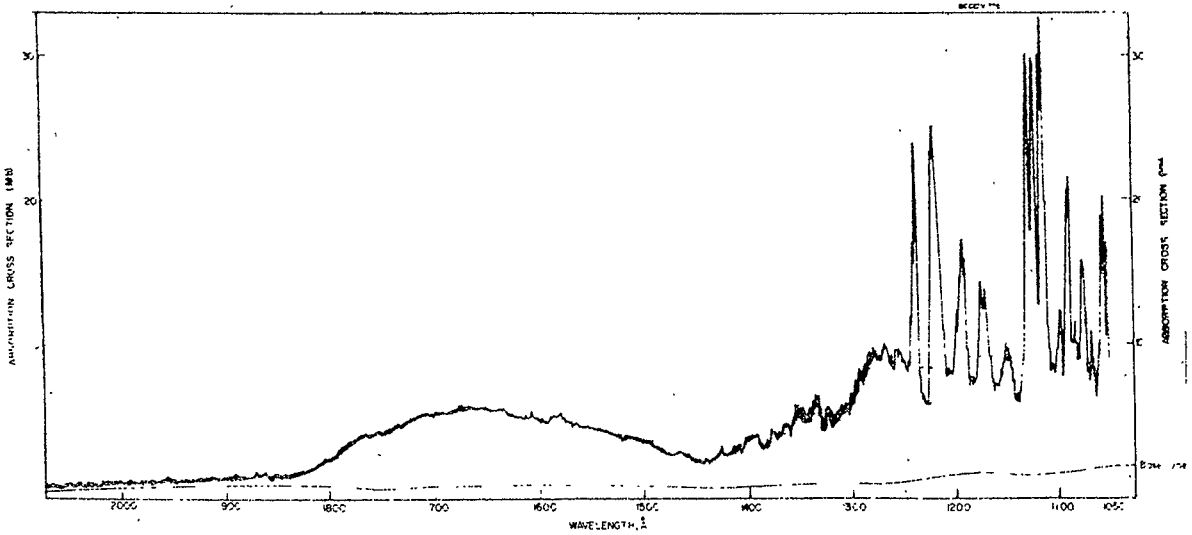

Figure 11. Absorption cross section of H_2O.

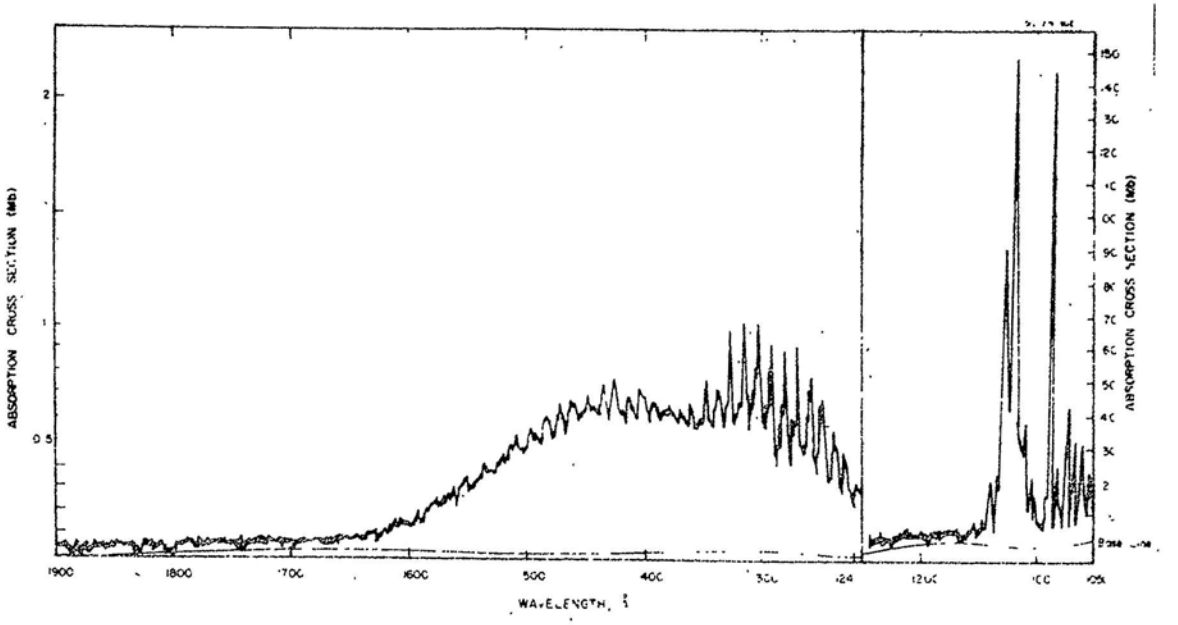

Figure 12. Absorption cross section of CO_2 as a function of wavelength between 1900Å and 1050Å.

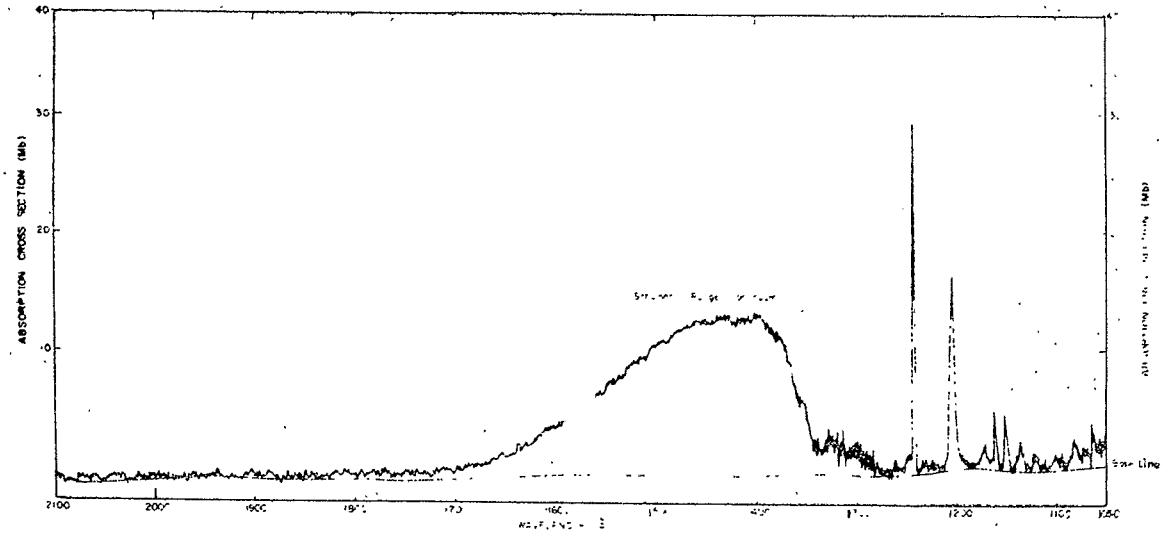

Figure 13. Absorption cross section of O_2 as a function of wavelength between 2100 and 1050Å.

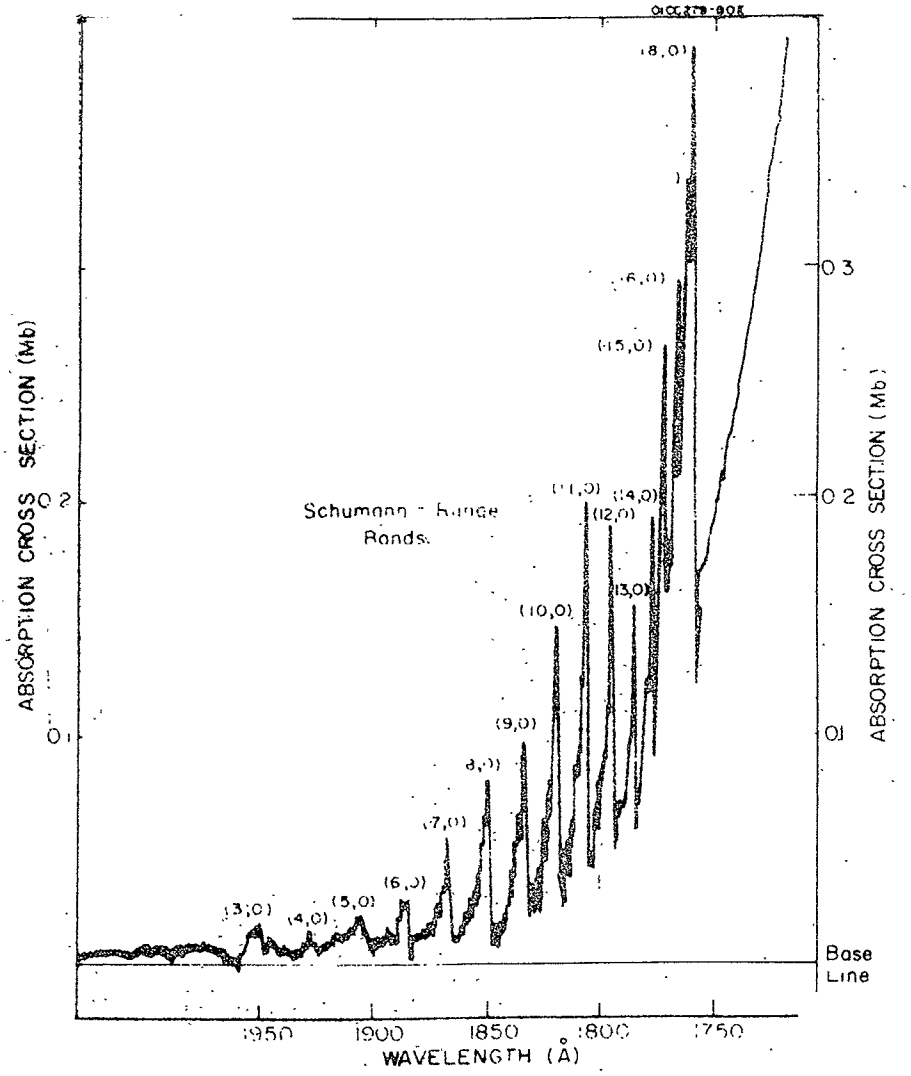

Figure 14. Absorption cross section of O_2 as a function of wavelength between 2000 and 1750 Å.

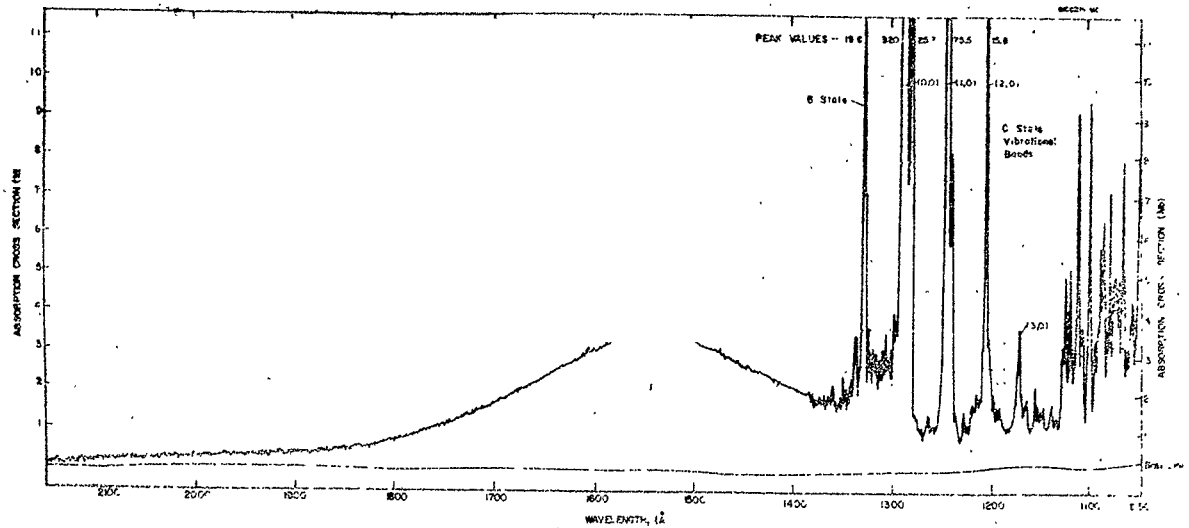

Figure 15. Absorption cross section of HCℓ as a function of wavelength between 2100Å and 1050Å.

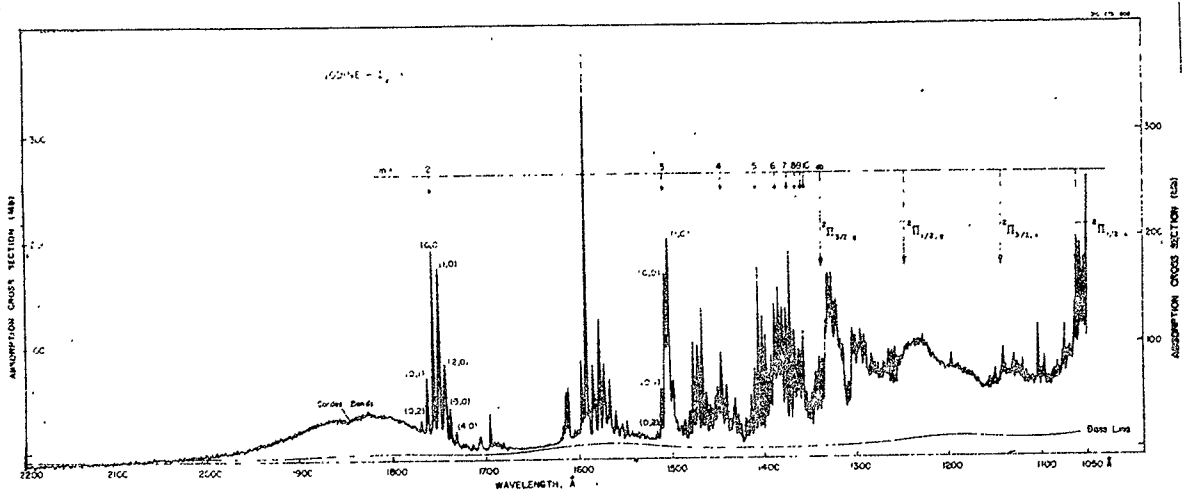

Figure 16. Absorption cross section of I_2 as a function of wavelength between 2200Å and 1050Å.

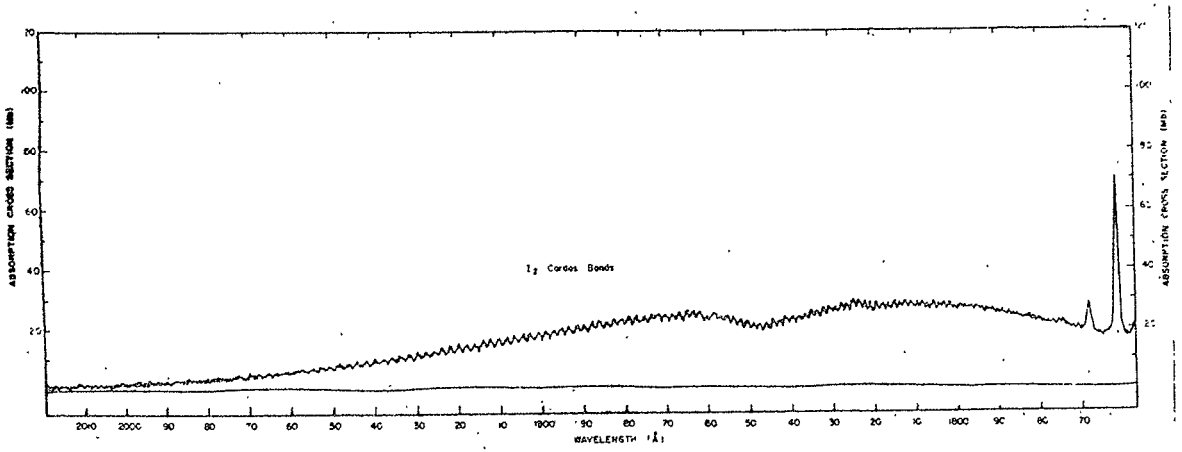

Figure 17. Absorption cross section of I_2 as a function of wavelength between 2020Å and 1760Å.

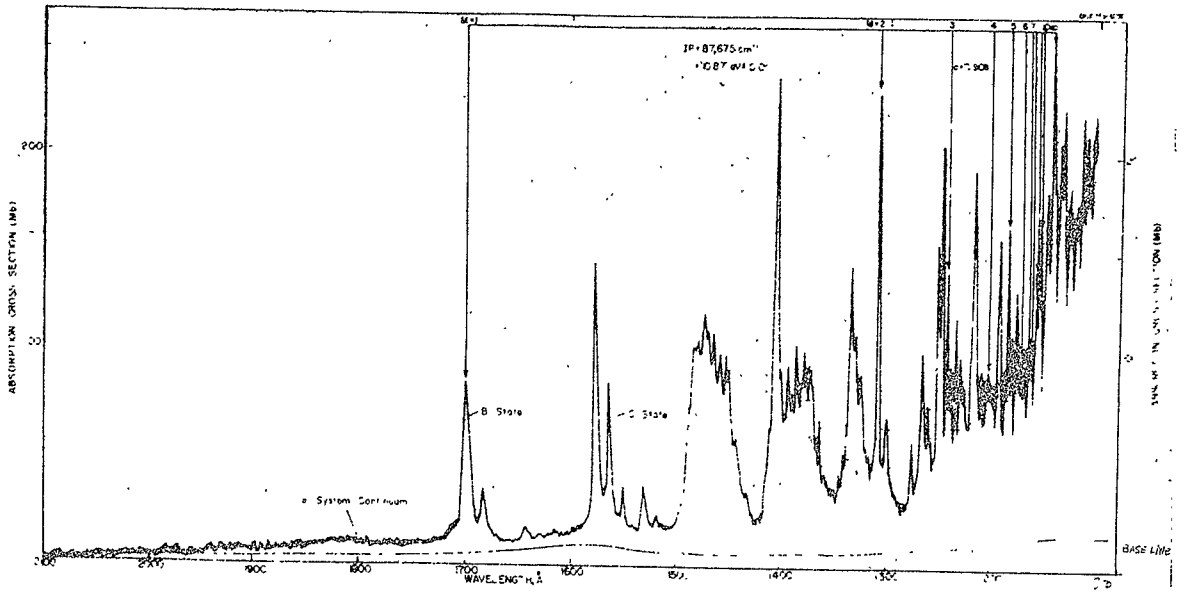

Figure 18. Absorption cross section of ICN as a function of wavelength between 2100 and 1100Å.

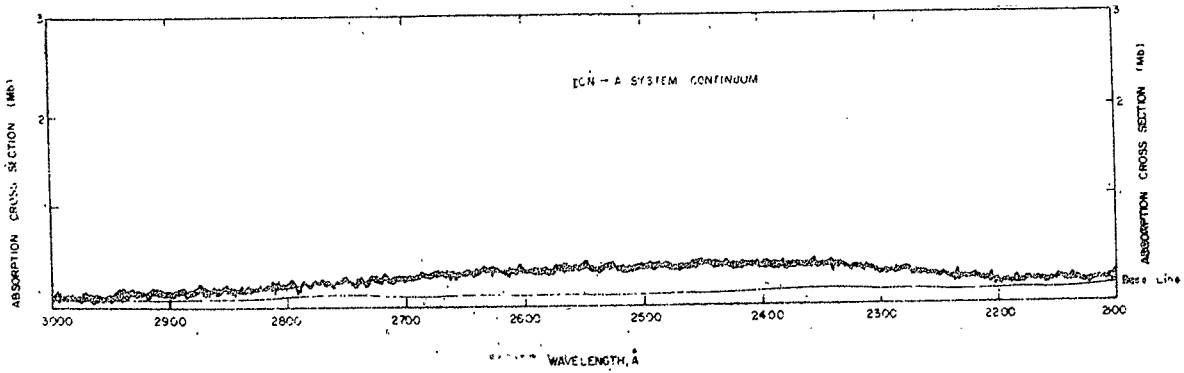

Figure 19. Absorption cross section of ICN as a function of wavelength between 3000 and 2100Å.

been analyzed, and a detailed evaluation of those data which have been analyzed has not yet been possible. The results presently available, and their implications will be discussed below.

The techniques employed in this study have been described in detail previously (Ref. 21). Briefly, the apparatus involved a 180 degree magnetic mass spectrometer with conventional ion source geometry and electronic multiplier. Ions are produced by extreme UV radiation generated in a repetitive spark light source. A Seya monochromator provides wavelength isolation with a spectral resolution of about 5Å. The light beam transversed the ion chambe midway between the repeller plate and the ion exit orifice which were placed 0.6 cm apart. The repeller potential was one volt. The gas pressure in the ion source was measured with a McLeod gauge through the hollow stem of the repeller.

Reactions were investigated in the low pressure domain where the motion of ions is mainly acceleration in the repeller field. Products were assessed from the appearance of new peaks as the pressure in the ion chamber was raised. Rate coefficients were determined from the decrease of the primary ion intensity as a function of the gas pressure, or as a function of the partial pressure of an added second gaseous component; and from the residence time of the primary ions in the source chamber. Residence times were determined from the time delay of the ion pulse arriving at the mass spectrometer collector after the deposition of ions in the source by the light pulse. As described previously, delay times were measured for several repeller potentials and a graphical extrapolation toward infinite repeller potential is used to separate the ion source residence time from the total flight time of the ions in the mass spectrometer. In the present experiments the half-rise time of the integrated ion pulse was utilized for reference in the delay time measurements so that averaged residence times were obtained.

In the following, results will be presented for ion-molecule reaction in ethylene, acetylene, and their mixtures. At ionizing wavelengths above 945Å up to the ionization threshold, the primary photoionization products in both ethylene and acetylene are the parent ions $C_2H_4^+$ and $C_2H_2^+$, respectively, and other ions are formed only by secondary reactions of these ionic species. In the wavelength region 900-945Å, photoionization of acetylene still yields only the parent ion, whereas that of ethylene produces $C_2H_2^+$ in addition to $C_2H_4^+$. This latter wavelength region thus facilitates a study of the reactions of $C_2H_2^+$ with ethylene in the absence of interference by acetylene. The present investigation made use of radiation at 1087Å and 923Å both provided by operating the spark source with nitrogen.

The development of the ion spectrum with pressure when acetylene is ionized at 1087Å is shown in Figure 20. The important product ions appear at mass numbers 50, 51, and 52. The reaction paths responsible for the production of these ions are

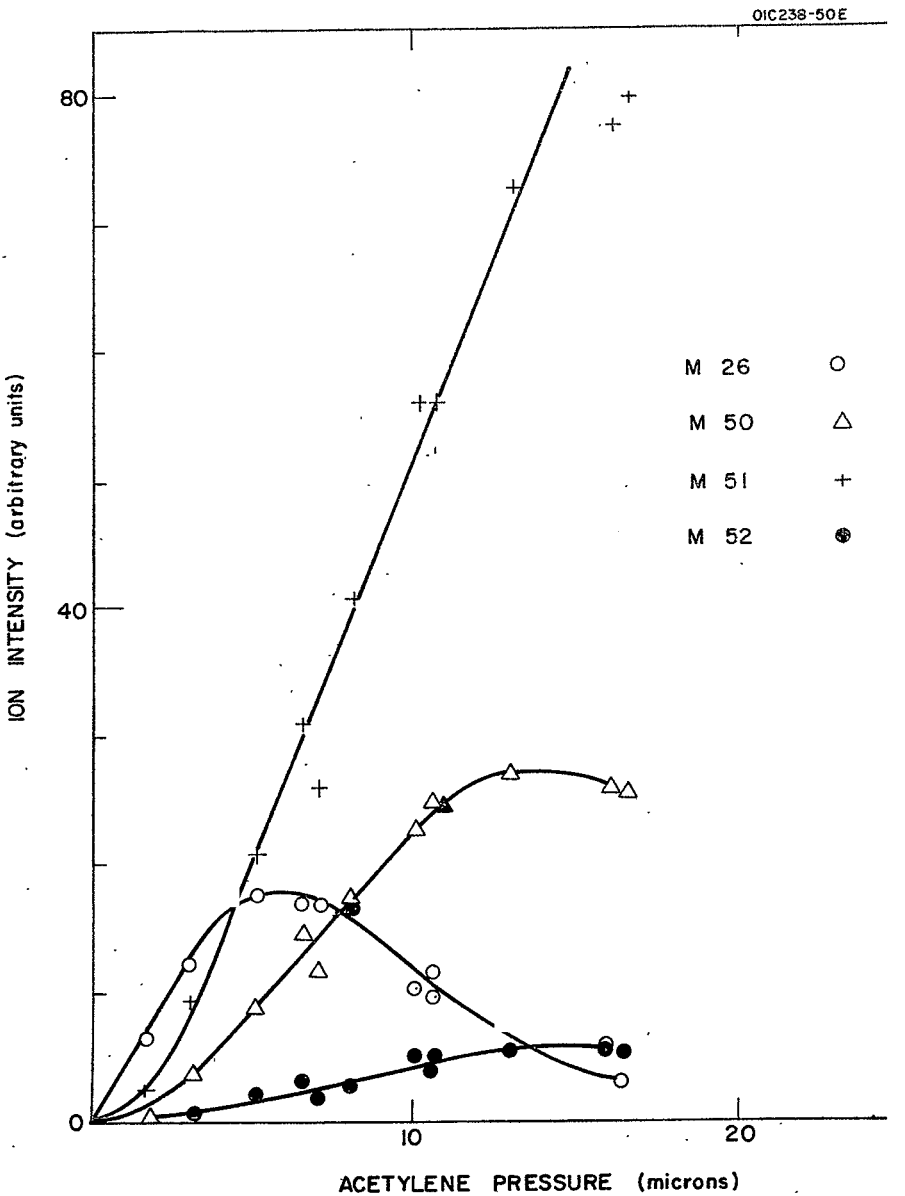

Figure 20. Intensities of major ions in acetylene as a function of pressure
Ionizing wavelength 1087Å.

$$C_2H_2^+ + C_2H_2 \rightarrow C_4H_2^+ + \text{products} \qquad (4)$$
$$\rightarrow C_4H_3^+ + \text{products}$$
$$\rightarrow C_4H_4^+$$

At pressures below 10 microns, the product ratios are found to be constant. The determination of the average values for the branching ratios of reaction (4) gave 29 percent for the formation of $C_4H_2^+$, 66 percent for $C_4H_3^+$ and 5 percent for $C_4H_4^+$. The pressure dependence for the formation of the last ion is such that it precludes the participation of the third collision partner. The formation of $C_4H_4^+$ in a binary collision is possible only if the lifetime of the intermediate collision complex is sufficiently long, so that the collision complex is stabilized by subsequent collisions regardless of the pressure. Since the produce branching ratio does not depend on the pressure, it must further be concluded that the other two products result from the same process as $C_4H_4^+$. Thus, the detailed mechanism of reaction (4) in the investigated pressure domain can be written as

$$C_2H_2^+ + C_2H_2 \rightarrow C_4H_4^{+*} \qquad (4a)$$

$$C_4H_4^{+*} + C_2H_2 \rightarrow C_4H_2^+ + C_2H_4^* \qquad (4b)$$
$$\rightarrow C_4H_3^+ + C_2H_3^*$$
$$\rightarrow C_4H_4^+$$

where the asterisk denotes (vibrationally) excited species. The present results contain no information on the fate of the neutral products in reaction (4b), but a possible course is their dissociation to yield H_2 or H and acetylene.

At pressures greater than 10 microns, the ratio of products M50/M51 decreases and new ions appear at mass numbers 74, 75 and 76 due to the reactions

$$C_4H_2^+ + C_2H_2 \rightarrow C_6H_2^+ + H_2 \qquad (5)$$
$$\rightarrow C_6H_3^+ + H$$

$$C_4H_3^+ + C_2H_2 \rightarrow C_6H_3^+ + H_2 \qquad (6)$$
$$\rightarrow C_6H_4^+ + H$$

of these, reation (5) predominates, producing $C_6H_2^+$ and $C_6H_3^+$ ions in approximately equal amounts. The sum of all the observed ion intensities, i.e. that of the acetylene and that of the various product ions, was found directly proportional to the acetylene pressure, indicating that reactions (4) through (7) account for essentially all the ions observed and further reactions are negligible. The rate coefficient for reaction (4) including all its channels can be derived from the decrease of the $C_2H_2^+$ ion intensity as a function of pressure from the relation

$$k = \frac{2.3}{\tau\, n} \log \frac{N_o}{N}$$

where τ is the average residence time of $C_2H_2^+$ in the ion source, n the number density of acetylene in the source, N_o is the sum of all ions taken equal to the initial $C_2H_2^+$ ion intensity and N is the measured $C_2H_2^+$ ion intensity. The average value of the rate coefficient thus determined for reaction (4) is $k_1 = 1.39 \times 10^{-9}$ cc/molecule sec. The value expected on the basis of the ion induced dipole interaction theory is k_1 (theor.) = 1.29×10^{-9} cc/molecule sec. The experimental rate coefficient is found to agree with the theoretical one within experimental error.

Similar results were obtained for ion reactions in acetylene when the photoionizing wavelength was 923Å. Again, $C_2H_2^+$ was the only primary ion observed, and reaction (4) with its three channels was the major loss process for $C_2H_2^+$. The ratio of product channels was determined as $C_4H_2^+$ 29 percent, $C_4H_3^+$ 67 percent, $C_4H_4^+$ 4 percent. Within experimental error, these values are the same as those given above for the reaction when working with 1087Å radiation. Moreover, the associated rate coefficient was found to be $k_1 = 1.38 \times 10^{-9}$ cc/molecule sec. This value agrees well with the value given above, and like that one is in accord with theoretical prediction. These results, therefore, show that the acetylene ion formed at 923Å behaves identically to that formed at 1087Å, even though it may be produced with some internal excitation.

The development of the spectrum of the major ions with pressure when ethylene is ionized at 1087Å is shown in Figure 21. The significant product ions appear at mass numbers 41 and 55. They are due to the reaction

$$\begin{aligned} C_2H_4^+ + C_2H_4 &\rightarrow C_3H_5^+ + CH_3 \\ &\rightarrow C_4H_7^+ + H \end{aligned} \qquad (7)$$

The branching ratio of this reaction is found to result to 90 percent in $C_3H_5^+$ ions, and to 10 percent in $C_4H_7^+$ ions. At pressures above about 10 microns, this ratio is perturbed by the strong increase of a tertiary product at mass 69 due to the condensation reaction

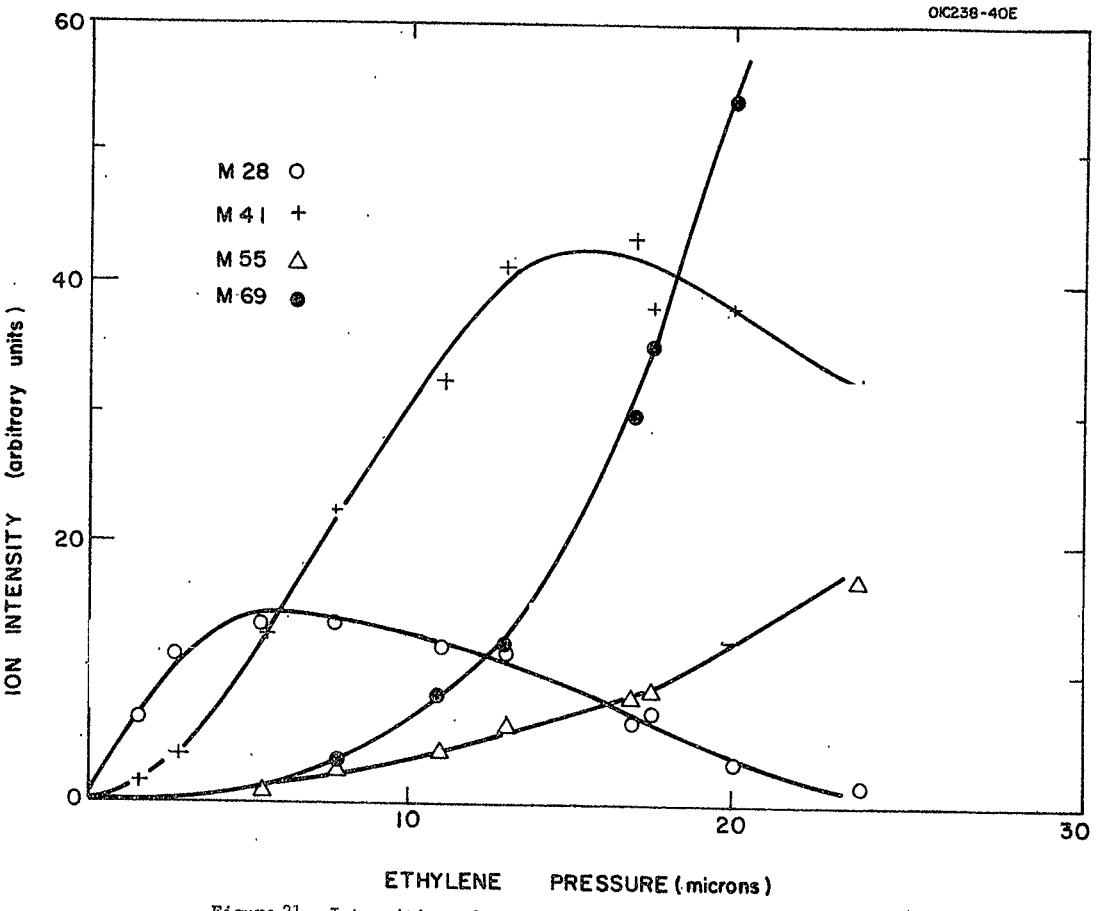

Figure 21. Intensities of major ions in ethylene as a function of pressure. Ionizing wavelength 1087Å.

$$C_3H_5^+ + C_2H_4 \rightarrow C_5H_9^+ \qquad (8)$$

which consumes the $C_3H_5^+$ ions formed in Reaction (4). The $C_4H_7^+$ ion formed in the reaction (Ref. 22) also undergoes further reactions but these are significant only at pressures greater than 30 microns and even then their contribution to the total ion abundance is small. Contributions to the total ion spectrum were observed also on mass numbers 42 and 70, but they were too small to be taken into account in a meaningful way. However, they are observed with higher intensity in the photoionization of ethylene at 923Å and will be discussed further below.

As in acetylene, an association product, $C_4H_8^+$, was found in the photoionization of ethylene. However, compared to the behavior at the mass 54 ion in acetylene, the association product in ethylene showed a different pressure dependence. Figure 22 indicates that the ratio of the intensity of the mass 56 ion to the total product ion intensity is not constant but increases with pressure. The dependence on pressure is linear and the straight line obtained extrapolates to the origin of the plot. This is evidence that in contrast to the acetylene case, the association product of the ethylene ion is formed by a third body reaction

$$C_2H_4^+ + 2\ C_2H_4 \rightarrow C_4H_8^+ + C_2H_4 \qquad (9)$$

The rate coefficient for reaction (7) was determined from the decay of the $C_2H_4^+$ ion intensity compared to the total ion intensity. A value of $k_4 = 1.24 \times 10^{-9}$ cc/molecule sec was obtained. The rate coefficient calculated from the induced dipole measurement theory is $k_4(\text{theor.}) = 1.29 \times 10^{-9}$. As for the previous cases, the agreement between the experimental and the theoretical values is good. From the rate coefficient associated with reaction (7) and the data shown in Figure 22, the rate coefficient for reaction (9) can be derived as $k_6 = 1.5 \times 10^{-25}$ cc^2/molecule^2 sec. The magnitude of this value indicates that the average lifetime of the intermediate collision complex before it is stabilized by a third body collision is approximately 1×10^{-7} seconds. Since this rate coefficient is derived from a product intensity rather than the primary ion intensity decrease, is is probably not as reliable as the other rate coefficients. Nevertheless, the implied order of magnitude makes reaction (9) one of the most rapid termolecular ion reactions. Gordon and Ausloos, (Ref. 22) from studies of the photolysis of ethylene at 1048Å/66Å had concluded that formation of the butenes is due mainly to neutralization of the $C_4H_8^+$ ion produced by reaction (9).

Since the primary ions formed by photoionization of acetylene and ethylene with 1087Å radiation are only the parent ions of these gases, and their reactions have been established by the results reported above, it was of interest to look for additional reactions of these species in a mixture of ethylene and acetylene. Specifically, charge transfer from the

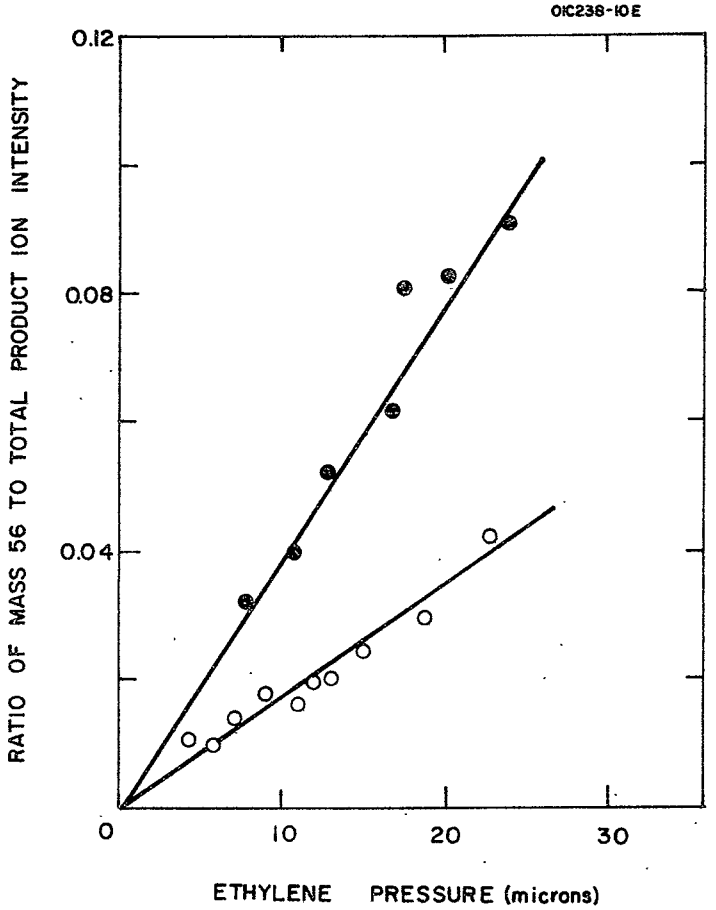

Figure 22. Ratio of Mass 56 ion intensity to total product ion intensity in ethylene as a function of pressure. Ionizing wavelength 1087Å: solid points; 923Å: open points.

acetylene ion to ethylene was expected to occur, as it is an exothermic process. In these experiments, therefore, acetylene was entered into the ion source chamber at a fixed rate providing a partial pressure of 3.8 microns, and ethylene was added in varying amounts at partial pressures up to 8 microns. In this pressure range, the ion intensities due to ethylene and its reaction products at mass number 28, 41 and 55 fitted well with the intensity curves shown in Figure 21 for pure ethylene so that the ethylene ions must react little or not at all with acetylene. The acetylene ion intensities, however, decreased considerably with increasing ethylene pressure as shown in Figure 23a indicating the occurrence of an interaction. At the same time new peaks appeared at mass numbers 39 and 53. Thus the reaction

$$C_2H_2^+ + C_2H_4 \rightarrow C_3H_3^+ + CH_3 \qquad (10)$$
$$\rightarrow C_4H_5^+ + H$$

is indicated. From the intensity distribution of the ions M39 and M53 the branching probability for reaction (10) was obtained as $C_3H_3^+$ 71 percent and $C_4H_5^+$ 29 percent. The sum of the intensities of these products matched the losses of the acetylene ions within the experimental error (see Figure 23a) so that reaction (10) must be the major reaction that acetylene ions undergo with ethylene. Several previous workers (Ref. 23) have concluded, however, that charge transfer is a major reaction channel. To investigate this problem further, the sum of the intensities of ions due to $C_2H_4^+$ and its interaction with ethylene are plotted in Figure 23b for ethylene in the presence of acetylene and for ethylene along. It is evident that both sets of data coincide, whereas if charge transfer took place to an appreciable extent, the total ethylene ion intensity should increase with increasing ethylene pressure. It may be agreed that the lack of an increase in the ethylene ion intensity is due to a reaction of these ions with acetylene and that charge transfer is operative nonetheless. The probability for this additional reaction would be greatest at low ethylene concentrations because then the concentration ratio of acetylene to ethylene is large. However, with increasing ethylene pressure the importance of this process diminishes in comparison with the interaction with ethylene, and the total ethylene ion intensity should increase correspondingly. From the failure to detect such an increase at the highest ethylene pressure involved ($C_2H_4/C_2H_2 = 2$), from the intensity losses of the acetylene ions, and from the corresponding increase of the M39 and M53 ion intensities shown in Figure 23a it is estimated that the charge transfer reaction

$$C_2H_2^+ + C_2H_4 \rightarrow C_2H_4^+ + C_2H_2 \qquad (11)$$

occurs to less than 15 percent of the overall reaction of acetylene ions.

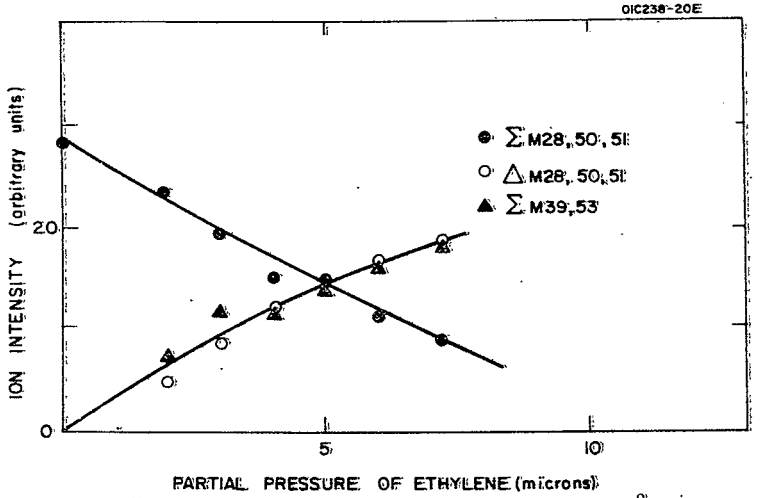

Figure 23. Photoionization of acetylene-ethylene mixture at 1087Å. Intensities of primary and product ions when ethylene is added to 3.8 microns of acetylene. (a): Loss of $C_2H_2^+$ and gain of $C_3H_3^+$ and $C_4H_5^+$ to show their equivalence. (b): Comparison of $C_2H_4^+$ and follow-on ions intensities (crosses) with those observed in pure ethylene (points) to show their equivalence.

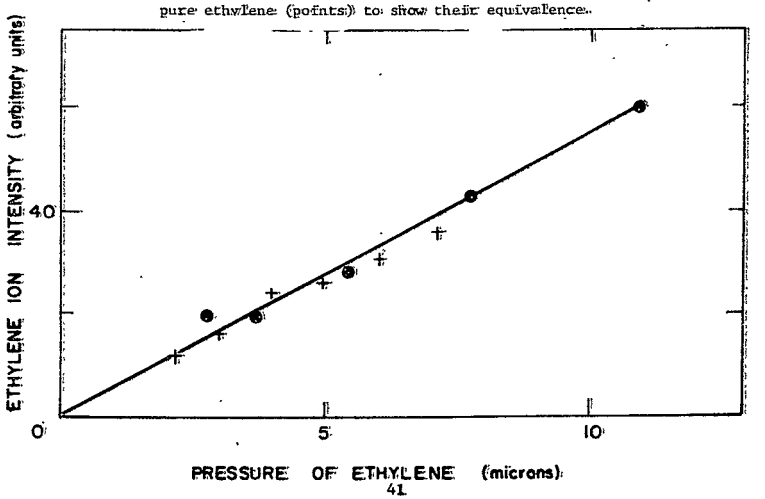

From the decrease of the $C_2H_2^+$ ion intensity as the ethylene pressure is increased and from the measured residence time of the acetylene ions in the source chamber, the rate coefficient for the reaction(10) and (11) combir is found to be $k_{7+8} = 1.35 \times 10^{-9}$ cc/molecule sec. The rate coefficient calculated from theory is k_{7+8} (theor.) $= 1.31 \times 10^{-9}$ cc/molecule sec. Withi the experimental error the values are identical.

When ethylene was photoionized with 923Å radiation, the major ion reactions were found to be reactions (7) through (10) discussed above, involving the primary ions $C_2H_4^+$ and $C_2H_2^+$. In accord with expectation the major product ions appeared at mass numbers 41, 55, 56, and 69, and at 39 and 53 respectively. However, some additional reactions occurred also, as evidenced by signals on mass numbers 27, 29, 40, 42, 54, 67 and 70. Although the contribution of these ions amounted to no more than 7 percent of the total ion intensity, their assignment is required for a complete interpretation of the results. The M67 ion is taken to be the condensation product of $C_3H_3^+$ with ethylene, because it was present also in the 1087Å photoionization of an acetylene-ethylene mixture when the ethylene pressure exceeded 10 microns. The behavior of most of the other ions identifies them as product ions. By analogy to reactions (7), (8) and (10), therefore, the signals on mass numbers 40 and 54 are assigned to products of M27, and the signals on mass numbers 42 and 70 are assigned to products of the ion M29. These assignments then reduce the problem of the minor ions to the origin of M27 and M29. The intensity of these ions and their follow-on products is much greater than the expected isotope contributions in ethylene (mainly due to C^{13}), so that the M27 and M29 ions must be identified as $C_2H_3^+$ and $C_2H_5^+$. They give rise to the reactions

$$\begin{aligned} C_2H_3^+ + C_2H_4 &\rightarrow C_3H_4^+ + CH_3 \\ &\rightarrow C_4H_6^+ + H \end{aligned} \qquad (12)$$

From the M40 and M54 contributions the branching ratio of this reaction is found to yield $C_3H_4^+$ to about 60 percent and $C_4H_6^+$ to about 40 percent. Similarly, M42 and M70 are due to

$$\begin{aligned} C_2H_5^+ + C_2H_4 &\rightarrow C_3H_6^+ + CH_3 \qquad (13) \\ &\rightarrow C_4H_8^+ + H \end{aligned}$$

$$C_3H_6^+ + C_2H_4 \rightarrow C_5H_{10}^+ \qquad (14)$$

in analogy to reactions (7) and (8) the branching ratio of reaction (13) cannot be determined, because the $C_4H_8^+$ ion on mass number 56 coincides with

the butene ion formed in reaction (9). It appears, however, from the pressure dependence of the M56 intensity that the contribution of reaction (13) to the mass 56 peak is almost negligible, so that the $C_3H_6^+$ formation in reaction (13) must be the predominant one.

The M29 ion could be conceivably formed from an ethane impurity in ethylene, but since the M30 peak was absent, this possibility is excluded. The nature of the $C_2H_5^+$ ion indicates that it is a product ion, rather than a primary ion. However, the pressure dependence of the sum of the intensities of the M29 sequence is fairly linear as shown in Figure 24, whereas product intensities should show a quadratic pressure dependence around the origin of the plot. On the other hand, it may be recalled that signals due to this ion sequence, albeit small, were also detected in the 1087Å photoionization of ethylene. Hence, it is reasonable to assume that the $C_2H_5^+$ ion and the follow-on ion sequence is due to the process

$$C_2H_4^+ + C_2H_4 \rightarrow C_2H_5^+ + C_2H_3 \qquad (15)$$

The clearer observation of $C_2H_5^+$ and its reaction sequence at a wavelength of 923Å compared with 1087Å, is mainly due to the higher intensity available with the light source combined with a 3 times higher ionization cross section of ethylene at 923Å. An additional factor may be the participation of excited ethylene ions, which according to a mass spectrometric study of Botter, et al (Ref. 24) can be formed at wavelengths below about 1010Å. At 923Å as much as 2/3 of the total ions produced by photoionization may be in an excited state. The quantitative evaluation of the data shows that the ethylene parent ion reactions (7) and (15) have the following probabilities: 83 percent produce $C_2H_5^+$; 11 percent produce $C_4H_7^+$; and 6 percent produce $C_2H_5^+$. The product channel ratio for reaction (7) determined in this case is in reasonable agreement with that found for the same reaction in the 1087Å photoionization of ethylene. Any difference beyond the experimental error must be attributed to the participation of excited ethylene ions.

The formation of butene ions $C_4H_8^+$ via reaction (9) is shown in Figure 22 in comparison to that determined at 1087Å. As in that case, a linear pressure dependence is observed for the intensity ratio at M56 to that of all other $C_2H_6^+$ product ions. However, the rate of M56 formation is only about half that observed at 1087Å. Again, this behavior is indicative of excited ethylene ions. Due to the additional energy content, the $C_4H_8^+$ collision complex would have a shorter lifetime, so that its stabilization by third body collision is less efficient.

The origin of the M27 may now be discussed. This ion is not believed to be formed from $C_2H_6^+$ in a manner similar to M29, because there is no evidence for M27 of the follow-on ions 40 and 54 in the photoionization of ethylene at 1087Å. However, in a mixture of acetylene and ethylene at the

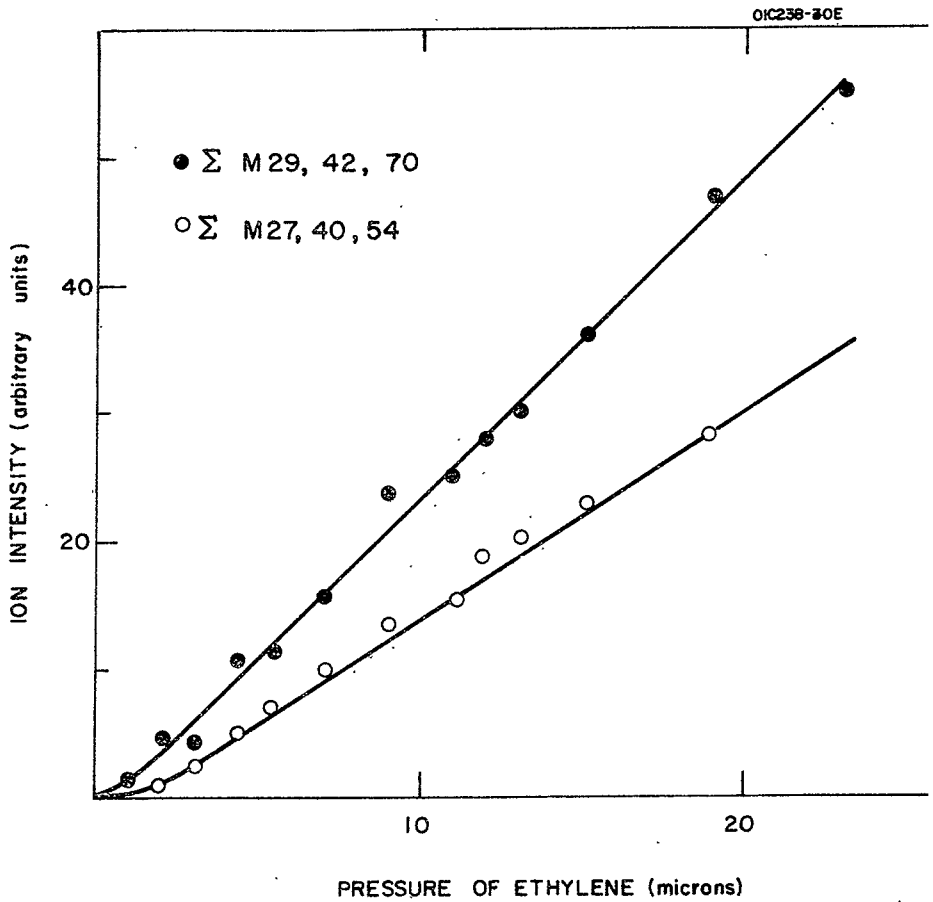

Figure 24 Summed intensities of mass 29 ion sequence (points) and mass 27 ion sequence (open circles) as a function of pressure in the photoionization of ethylene at 923Å.

same wavelength very weak signals were observed at the corresponding mass numbers, indicating the reaction

$$C_2H_2^+ + C_2H_4 \rightarrow C_2H_3^+ + C_2H_3 \qquad (16)$$

Since the ionizing energy at 923Å lies only 0.3 eV above the threshold of $C_2H_2^+$ formation from ethylene, the acetylene ion cannot carry much internal energy and should behave similar to that formed from acetylene at 1087Å. However, at 923Å the formation of $C_2H_3^+$ according to reaction (16) would be more pronounced due to the higher ion intensity, and because of the absence of acetylene which diverts a considerable portion of acetylene ions to the M50 and M51 products due to reaction (4). Figure 24 shows also a plot of the sum of M27 and follow-on ion intensity versus pressure. The behavior is similar to that of the sum of M29 and follow-on ions, i.e. the pressure dependence is more linear, than one would expect for a secondary ion sequence. It should be noted that in the case of the $C_2H_3^+$ ion (but not for the $C_2H_5^+$ ion), there may be a small contribution to its intensity from the dissociative photoionization of ethylene. The threshold for $C_2H_3^+$ formation by that process lies at 898Å, i.e. 25Å toward lower wavelengths. While the applied spectral resolution excludes the direct admission of this radiation to the ion chamber, radiation of shorter wavelengths may nevertheless be present as scattered light.

The $C_2H_3^+$ ion sequence constitutes about 2 percent of the total ion intensity, and about 20 percent of the acetylene ion intensity if it is counted fully as being due to reaction (16). The ratio of acetylene to ethylene ions thus produced by photoionization is $R = (C_2H_2^+)_o/(C_2H_6^+)_o = 0.14$, if the M27 sequence is added to that of M26, and $R = 0.12$ if it is not. These ratios are smaller than those found in other studies of the photoionization of ethylene at 923Å, but they are still within the same order of magnitude. From the data of Botter, et al (Ref. 24) one obtains $R = 0.21$, the data of Brehm (Ref. 25) yield $R = 0.16$ and those of Schoen (Ref. 26) $R = 0.20$. A portion of the discrepancy may be due to the varying efficiencies of the electron multiplier detectors used in these studies. From electron impact ionization studies of ion reactions in ethylene it has been concluded (Ref. 23) that charge transfer of $C_2H_2^+$ to ethylene produces some losses of acetylene ions. Since the data obtained for acetylene-ethylene mixtures at 1087Å gave no evidence for charge transfer, and the probability for this process was shown to be less than 15 percent of the total reaction probability, the effect of charge transfer to the $(C_2H_2^+)_o/(C_2H_6^+)_o$ ratio must be slight.

If the reactions assigned to the acetylene ions are reactions (10) and (16), the branching ratio found for reaction (10) from the photoionization of ethylene at 923Å is $C_3H_3^+/C_4H_5^+ = 2.1$. This agrees within experimental error with the ratio found for the same reaction in a mixture of acetylene and ethylene, $C_3H_3^+/C_4H_3^+ = 2.4$, when the photoionizing wavelength was 1087Å.

Because of the contribution of a dissociative photoionization process to the M27 ion sequence when ethylene is photoionized at 1087Å, the efficiency of reaction (16) can only be estimated. If half of the M27 sequence ion intensity is due to reaction (16), its rate is ten percent of the rate reaction (10), i.e. about 14 percent of $C_2H_2^+$ ions reacting with ethylene yield $C_2H_3^+$.

Having assigned the various products to reactions of either ethylene or acetylene ions reacting with ethylene, the associated reaction rate coefficients can be determined from the decrease of the M28 and M26 ion intensities when compared to the total ion intensities in the corresponding ion sequences. The absolute values of the rate constants thus determined are $k_{4+12} = 0.88 \times 10^{-9}$ cc/molecule sec, and $k_{7+13} = 1.31 \times 10^{-9}$ cc/molecule sec. The former value constitutes only 70 percent of the rate coefficients for ethylene ions formed at 1087Å. This behavior is presumably associated with excited ethylene ions formed at 923Å. The latter rate coefficient is in excellent agreement with the value found for acetylene ions formed at 1087Å, and thus indicates that, in accord with expectation, the $C_2H_2^+$ ion formed from ethylene at 923Å is essentially identical with that formed at 1087Å by the photoionization of acetylene.

Further data have been obtained for reactions of acetylene and ethylene ions with methane, and for some reactions involving methane ions. These results have not been evaluated and will be discussed in future reports.

"Yield of Ions Resulting from Photoionization." A variety of small molecules has been studied with the photoionization mass spectrometer to determine the yield of fragment ions resulting from photoionization. Of particular interest in this work was the investigation of the wavelength dependence of product ions near their thresholds of appearance, because it allows the determination of appearance potentials, which in turn provide information on important thermodynamic properties of the ions and their parent molecules.

The techniques involved have been reported previously (Refs. 27,28) and only a brief summary is required here. The photoionization mass spectrometer employed involves a 1/2 meter Seya grating monochromator with the slits set to provide a spectral resolution of about 3.5Å at half-width. The monochromator exit slit also serves as the entrance slit to the ion source chamber. After passing the ion chamber, the radiation is registered on a sodium-salicylate-coated photomultiplier. From the ion chamber, ions are withdrawn at right angles to the light beam through an aperture of 3 mm diameter. A concave repeller provides a concentric field configuration which enhances the collection of ions. Subsequently, the ions are focused onto the entrance aperture of a 180 degree magnetic analyzer, behind the exit orifice of which the ions are registered by means of an electron multiplier detector. An electrometer readout circuit and recording equipment complete the experimental arrangement.

The experimental procedure entailed taking simultaneous recordings as a function of wavelength of the photomultiplier current and the ion current. For this purpose, the magnet current of the mass spectrometer was adjusted to allow the desired ionic species to pass the mass analyzer, and the wavelength drive of the monochromator was actuated. Two types of light sources were used which gave overlapping spectra in the wavelength region of interest: (a) a dc cold cathode type source operated with hydrogen as the filler gas provided a usefully intense spectrum between 900 and 1300Å; (b) a Weissler type repetitive spark source operated with argon gave a usefully intense spectrum between 450 and 1000Å. Both light sources emit line spectra but the population of emission lines made available is sufficiently dense to provide data points not more than 10Å apart over most of the investigated wavelength range. The ion yield curves thus obtained are sufficiently well defined to allow their extrapolation to threshold. Since, in addition, polyatomic molecules do not usually exhibit narrow structure in absorption and photoionization cross sections, the many line radiation source employed here suffice for this study.

To date, detailed data have been obtained for methane, methanol, formaldehyde and formic acid. These substances were introduced to the ion source chamber via an appropriate leak valve at a pressure of about 10^{-3} Torr. At these high source pressures satellite mass peaks due to secondary ion reactions were observed but their intensity was insignificant. These secondary peaks, for example M33 from methanol, could be identified easily from the fact that their thresholds coincided with that of the parent peaks. Although the effect of the satellite ion peaks could be reduced by working at lower pressures, it was advantageous to make use of the generally good ion intensities provided in the 1×10^{-3} Torr pressure regime and to tolerate the appearance of secondary ions.

Figure 25 shows, as an example, the ion yields for CH_4^+ and CH_3^+ observed in the photoionization of methane in the 800-1000Å wavelength region. From the yield curves the onsets can be determined by extrapolation. We find the thresholds for CH_4^+ at 976Å and for CH_3^+ at 874Å. After correction for the involved spectral resolution, the resulting threshold wavelengths and associated energies are

CH_4^+	973 ± 3Å	12.74 ± 0.04 eV
CH_3^+	871 ± 3Å	14.23 ± 0.06 eV

These values are in good agreement with those determined by Dibeler, et al. (Ref. 29) and by Chupka (Ref. 30).

In a similar manner, thresholds for various ions have been determined for methanol and formaldehyde. These are given in Table 1. The relative

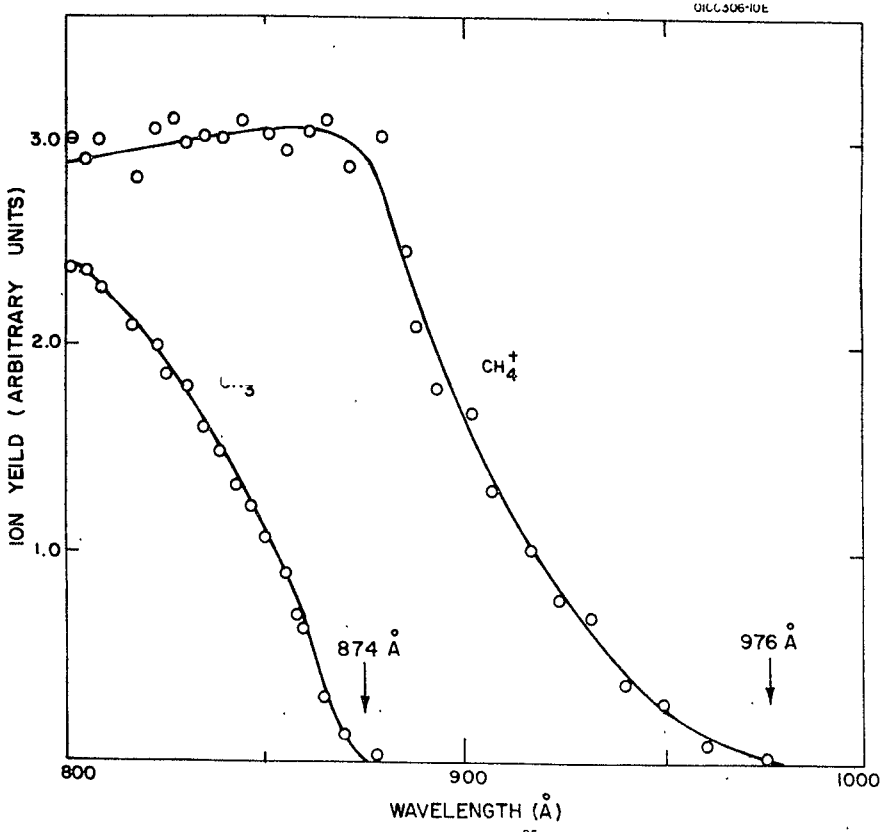
ION YEILD (ARBITRARY UNITS)
3.0
2.0
1.0
800
900
1000
WAVELENGTH (Å)
874 Å
976 Å
CH_4^+

Figure 25

TABLE 1

Photoionization Thresholds for the Appearance of Ions in Methanol and in Formaldehyde

Compound	Ion	Threshold Wavelength (Å) Observed	Corrected	Energy (eV)
CH_3OH	M32	1145 ± 3	1142 ± 3	10.85 ± 0.03
	M31	1077 ± 3	1074 ± 3	11.54 ± 0.03
	M30	1033 ± 10	1030 ± 10	12.04 ± 0.12
	M29	952 ± 7	949 ± 7	13.06 ± 0.10
	M15	900 ± 3	897 ± 3	13.82 ± 0.04
	M14	883 ± 5	880 ± 5	14.09 ± 0.08
CH_2O	M30	1142 ± 2	1139 ± 2	10.89 ± 0.02
	M29	1046 ± 3	1043 ± 3	11.89 ± 0.03
	M 2	807 ± 3	804 ± 3	15.42 ± 0.06
	M 1	715 ± 3	712 ± 3	17.41 ± 0.07

ion yields as a function of wavelength for these compounds and for formic acid have not yet been evaluated in detail, but as supplementary information we give in Table 2 the ion distribution for all the compounds investigated at the photoionizing wavelength of 801Å.

The threshold energies assembled in Table 1 will now be used to derive some important selected thermodynamic properties. From the appearance potentials of the parent ions of methanol and formaldehyde one obtains the ionization energies 10.85 eV from CH_3OH and 10.89 eV for CH_2O. These values are in excellent agreement with those determined by Watanabe (Ref. 31) and collaborators using a different photoionization method. Next consider the appearance potentials for CH_3^+ and CH_2^+ from methanol. After subtraction of the spectroscopic ionization potentials (Ref. 32) for CH_3 and CH_2 (CH_3) = 9.843 eV and I (CH_2) = 10.396 eV, respectively, one obtains the dissociation energies for the processes

$$CH_3OH \rightarrow CH_3 + OH \qquad D_1$$

$$\rightarrow CH_2 + H_2O \qquad D_2$$

The values thus derived: $D_1 = 3.98 \pm 0.04$ and $D_2 = 3.69 \pm 0.08$ can be utilized to derive the heats of formation of the CH_3 and CH_2 radicals by virtue of the relations:

$$D_1 = \Delta H_f\ (CH_3) + \Delta H_f\ (OH) - \Delta H_f\ (CH_3OH)$$

$$D_2 = \Delta H_f\ (CH_2) + \Delta H_f\ (H_2O) - \Delta H_f\ (CH_3OH)$$

The resulting heats of formation are $\Delta H_f\ (CH_3) = 1.49 \pm 0.04$ eV = 34.3 ± 1 kcal/mole, and $\Delta H_f\ (CH_2) = 4.07 \pm 0.08 = 93.6 \pm 2$ kcal/mole. These values are in good agreement with those derived by Chupka (Ref. 30) and by Dibeler, et al. (Ref. 29) from the photoionization of methane and CH_3 radicals, although Chupka's values are more precise. From the threshold of CHO^+ appearance from CH_3OH, the heat of formation of CHO^+ can be derived via the relation

$$A\ (CHO^+) = \Delta H_f\ (H) + \Delta H_f\ (CHO^+) - \Delta H_f\ (CH_3OH)$$

which assumes the the process responsible for the formation of CHO^+ is

$$CH_3OH + h\nu \rightarrow CHO^+ + H_2 + H$$

TABLE 2

ION YIELDS FOR METHANE, METHANOL, FORMALDEHYDE & FORMIC ACID AT 801Å

Substance	m/e	Relative Ion Yield
Methane	16	0.585
	15	0.414
Methanol	32	0.443
	31	0.492
	30	0.009
	29	0.028
	15	0.031
Formaldehy	30	0.433
	29	0.550
	28	0.016
Formic Aci	46	0.462
	45	0.286
	41	0.003
	32	0.028
	31	0.055
	30	0.003
	29	0.100
	18	0.064

Since the threshold of CHO^+ occurs at a higher energy than that of CH_2O^+ of CH_3O^+ it is reasonable to assume that the above reaction requires two steps, with one of these ions as an intermediate. For example,

$$CH_3OH + h\nu \rightarrow (CH_3O^+)^* + H$$

$$(CH_3O^+)^* \rightarrow CHO^+ + H_2$$

Here, the asterisk indicates that the intermediate ion must be internally excited to dissociate further in the process of CHO^+ formation. Since the dissociation process may require an activation energy, the threshold of CHO^+ formation can provide only an upper limit to the heat of formation of CHO^+. The present data yield ΔH_f $(CHO^+) \leq 8.62 \pm 0.10$ eV = 198 $\pm$ 2 kcal. This value is in excellent agreement with the heat of CHO^+ formation previously derived by us from the photoionization of formaldehyde (see below), formic acid, and acetaldehyde (Ref. 33). It thus appears that the activation energy involved in the dissociation of the intermediate is negligible. From the threshold of CH_2O^+ formation we find that the energy involved is by 0.19 eV of 4.4 kcal higher than predicted on account of the process

$$CH_3OH + h\nu \rightarrow CH_2O^+ + H_2$$

for which all the required thermodynamic values are known. Thus it appears that the intermediate for CHO^+ formation is CH_3O^+ rather than CH_2O^+. On the other hand, the heat of formation for CH_3O^+ derived from the threshold of its observation is ΔH_f $(CH_3O^+) = 7.20 \pm 0.03$ eV = 166 $\pm$ 1 kcal, in good agreement with a value recently derived by Haney and Franklin (Ref. 34) from electron impact mass spectrometry with consideration of the excess kinetic energy of the fragments.

Similar considerations apply to the data for formaldehyde. From the threshold of CHO^+ formation one obtains ΔH_f $(CHO^+) = 8.51 \pm 0.03$ eV = 196 $\pm$ 1 kcal. This result has been reported previously (Ref. 33). The formation of H_2^+ is due to the process

$$CH_2O + h\nu \rightarrow CO + H_2^+$$

The threshold of 15.42 eV is in good agreement with that calculated for this process from known available thermochemical values A (H_2^+) = 15.40 eV. The formation of H^+ is associated with

$$CH_2O + h\nu \rightarrow HCO + H^+$$

This process allows the derivation of the heat of formation of CHO. Subtracting from the threshold energy for H^+ formation the ionization potential of the hydrogen atom, I (H) = 13.595 eV, gives the bond dissociation

energy for formaldehyde D (CHO - H) = 3.82 eV = 88 $\pm$ 2 kcal/mole. The corresponding value for the heat of formation of CHO is ΔH_f (HCO) = 0.43 $\pm$ 0.07 eV $\approx$ 10 kcal/mole. From this value, the dissociation energy of the HCO radical can be calculated as D (H - CO) = 15.7 kcal. In deriving these values the new heat of formation of formaldehyde (Ref. 35), ΔH_f (CH_2O) = -25.9 kcal/mole, has been used. The value for D (CHO - H) derived here is the high value of the two possibilities discussed in the literature. Similarly, the value for D (H - CO) derived here is the low value for the discussed two possibilities. Independent evidence for D (CHO - H) = 88 kcal/mole has been derived previously by Haney and Franklin (Ref. 34). From a detailed discussion of previous data, Kerr (Ref. 36) has also favored this value.

Although an analysis of the formic acid data is even less complete than the ones discussed above, a check has been made on the heat of formation of the CHO radical by the observation of the threshold for the process

$$HCOOH + h\nu \rightarrow HCO + OH^+$$

which was observed to occur at 690Å, corresponding to 17.97 eV. The value for the heat of formation of HCO derived from this process is ΔH_f (CHO) = 0.45 eV = 10.5 kcal. This is in good agreement with the value found above from formladehyde, supporting the high value for ΔH_f (CHO) and for D (CHO-H).

"Measurement of Ionic Mobilities" The effort under this heading represents a continuation of previous work concerning the title subject. It has been demonstrated previously (Ref. 37) that the photoionization mass spectrometer technique can be employed to obtain reliable drift velocity data for mass analyzed ions produced by photoionization. In this manner it is possible, in principle, to preselect the energy state of the ion by an appropriate choice of varying wavelengths, and to identify the ion subjected to measurement by the employed mass spectrometer.

The experimental set up and the applied experimental procedures have been described in detail previously (Refs. 37,38) and will be summarized only briefly here. The cylindrical ion chamber configuration employed for this application of the instrument is conventional in that ions formed along the axis of this light beam are driven to the ion exit aperture by an electric field established perpendicular to the direction of the light beam. The plane repeller is supported by a hollow stem so that the gas pressure in the source can be measured directly with an attached McLeod manometer. As a consequence of the ion source geometry the electric field is inhomogeneous everywhere except in the vicinity of the axis of ion removal. The field in this region was calculated from the applied voltage and from the distance between the repeller and the ion exit aperture, the positions of which were adjusted to a spacing of 0.70 cm. A small correction was required to take into account the slight field inhomogeneity near the repeller. This was shown by a field plotting method previously (Ref. 37).

The light source is a Weissler type repetitive spark source, providing 120 pulses per minute of about one microsecond duration each. This time is sufficiently short to provide an essentially instantaneous ion deposition, unless the residence time of the ions in the ion chamber becomes comparable. Under the applied conditions of pressure and electric field, ion residence times are usually longer than 10 microseconds. A further necessary experimental condition for mobility studies is that the mean free path of the ions is short compared with the drift distance. This condition is met at pressures above about 80 microns.

Due to diffusion, the ion transient broadens while drifting from the plane of origin toward the ion exit plane. Thus, the initially rectangular ion transient profile is changed to a Gaussian profile. The average ion residence time, τ_o is defined as the time span required for the center of the profile to reach the exit aperture after deposition of the ions by the light pulse. Accordingly, the ion drift velocity is $v = d/\tau_o$, with d being the drift distance (0.3 cm in the present arrangement). Due to the process of diffusion broadening, some ions arrive at the exit at an earlier time $\tau < \tau_o$. It has been shown previously that τ and τ_o are related by the equation

$$\tau/\tau_o = 1 - (f/d)\ (2\ D\tau)^{1/2}$$

where D is the ionic diffusion coefficient and f is a factor depending upon the threshold sensitivity for the detection of the onset of the ion pulse. If the detection limit is 10 percent of the total integrated ion pulse, f = 1.28, if it is five percent of the integrated ion pulse, f = 1.65. The former factor has been used previously (Ref. 38), but due to the increased sensitivity, the latter value will be used here. Then, the measurement of both τ and τ_o will provide the ionic diffusion coefficient

$$D = \frac{1}{2}\ \frac{d^2}{f^2}\ \frac{(1 - \tau/\tau_o)^2}{\tau} = 1.65 \times 10^{-2}\ \frac{(1 - \tau/\tau_o)^2}{\tau}$$

Knowledge of the diffusion coefficient and the ionic mobility $\mu = v/E$ provides the average energy content of the drifting ions. To derive the random energy of the ions, expressed as the ionic temperature, T_i, we make use of a relation due to Einstein (see for example Huxley and Crompton, Ref. 39).

$$T = F\ \frac{e}{k}\ \frac{D}{\mu}$$

where e is the ionic charge, k is the Boltzmann constant, and F is a factor depending on the velocity distribution function of the ions. For a Maxwellian

distribution F = 1, for other distributions F is usually somewhat smaller than unity. Here it will be assumed that F = 1. Then the ion temperature is defined as

$$T_i = \frac{e}{k} \frac{1}{2} \frac{d}{f^2} \frac{(1 - \tau/\tau_o)^2}{\tau/\tau_o} E$$

$$= 6.38 \times 10^2 \frac{(1 - \tau/\tau_o)^2}{\tau/\tau_o} E$$

The formula then reduces the ion drift velocity, the ionic diffusion coefficient, and the ion temperature to the residence times τ and τ_o in the ion chamber. These quantities are determined experimentally from the time delay of the ion pulse arriving at the mass spectrometer detector, after a group of ions is formed by the light pulse. Delay times are measured as a function of the repeller potential and a graphical extrapolation toward infinite repeller potential is applied to enable a separation of the ion source residence times from the mass spectrometer flight time of the ions. The details of this procedure have been published (Ref. 38).

Below we report data on the parent ions in three gases: argon, nitrogen, and oxygen.

Argon: The drift velocities observed for A^+ in argon are plotted in Figure 26 as a function of the reduced field strength E/P_o, for three values of the electric field and various settings of pressure in the range 70-210 microns. The lower group of data points represents measurements with the monochromator set to transmit a wavelength of 786Å (with 3.5Å halfwidth), so that only argon ions in the $^2P_{3/2}$ ground state are formed. The upper group of data points was obtained at 767Å. In this case excited $^2P_{1/2}$ argon ions are formed in addition to those in the ground state. At 786Å, the ion transient observed with the oscilloscope was fairly symmetric and the center of the pulse was used to derive the drift velocities. At 767Å an additional component was present, the ion transient had an asymmetric appearance, and the peak of the pulse (which was used to derive the drift velocity) shifted forward. The two types of oscilloscope traces are shown in Figure 27 for comparison. Clearly, the excited argon ion moves faster than the ground state ion. Since the mobility of an ion, like its diffusion coefficient, is inversely proportional to its cross section for momentum transfer to the neutral gas, suitably averaged over the range of velocities, the data indicate that the momentum transfer cross section for the excited argon ion is smaller than that for the ground state argon ion. For both types of argon ions moving in the parent gas, the momentum transfer cross section is governed mainly by charge transfer. Theoretically one would predict, on the assumption that the reduced matrix elements governing the two charge transfer cross sections are nearly equivalent, that the difference in cross sections is due to the differences in the degeneracy of the

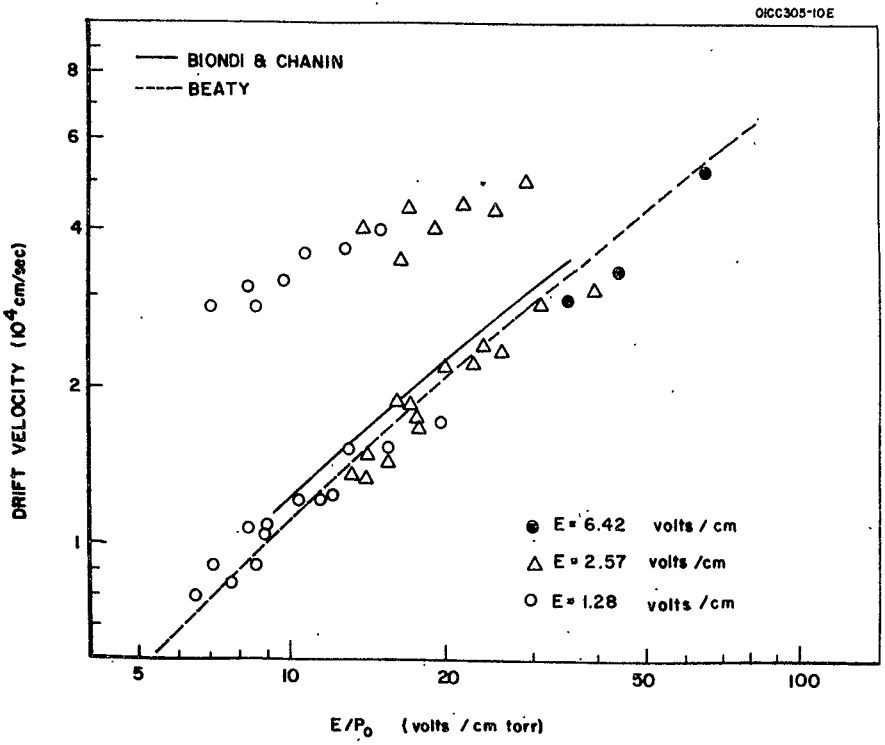

Figure 26: Drift velocities of argon ions in their parent gas. Ionizing wavelength: Lower group of points 786Å; Upper group 767Å.

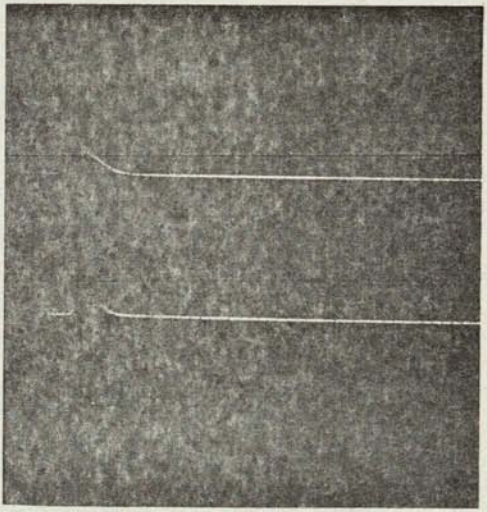

Figure 27. Argon ion transients. Lower trace: 786Å; upper trace: 767Å.

two processes. Thus, the summation over all possible magnetic quantum number combinations indicates $Q_{ground}/Q_{excited} = 2$, because the resonant process $A^+ (^2P_{1/2}) + A (^1S_o)$ is 2 fold degenerate. The observed increase in mobility when going from the ground state to the excited state is about three at the lower end of the reduced field strengths. Towards higher fields, the ratio becomes smaller due to the fact that the drift velocity for the excited argon ions increases with E/P approximately with 1/2 power, whereas the drift velocity of ground state argon ions increases essentially linearly with E/P.

The data obtained for ground state argon ions are found to be in excellent agreement with previous measurement. Two sets of previous data are shown in Figure 26, those by Biondi and Chanin (Ref. 40) are represented by the solid line and those by Beaty, et al. (Ref. 41) are indicated by the dashed line. Two more recent measurements, like the present one with mass identification, were made by McAfee, et al. (Ref. 42) and by Madson and Oskam (Ref. 43). They are in good agreement with the former and the present measurements. An extrapolation of the present data to zero electric field leads to a reduced zero field mobility of A^+ of $\mu = 1.5$ cm^2/sec volt. It must be realized that the drift velocities of the excited argon ions cannot be measured with the same reliance as that of the ground state ions, because the two ion transients cannot be sufficiently separated so that the arrival time of the center of the excited ion transient is falsified by the contribution due to the normal argon ions. Accordingly, the data presented here for that ion species must be considered tentative. Qualitatively, however, there can be no doubt about the increased drift velocity of the excited ion compared with the ground state ion. The importance of this finding should not be underrated. It has been made possible solely by the energy differentiation provided by the method of photoionization.

The good results obtained for ground state ions in argon have encouraged measurement of diffusion coefficients and ion temperatures according to the methods outlined above. These are shown in Figures 28 and 29. The straight line in Figure 10 is calculated from the thermal, zero field mobility of the argon ions. The data points agree with the calculated diffusion coefficients, indicating that the energy that the argon ions acquire from the field is quickly passed on to the neutral argon matrix. This behavior is reflected also in the derived ion temperature, which lies only little above that corresponding to thermal ions. A considerable scatter of the data points in Figure 29 makes apparent that an accurate determination of ion temperatures is not possible by this method. However, the good agreement of ion temperature and diffusion coefficients with the expected ion behavior indicates the validity of the concepts underlying their derivation.

Nitrogen: Drift velocities observed for nitrogen ions formed from molecular nitrogen at an ionizing wavelength of 790Å were reported previously by us and are shown in Figure 30. There is good agreement with the results

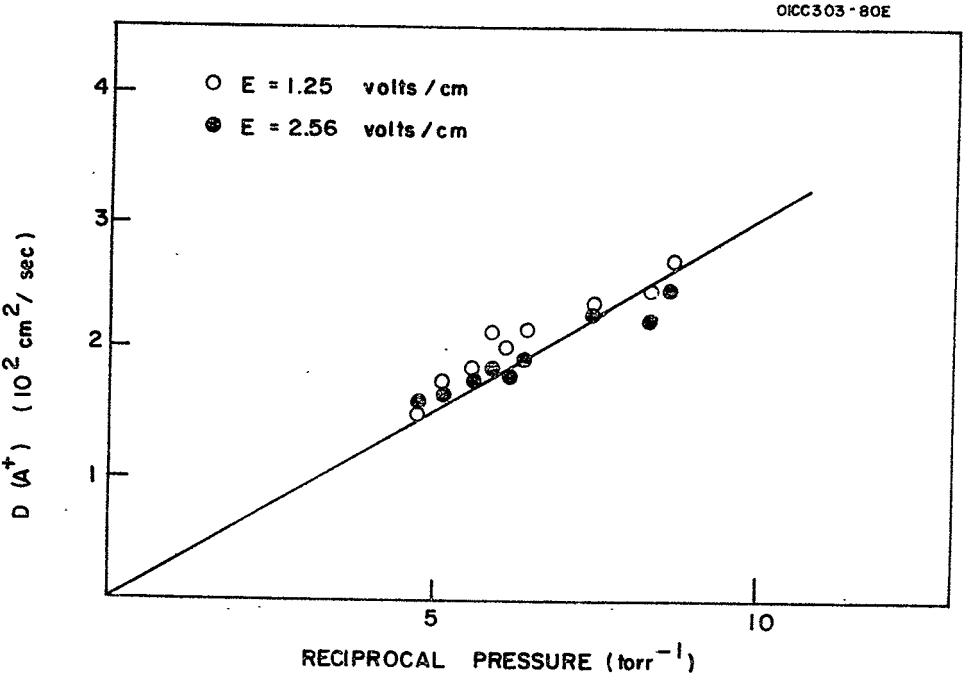

Figure 28: Diffusion coefficients for $A^+(^2P_{3/2})$ ions in argon. Solid line calculated for thermal ions.

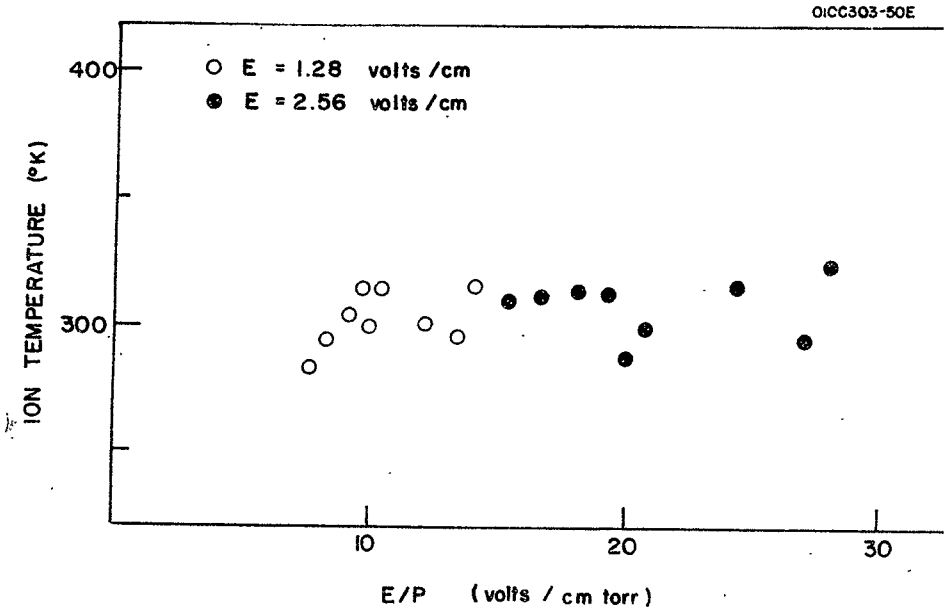

Figure 29: Temperature of $A^+(^2P_{3/2})$ ions as a function of E/P.

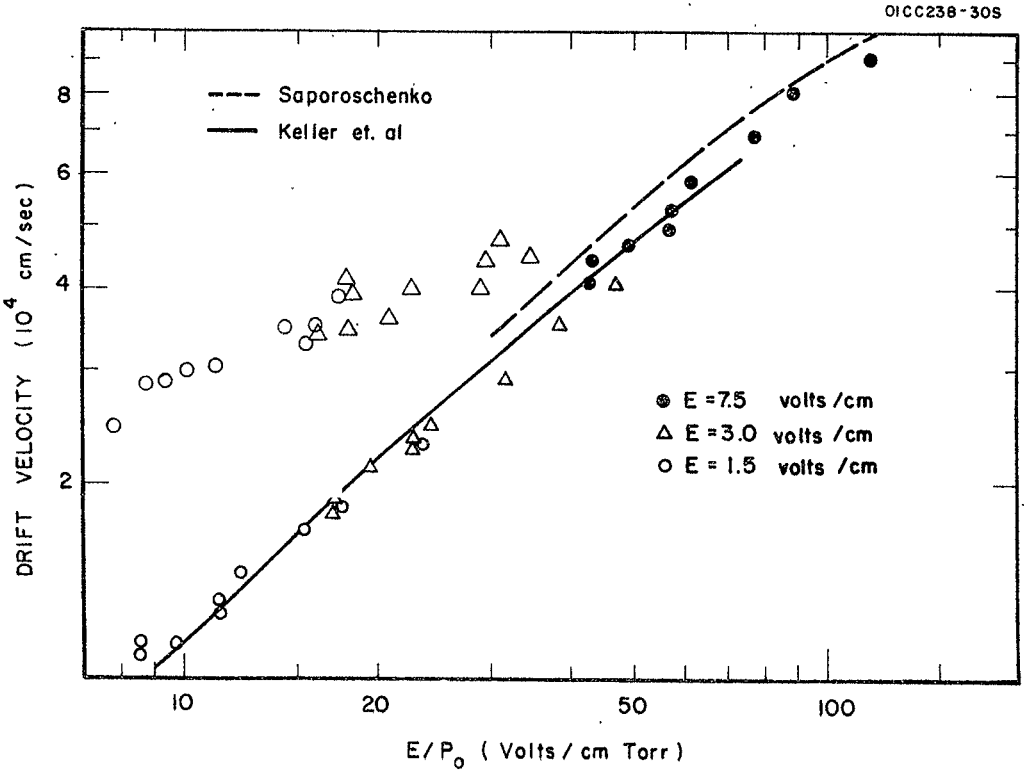

Figure 30: Drift velocities of N_2^+ in nitrogen versus relative field strength. Ionizing wavelength: lower group of points 790Å; upper group of points 764Å.

of Saparoschenko (Ref. 44) and Keller, et al. (Ref. 45) who also used mass identification of the ions. Similar to the behavior of argon ions, an increase of drift velocities was observed for N_2^+ as the ionizing wavelength was lowered. However, the mobility increase occurred at isolated wavelengths, and was then clearly recognizable as an asymmetry of the ion transient. A very strong asymmetry occurred at 764Å, and drift velocities corresponding to the peak of the ion pulse at this wavelength are shown in Figure 30 as the upper group of data points. The increase in ion mobility appears to occur at wavelengths where the emission lines available from the light soure coincide with autoionization features in the N_2 absorption spectrum. At 764Å, the wavelength investigated here, the line group emitted from the source overlaps the v (1-0) transition at 764.35Å of the Ogawa and Tanaka (Ref. 46) progression (1) series which, having a high ionization efficiency produces a considerable population of vibrationally exicted N_2^+ (v = 1) ions. Accordingly, the increased mobility, v, at 764Å is due to vibrationally exicted N_2^+ ions, whereas at 790Å only ground state nitrogen ions are formed. Similar to the results discussed above for argon ions, the N_2^+ ion mobility increases by a factor of about 3 for vibrationally excited ions. A similar behavior with E/P is observed as for ions in argon.

Figures 31 and 32 show the diffusion coefficients and the ion temperatures determined for N_2^+ (v = 0), respectively. Unlike the behavior of argon ions, the diffusion coefficients are much higher than that for thermal ions (indicated by the solid line), and the ion temperatures derived lie also considerably above thermal values. Both factors indicate an appreciable energy content of N_2^+ ions in the presence of electric fields. Note also that both diffusion coefficients and ion temperatures increase as the field strength is increased.

Oxygen: The drift velocities determined for O_2^+ ions as a function of E/P are shown in Figure 33. These data were obtained with an ionizing wavelength of 1007Å, and good agreement is observed with the results of previous investigations (Refs. 47,48) in which the identity of the ion was inferred rather than determined. At 1007Å, photoionization of O_2 may lead to O_2^+ in the first vibrationally excited state, but from the results it appears that the direct photoionization probability for the formation of O_2^+ (v = 1) is only a very small fraction of that leading to ground state O_2^+ ions. Unfortunately, a sufficiently strong emission line was not available in the region 1007-1027Å (where O_2 ionization initiates), so that the O_2^+ (v = 1) formation could not be positively excluded. However, similar to the previous case (N_2^+), an increase in mobility was observed at autoionization features of oxygen. Figure 34 shows that wavelength at which the O_2^+ residence time in the ion source chamber decreased when the other experimental conditions are kept constant. Each such decrease of residence

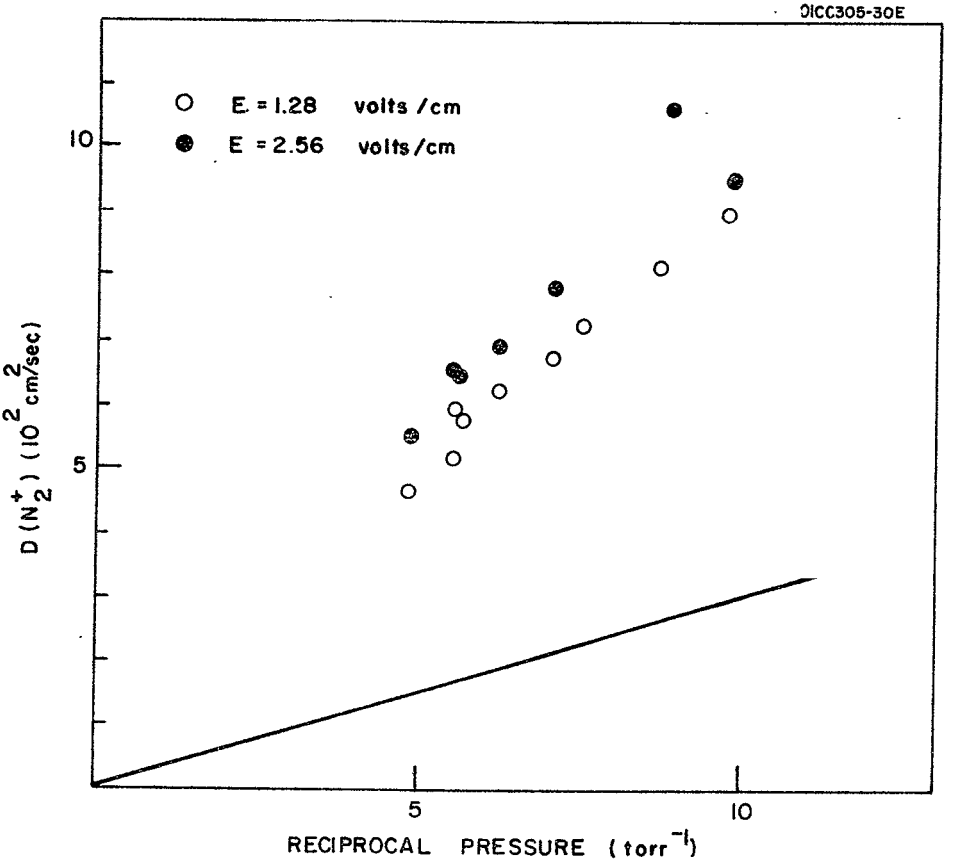

Figure 31: Diffusion coefficients for N_2^+ (v = 0) ions in nitrogen. Solid line calculated for thermal ions.

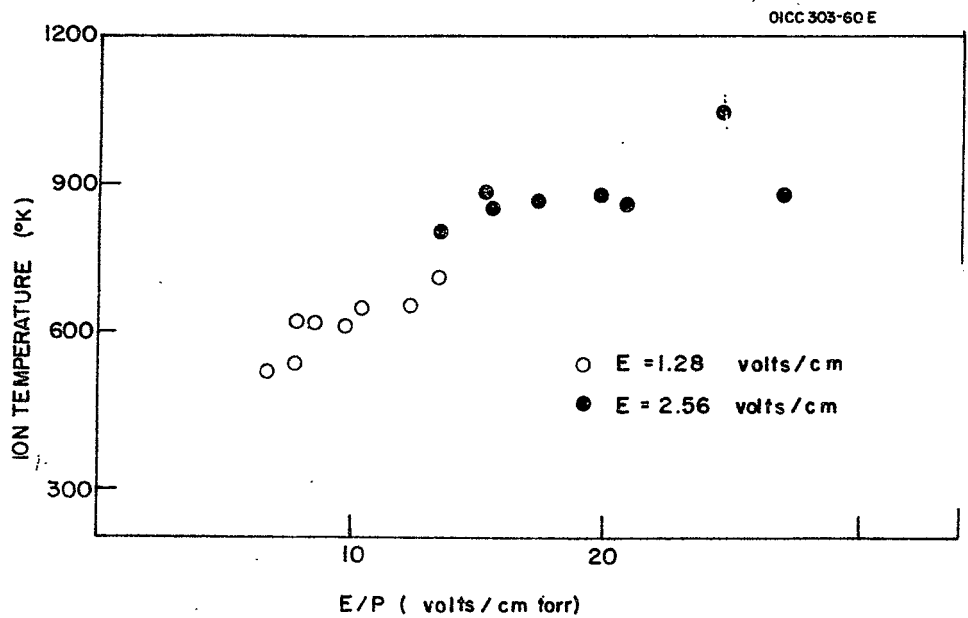

Figure 32 Ion temperature for N_2^+ (v = 0) in nitrogen as a function of E/P.

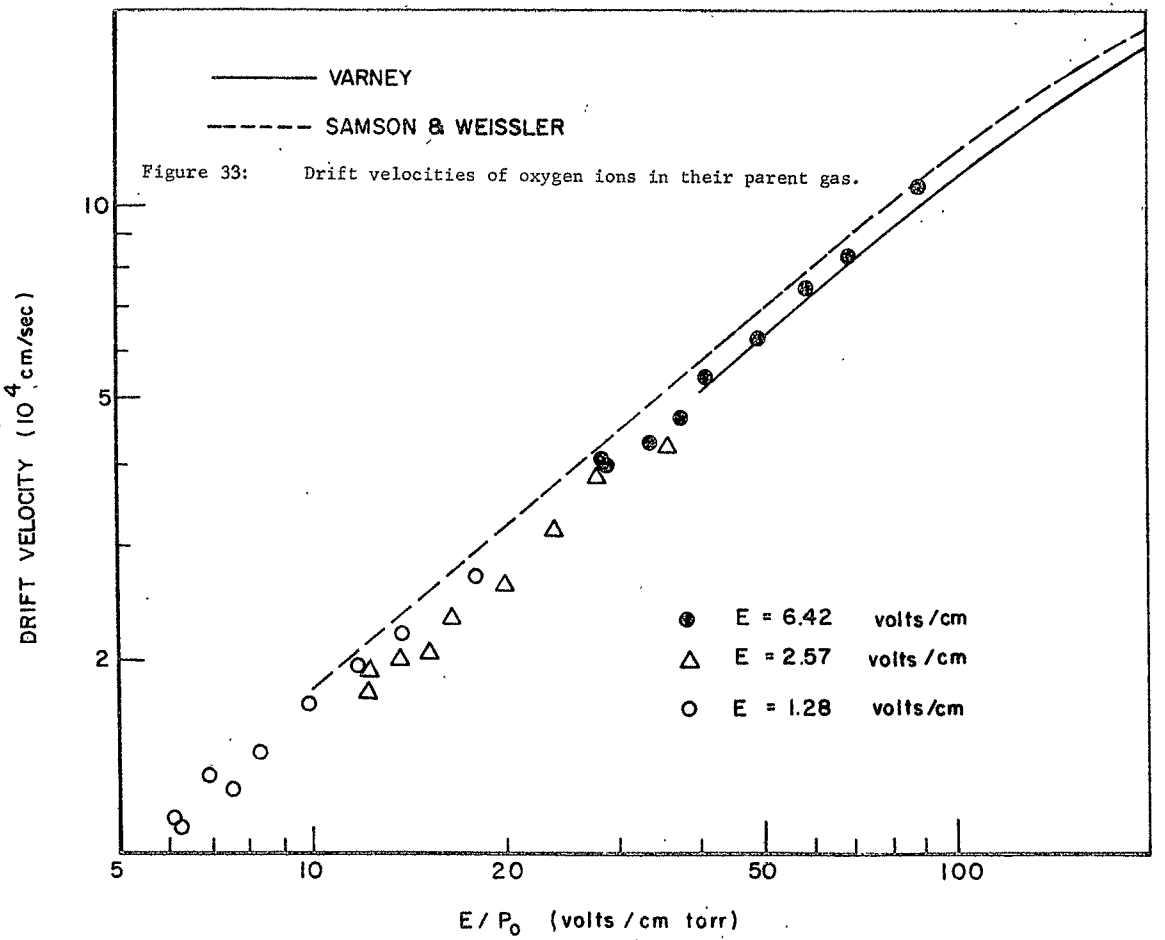

Figure 33: Drift velocities of oxygen ions in their parent gas.

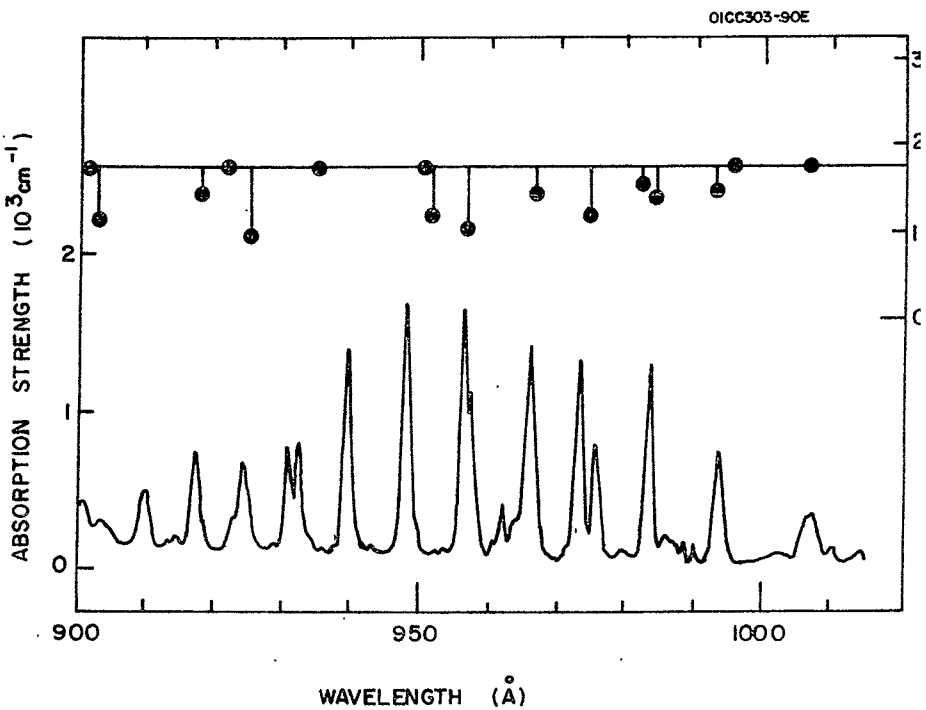

Figure 34: Correlation of oxygen on residence time with autoionization features in the absorption spectrum of oxygen.

time (or increase of ion mobility) correlates with an autoionization feature in the absorption spectrum of oxygen in the 900-1000Å wavelength region here investigated. The limited number of strong emission lines available from the light source prevents the demonstration that an increase of mobility is associated with every sufficiently energetic autoionizing feature, but the number of available lines appears to be sufficient to prove the point. The variation in residence times observed is due to the degree of overlap of emission and absorption intensities and the varying ionization efficiencies.

Figures 35 and 36 show the diffusion coefficients and ion temperatures derived for O_2^+ formed at 1007Å. Again it is evident from both groups of data that the ions drifting in the electric field are non-thermal, although the increases in the diffusion coefficient and the ion temperature above thermal values are not as drastic as was found for nitrogen ions.

B. Theoretical Studies

Published Data.-

"Mariner 6: Origin of Mars Ionized Carbon Dioxide Ultraviolet Spectrum"

A. Dalgarno, T. Degges and A. Stewart

Science 167, #3924, 1490 (1970)

Predicted intensities of the ionized carbon dioxide (CO_2^+) emission feature at 2890Å and the Fox-Duffendack-Barker bands are 5.2 and 19.9 kilorayleighs, respectively, for a vertical column. Direct photoionization of carbon dioxide by solar radiation contributes 3.5 and 4.1 kilorayleighs, respectively, and fluorescent scattering by CO_2^+, 1.6 and 15.3 kilorayleighs, respectively. Photoelectron impacts are less important.

"Dipole Properties of Molecular Hydrogen"

G. Victor & A. Dalgarno

Journal of Chemical Physics 50, #6, 2535 (1969)

Experimental data on electron scattering, optical refractivity, and molecular anisotropy are used to construct a model dipole spectrum for molecular hydrogen which is consistent with oscillator strength sum rules. The model spectrum is used to calculate the parallel and perpendicular dynamic dipole polarizibilities, the refractive index, the Verdet constant, the Rayleigh scattering cross section, the Rayleigh depolarization factor, and the molecular anisotropy as a function of frequency of the incident radiation. The tensor components of the van der Waals coefficient for a pair of interacting hydrogen molecules are also calculated.

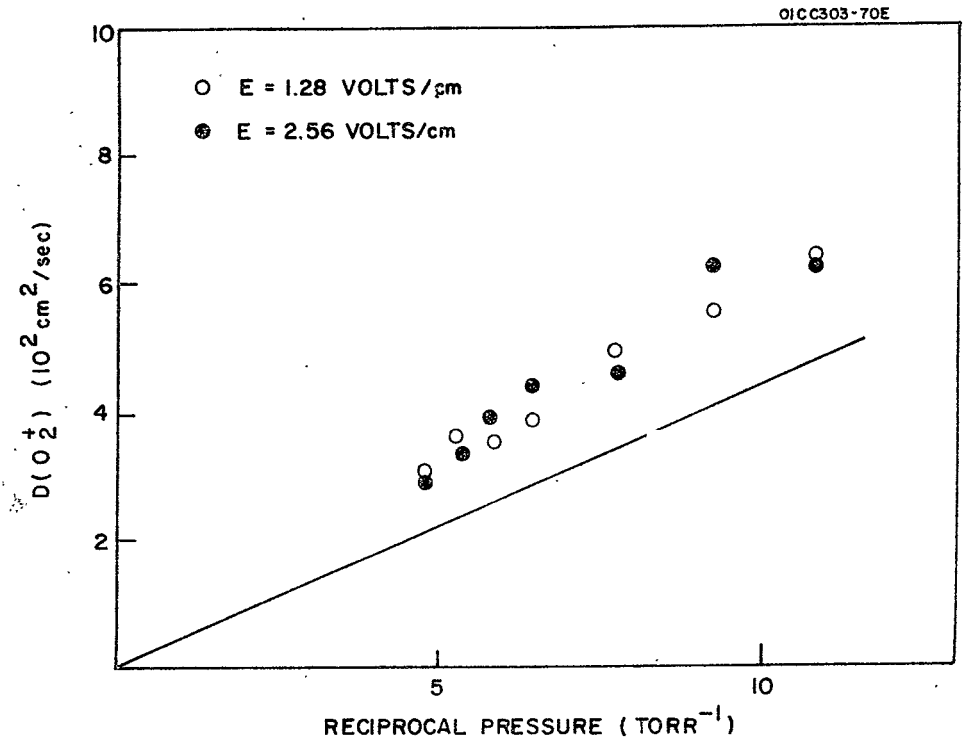

Figure 35: Diffusion coefficients for O_2^+ ions in oxygen. Solid line calculated for thermal ions.

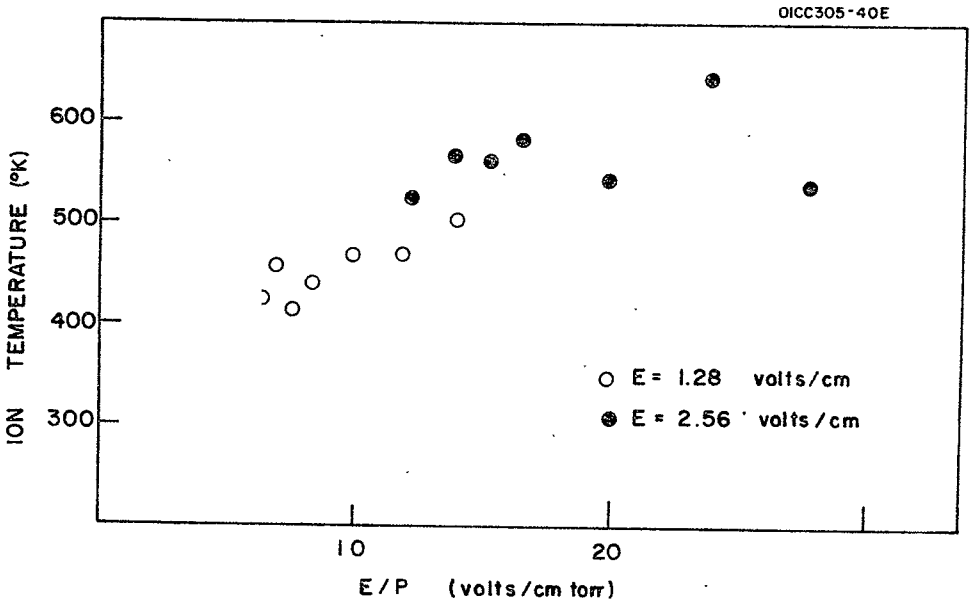

Figure 36: Ion temperature for oxygen ions in oxygen as a function of E/P.

"The Effect of Oxygen Cooling in Ionospheric Electron Temperatures"

A. Dalgarno, M. McElroy, M. Rees, & J. C. G. Walker

There are discrepancies between ionospheric electron temperatures derived from Thomson scatter data and electron temperatures predicted from the solar ultra-violet heat source. The inclusion of electron cooling by excitation of the fine structure levels of atomic oxygen removes the discrepancy throughout the day at all altitudes above 320 km. Below this altitude a discrepancy persists, but it probably lies within the uncertainties arising from the basic atomic and molecular data employed in the theoretical analysis and from the solar flux data.

"CO_2^+ Dayglow on Mars and Venus"

A. Dalgarno and T. Degges

Quantitative calculations are presented of the intensities of the CO_2^+ bands present in the dayglows of Mars and Venus and it is argued that fluorescent scattering by CO_2^+ ions and photoionization of CO_2 are the main sources of excitation. An estimate is made of the intensity of 3914Å emission that would arise if the atmosphere contained N_2.

"Electron Impact Excitation of the Dayglow"

A. Dalgarno, M. McElroy and A. Stewart

Journal of Atmospheric Sciences 26, #4, 753(1969)

Calculations are described of the equilibrium velocity distributions of the photoelectrons produced in the F-region by solar ionizing radiation. Detailed estimates are presented of the intensities and altitude profiles of emission features of atomic oxygen, molecular nitrogen, and molecular oxygen, appearing in the dayglow as a result of photoelectron impacts.

"Carbon Atoms in the Upper Atmosphere of Venus"

F. F. Marmo and A. Engelman

ICARUS

The detection of carbon atoms in the upper atmosphere of Venus is reported on the basis of an extension of a previously reported analysis of low resolution spectra of the solar illuminated atmosphere of Venus. It is demonstrated that the previously reported anomalously high albedo for $\lambda\lambda >$ 1500Å can be explained by invoking the presence of a 14 kR CI signal at 1657Å. It is possible to check the validity of this conclusion on a future Venus fly-by mission which employs a scanning spectrometer operating in this spectral region. Furthermore, if it is valid to extrapolate these results to the case of Mars the vacuum ultraviolet spectra acquired by the Mariner 6 and 7 missions should include this spectral feature as well as some of the more intense bands of the CO 4th positive system.

Unpublished Data.- "Mars Lander Experiment -- Spectral Photometric Observations of the Martian Atmospheric Dayglow." The identification of the atomic and molecular constituents in a planetary atmosphere is a fundamental branch of planetary aeronomy. For the earth atmosphere, one of the most prolific sources for these type of data have been obtained through the performance of airglow observations employing ground based spectrophotometric techniques. However, the performance of such experiments are severely constrained owing to two important limitations: (a) the spectral region of investigation is limited to wavelengths greater than 3000Å owing to atmospheric attenuation, and (b) throughout the visible regions intense background radiations (on the order of megarayleighs) can be encountered owing to Rayleigh and Mie scattering of the solar illuminated atmosphere. The identification of organic and/or inorganic constituents in the Martian atmosphere is fundamental to the associated aeronomic and exobiological studies. For this purpose the established techniques utilized from the surface of the earth can be translated, extended and modified into an appropriate configuration so that airglow Martian surface observations may be performed taking full advantage of the reduced background scattering as well as the relative absence of atmospheric absorption down to 2000Å. Owing to the great potential involved a number of relevant initial tasks have been performed in order to evaluate the feasibility of performing such a program as well as to identify the type and variety of optical data that can be acquired from a surface based Martian airglow station. In order to operate under realistic constraints it is proposed to employ a rugged, double pass, scanning spectrophotometer probing the spectral region λλ 2000-8000Å. The configuration represents a simplified version of a fully developed instrumentation currently used in earth satellite studies. The proposed spectrometer involves no moving optical components so that it can be packaged for extreme ruggedness in order to survive the relatively high g-loading in the landing environment.

The specific experiments suggested in the following sections involve a host of complex theoretical and practical problems which are considered to lie outside the scope of the present survey and feasibility study. In fact, in some cases, it is difficult to assess the value of performing a specific experiment as compared to other techniques which may be available or have been suggested for the same purpose. Alternatively, it is felt that enough scope and data have been incorporated into the present discussions to amply illustrate the potential involved in a number of applications of airglow observation technology for the identification of specific atomic and molecular constituents in the atmosphere of Mars.

The remaining discussion is presented in the following four sections. The pertinent geometric and solar illumination factors involved in the performance of the proposed Martian twilight, day and night airglow experiments are discussed in addition to a number of possible signal generation sources within the spectral region λλ 2000-8000Å involving some of the more possible constituents in the Martian atmosphere, consideration of the roles of resonance scattering, fluorescence scattering, atmospheric absorption,

nightglow, and Martian dust, and the experimental configuration of the suggested scanning spectrophotometer is discussed.

Most of the pertinent geometric parameters involved in this study are illustrated in Figure 37. In this section, a number of relationships will be deduced between these several parameters which are employed subsequently in the development and discussions of the suggested experimental configurations.

Zenith (β=0) sky radiances have been calculated for both earth and Mars for the case of solar zenith angle of zero degrees (i.e., overhead sun) employing available model atmosphers for earth and Mars, (Refs. 49,50) the appropriate incident solar fluxes (Ref. 51) and the absorption (Ref. 52) and Rayleigh scattering (Ref. 53) characteristics of the several pertinent planetary atmospheric constituents. The results are shown in Figure 38 wherein the heavy dashed and solid curves obtain for the earth and Mars zenith radiances respectively. It should be noted that two separate radiance scales are employed in this figure which illustrates two important factors. First, over the spectral range $\lambda\lambda$ 3000-8000Å, Martian atmospheric background intensities are about two orders of magnitude less than those on earth (which is roughly equivalent to a platform located at about 30 km above the surface of the earth) and second, the fact that the observational spectral range is extended down to 2000Å for the case of Mars. However, a portion of the apparent improvement in background radiation is due to the scaling factor applied to the lower incident Martian solar flux. Thus, solar flux dependent signal sources would undergo a corresponding decrease whereas in the case of self-emission sources, full advantage can be taken of the lower background radiance conditions. It should be stressed that only the role of Rayleigh scattering has been considered in these calculations so that the presence of a solar-illuminated surface haze layer would result in a Mie scattering background intensity contribution which has not been included herein. In any event, it appears that as far as background considerations are concerned, distinct advantage is obtained with respect to the terrestrial atmospheric case for the performance of dayglow observations from the Martian surface.

For the earth case, it has been well established that twilight airglow observations contribute significant data to the aeronomy of the upper atmosphere. In the following discussions, reference is made to the performance of cogent twilight observations in both the zenith (β = 0) and horizon (or more appropriately at $\beta \approx 80^{o}$) directions. Accordingly, for subsequent reference it is convenient to derive a number of relationships involving the geometric parameters identified in Figure 37.

The twilight geometry pertinent to planetary atmospheres has been discussed in detail elsewhere (Ref. 54). For the simplified case where atmospheric refraction is neglected, a sharp shadow line AB prevails as shown in Figure 37. Under such conditions, it can be shown that for the zenith look-angle, $\beta = 0^{o}$ and small α-values,

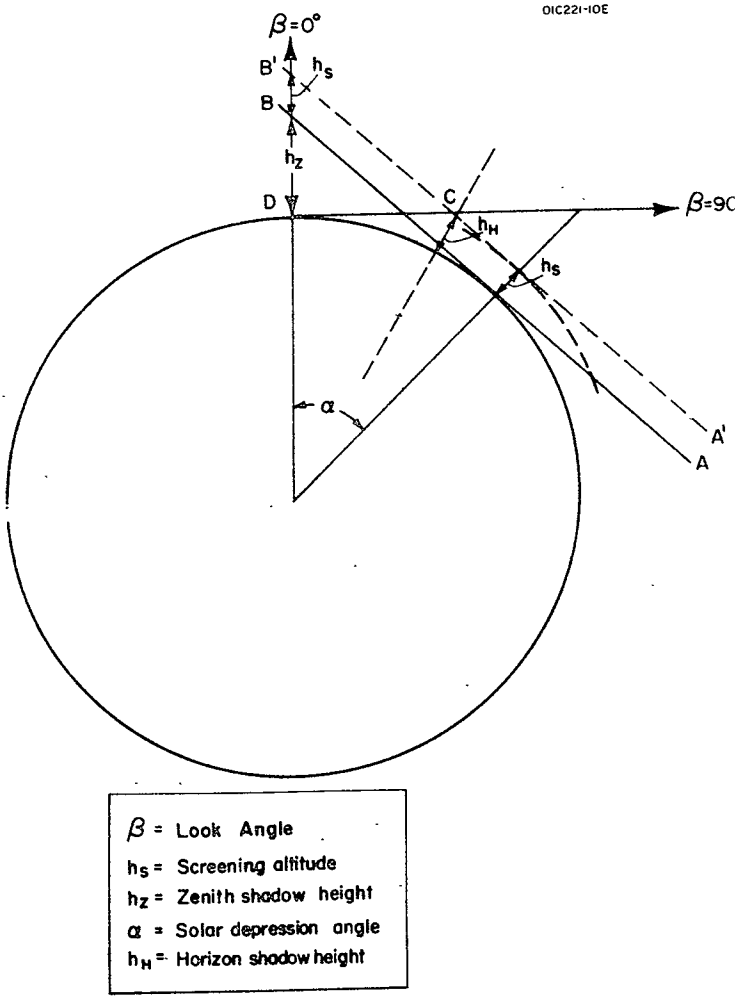

Figure 37. Geometry of the Martian airglow spectrophotometric scanning equipment.

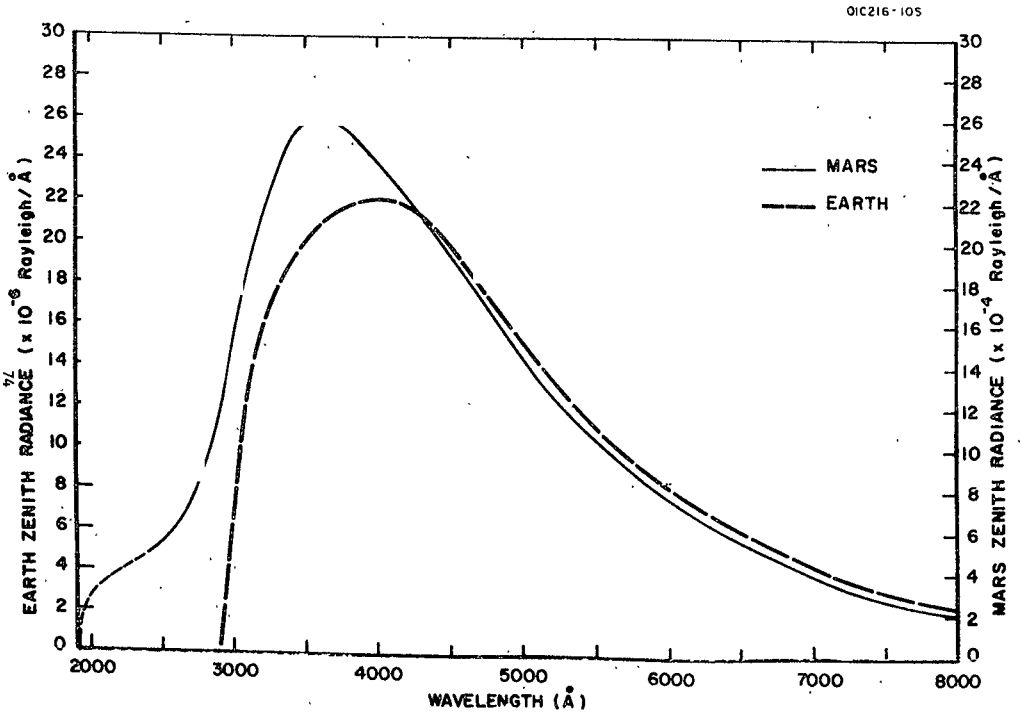

Figure 38 Zenith sky background radiances for Mars and Earth

$$h_z \approx \alpha^2 \quad \text{for earth} \tag{17}$$

$$2h_z \approx \alpha^2 \quad \text{for Mars} \tag{18}$$

In addition, for horizon observations performed along $\beta = 90^\circ$, the horizon illumination altitude, h_H as shown in Figure 37 was determined directly from geometric relationships. The zenith and horizon illumination altitudes, h_z and h_H respectively for Mars are shown in Figure 39 in terms of both the solar depression angle, α, in degrees, and in minutes.

Resultant zenith radiances are presented in Figure 40 in terms of Rayleighs/Å as a function of wavelength for $\lambda\lambda$ 2000-8000Å and a number of h_z-values ranging from 0-100 km. For convenience, the corresponding α-values are included on each h_z-curve. The horizon radiance in Rayleighs/Å is presented in Figure 41 as a function of solar depression angle. In this figure, the radiance calculations were performed for three representative wavelengths, namely 2000, 2500, and 3000Å since no significant attenuation occurs for $\lambda\lambda > 3000$Å where the screening height approaches zero km. The screening height, h_s results from attenuation along the twilight path indicated in Figure 37 as A'B'. In the case of Mars, significant attenuation occurs for $\lambda\lambda < 1975$Å where CO_2 absorption predominates. At higher wavelengths, the decreased attenuation is due only to atmospheric Rayleigh scattering by the major constituent model atmosphere gases, i.e., CO_2 and N_2. (Ref. 50). The sharp increase in h_s-values for $\lambda\lambda < 2000$Å shown in Figure 42 illustrates this point. In the present discussion, the h_s-values are small compared to the radius of the planet at all wavelengths $\lambda\lambda$ 2000-8000Å. Under this condition and for relatively moderate solar depression angles, it is appropriate to simply add the h_s and h_z-values to derive the effective altitude above which resident atmospheric constituents are fully solar illuminated under given twilight conditions. This is illustrated in Figure 37 by the altitude region above the point marked B'.

Estimates were made for the time duration of specific twilight conditions which obtain on both earth and Mars for comparison and reference. For the present purpose, an arbitrary twilight condition is defined for a change in solar depression angle, $\Delta\alpha$ from 1 to 18 degrees (which corresponds to astronomical twilight on earth). The time durations of this condition as a function of date at common latitudes were acquired for both planets. The data, pertinent to the case of earth was deduced directly from data contained in the American Ephemeris and Nautical Almanac. Although corresponding data for Mars were not readily available, they were calculated by application of the following expression

$$\Delta t_T = \left| \frac{\tau_o - \tau_T}{360/24.7} \right| \tag{19}$$

Δt_T = time duration for astronomical twilight = $\Delta\alpha$ = 0-18°, cos τ_o = -tan δ tan λ.

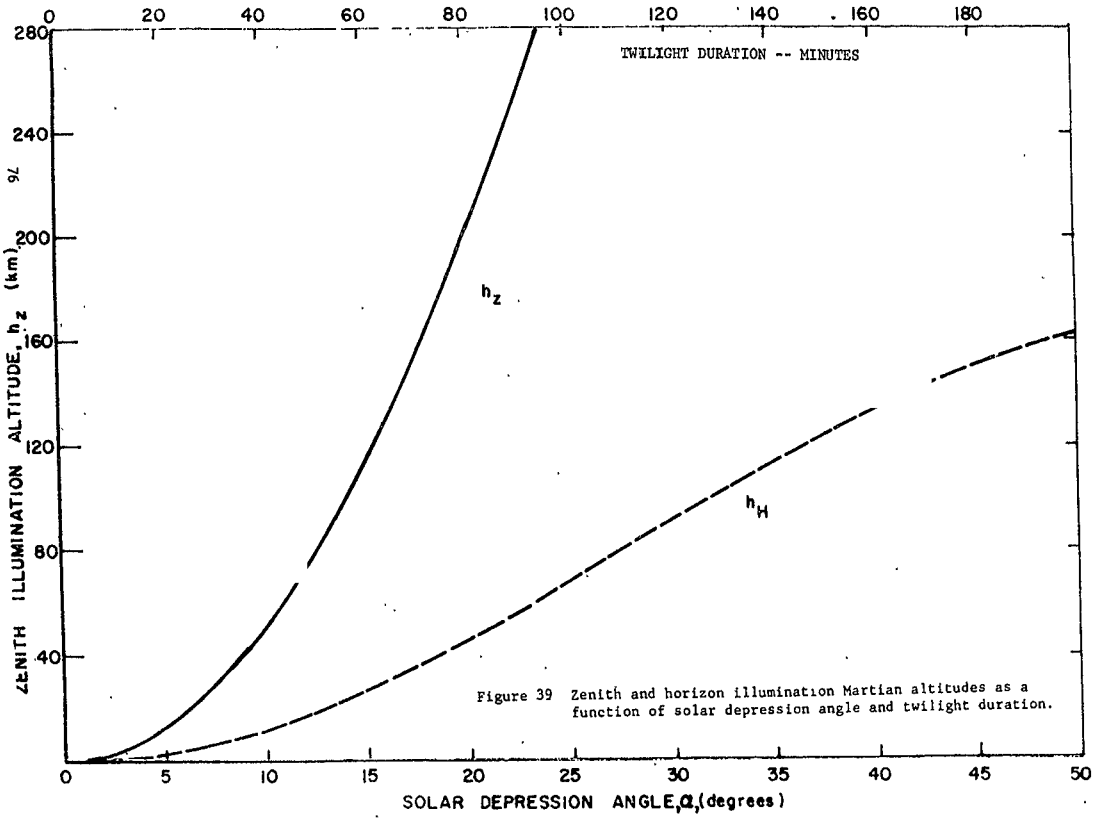

Figure 39 Zenith and horizon illumination Martian altitudes as a function of solar depression angle and twilight duration.

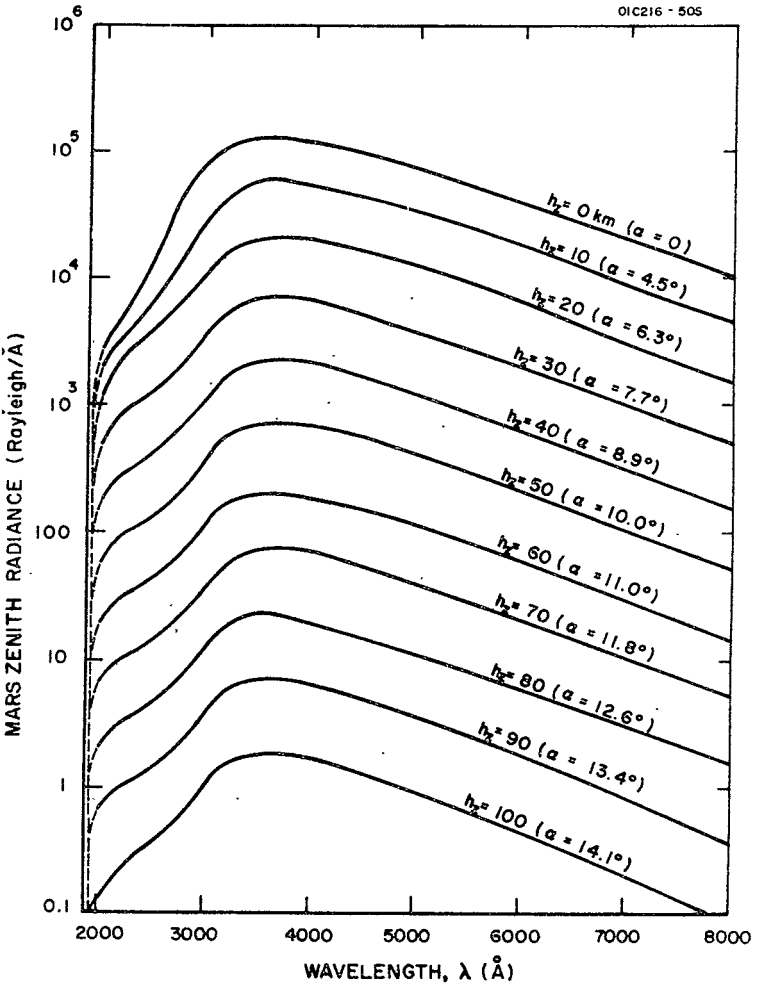

Figure 40. Zenith sky radiance as a function of wavelength for selected solar depression angles.

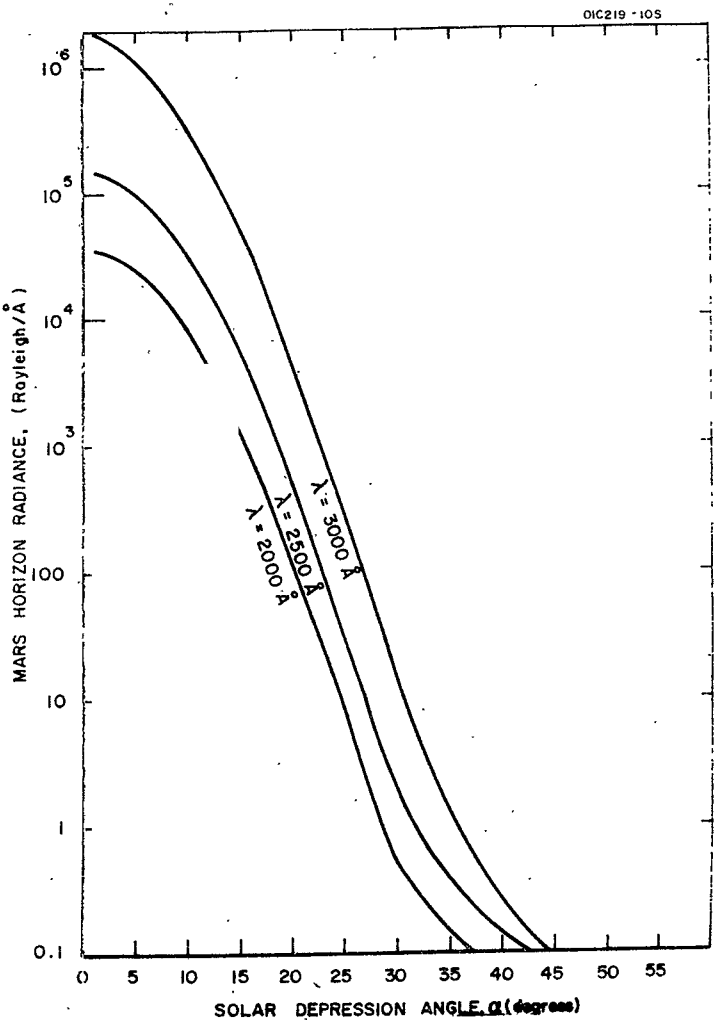

Figure41. Horizon sky radiance as a function of solar depression angle for λ = 2000, 2500, and 3000Å.

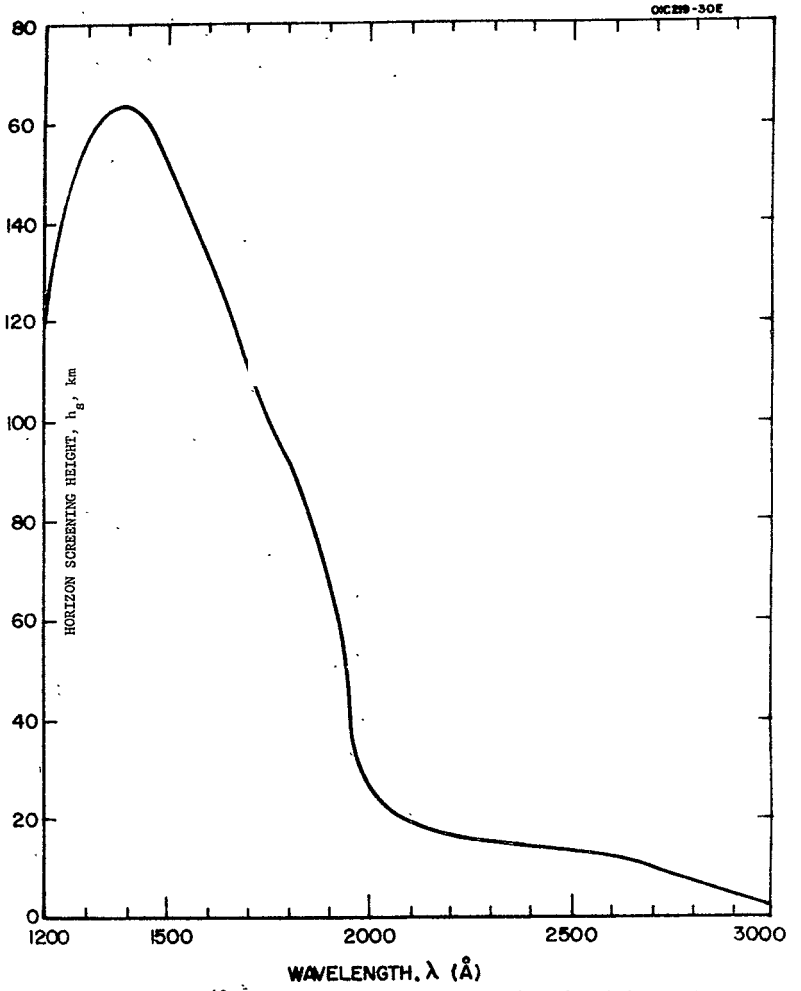

Figure 42. Screening height as a function of wavelength for Martian twilight.

$$\cos \tau_T = - \frac{\sin \delta \sin \lambda + \sin \alpha}{\cos \delta \cos \lambda} \qquad (20)$$

where δ = solar declination angle

λ = geographic latitude

and α = solar depression angle

The factor 360/24.7 relates to the rotation period pertinent to Mars.

The time duration of astronomical twilight ($\Delta\alpha$ = 0-18°) for the northern hemisphere of earth and Mars are shown in Figures 43 and 44 respectively. The similarity of the Δt_T-values for common latitude is striking although this behavior reflects the ensemble of pertinent planetary and orbital characteristics of the two planets.

In summary then, the following pertinent features can be noted: (a) for the spectral region $\lambda\lambda$ 3000-8000Å, the zenith sky radiance observed on the surface of Mars is about two orders of magnitude less than that which prevails on the earth's surface and that this background corresponds to that encountered from a platform located at a 30 km earth altitude, (b) for Mars, the spectral region of investigation can be extended down to 2000Å, (c) the time duration of specified twilight conditions for earth and Mars are similar, and (d) for given α-values, the shadow height on Mars is about half of the earth value, which allows increased observation time per unit altitude interval.

The relationships and results presented in Figures 37 through 44 inclusive will be referred to and employed as required in the following discussions which identify a number of possible signal sources which emit throughout the spectral region $\lambda\lambda$ 2000-8000Å.

Herein a number of possible signal sources are discussed and evaluated in order to illustrate the potential involved in performing the proposed Martian Lander spectrophotometric experiment. Owing both to the broad scope of the problems encountered and to the required brevity of the presentation, detailed discussions involving parameters which are of necessity somewhat speculative have been avoided. Thus, each signal source category discussed results in the illustration of the potential involved rather than in the recommendation of specific detailed selective experiments. A convenient format has been adopted which incorporates five categories: (1) Resonance Emission from Solar Illuminated Atoms or Ions in the Upper Atmosphere, (2) Fluorescence Emission from Solar Illuminated Molecules or Molecular Ions, (3) Airglow Radiations from Chemiluminescent Reactions between Atmospheric Constituents, (4) Absorption Owing to the Presence of Trace Constituents in the Lower Atmosphere of the Planet, and finally, (5) The Role of Particulate Scattering due to Dust and Haze in the Lower Atmosphere of Mars.

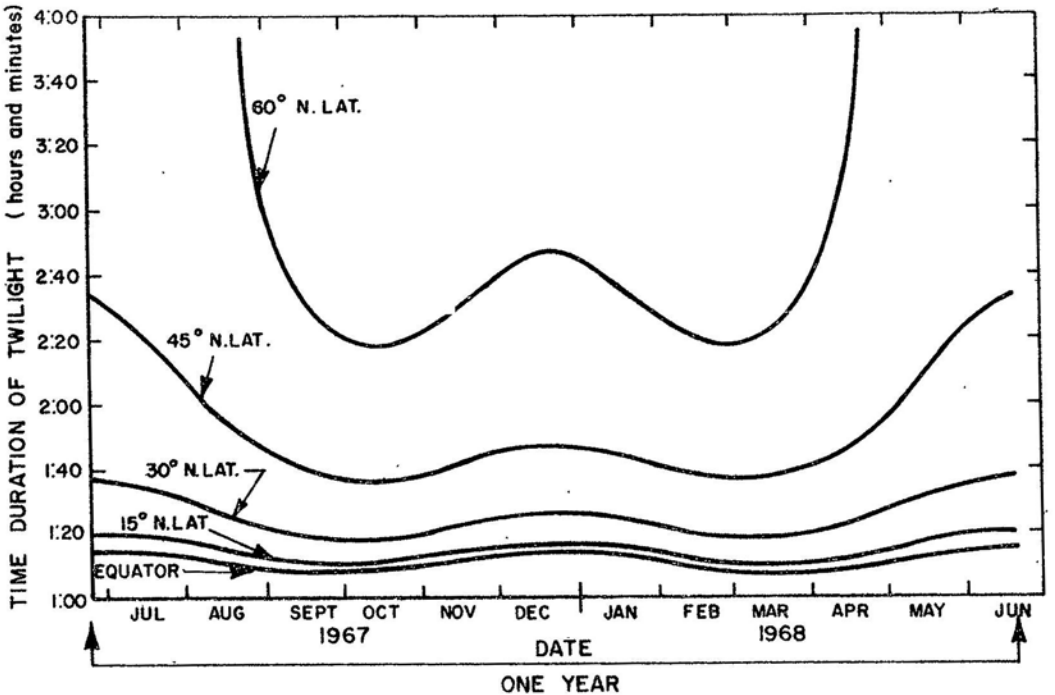

Figure 43. Time duration of twilight for Earth.

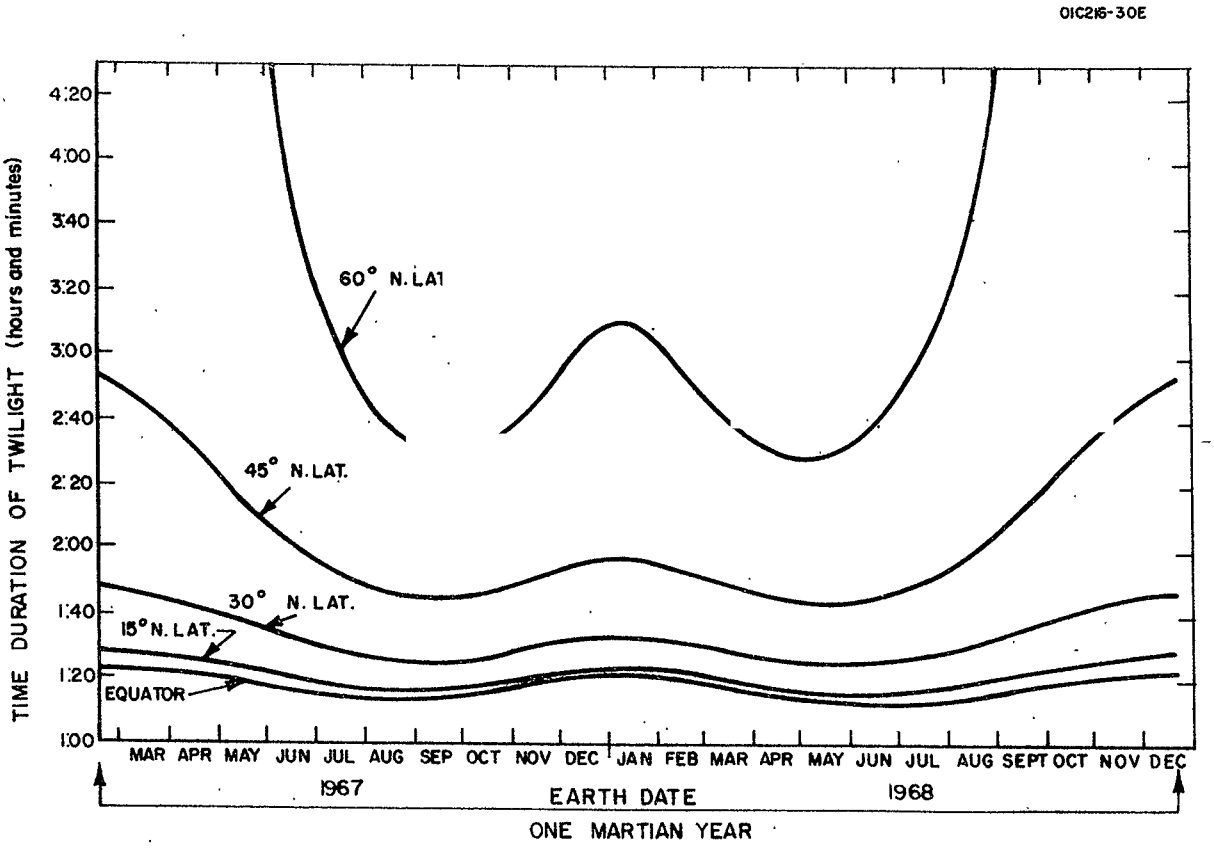

Figure 44. Time duration of twilight for Mars.

In general, atomic, ionic and metastable species in a planetary atmosphere reside in the upper altitudes owing to recombination processes which become more efficient with increasing number densities. The resultant high altitude profiles are particularly amenable to observations conducted under twilight conditions wherein the background radiation can be minimized without significant reduction in the signal intensity. This is not to say that full dayglow observations are precluded; thus for high signal intensity magnitudes, a program of dayglow observations may be warranted.

With certain simplifying assumptions for the case of resonance scattering by atoms or ion species

$$4\pi I = \pi F \frac{\pi e^2}{mc^2} \lambda^2 f\omega \frac{N}{\mu} \tag{21}$$

where $4\pi I$ = the emission rate in photons-cm^{-2}-sec^{-1}-Å^{-1} (one Rayleigh = 10^6 photons-cm^{-2}-sec^{-1})

πF = the solar flux in photons-cm^{-2}-sec^{-1}-Å^{-1}

λ = resonance wavelength

f = f-value or oscillator strength of the line

ω = the albedo for single scattering

N = number of atoms along the line of sight in atoms-cm^{-2}

μ = cos θ where θ is the angle between the illuminating and observing paths.

For the present purposes, it is convenient to define an emission probability factor, i.e, the number of photons scattered per second per solar illuminated atom:

$$g = \pi F \frac{\pi e^2}{mc^2} \lambda^2 f\omega \tag{22}$$

so that

$$4\pi I = g \frac{N}{\mu} \tag{23}$$

The detailed composition of the Martian atmosphere is unknown at present. However, even with the limited available data, one may speculate that an ensemble of possibilities exist for the production of neutral and metastable atoms and ions in the upper atmosphere. When solar illuminated, these species will re-emit at their characteristic signature resonance radiations which can represent possible signal sources of interest for $\lambda\lambda$ 2000-8000Å. Among the generation processes are included: ionospheric recombination, solar photodissociation, photoelectron and solar wind proton interaction with the atmospheric constituents, photochemical production of these species, etc. Under certain conditions, it can be expected that the resultant resonance signals could be highly intense. For example, in the terrestrial atmosphere case the $[OI]_{21}$-6300Å and the sodium-D-5890Å radiations (on the order of 20 kR) have been observed in full dayglow experiments by Noxon and Goody (Ref. 55) and Donahue (Ref. 56) respectively, in spite of the intense earth background radiations shown in Figure 38 at these spectral positions. Since the corresponding background intensities pertinent to Mars are two orders of magnitude lower, it is evident that in the proposed Martian surface experiment similar and lesser emission intensities could be observed in the dayglow. Another possible source of atmospheric atoms and ions results from the deposition and subsequent observation of interplanetary debris in the upper atmosphere of Mars. This latter source is singled out for more detailed discussion in order to illustrate the potential involved.

Interplanetary debris represents an important source of minor constituent atoms and ions in the upper atmosphere of the earth. The identity and inventory of these debris atoms and ions have been experimentally conformed for Na^+, Mg^+, $A\ell^+$, Ca^+, Fe^+ and Si^+ (Ref. 57) by direct in-situ measurements and also for Ca^+, Na, K and Li (Ref. 58) by ground-based photometric twilight observations. The observed atomic number density-altitude profiles typically peak in the vicinity of 100 km with a sharp cutoff occurring at lower altitudes due to the occurrence of oxidation processes. It may be speculated that a somewhat similar situation obtains in the upper atmosphere of Mars. In fact, on the basis of an analysis performed by Marmo and Brown (Ref. 59), it has been shown that assuming equivalent debris influx rates, for the case of Mars the peak number density would be larger (due to the limited oxidation processes compared to earth) and also it would occur at altitudes in the vicinity of 80 km. In any case, it appears reasonable to search for the presence of these debris species in the upper atmosphere of Mars. To emphasize this possibility, the following preliminary analysis was performed.

First, a number of possible debris constituents were selected on the basis of two criteria: (a) that they possess a relatively high chemical abundance in typical meteors (Ref. 60), and (b) that their resonance wavelengths are located at $\lambda\lambda > 2000$Å (Ref. 61). The selected debris atoms and their corresponding resonance wavelengths are presented in columns 1 and 2, respectively of Table 3. From readily available data (Refs. 61,62) corresponding g-values were calculated as shown in column 3

TABLE 3

Relative Emission Probability - Abundance Factors (gC-values), for Solar Illuminated Meteoric Debris Atomic and/or Ionic Species in the Martian Atmosphere

Debris Species	Resonance Wavelength Å	$g\left(\frac{\text{photon}}{\text{sec-atom}}\right)^{*}$	gC-values**
Aℓ I	3082	7.6(-2)	2.6(-1)
Ca I	4227	1.0(-2)	1.7(-2)
Ca II	3933	1.4(-1)	
Fe I	3441	7.6(-3)	6.0(-1)
Fe II	2599	2.2(-2)	
K I	7699	1.2(-1)	1.4(-1)
Li I	6708	4.4(0)	1.6(-2)
Mg I	2852	1.0(-1)	3.2(0)
Mg II	2796	3.1(-2)	
Na I	5890	6.4(-1)	1.0(0)
Ni I	3370	8.2(-2)	7.9(-2)
Si I	2514	6.0(-3)	2.1(-1)
Ti I	3342	4.0(-2)	3.4(-2)

* Values in parenthesis are raised to that power of ten

** gC-values are relative to a value of unity for sodium

of Table 3. Relative signal intensity estimates can be derived for the tabulated species as follows. First, it is assumed that the deposited inventory of the upper atmospheric debris species is equivalent to its chemical abundances in typical meteors. Then if C represents this abundance parameter , the product gC-values in column 4 of Table 3 are measures of the expected relative signal intensities. It is convenient to normalize these values to sodium which is assigned an arbitrary value of unity. As noted previously, a representative earth value for the Na-D-5890Å dayglow can be taken as about 20 kR (Ref. 54). If this signal intensity value is employed as a reasonable estimate for the Mars dayglow, it follows that all the species indicated in Table 3 should be readily observable under certain specified conditions (of both dayglow and twilight airglow) encountered during the conduct of the suggested experimental program.

Molecules and molecular ions which may represent sources of Martian atmospheric emission included the following candidates: CO, NO, O_2, N_2, OH, CN, N_2^+, O_2^+, CO^+, CO_2^+, and others. Therefore, the resultant fluorescence over the spectral region of interest λλ 2000-8000Å owing to the initial absorption of solar radiation by these molecules constitutes another signal source which is evaluated in the following discussion.

The molecular case is more complex than its atomic analog discussed previously although the single scattering theory for atoms may be adapted readily for application to diatomic molecules. The expression which describes single molecular photon scattering is analogous to Equation (21) for atomic species and is given by:

$$4\pi I_{v'v''} = \pi F_{v'o} \frac{\pi e^2}{mc^2} \lambda^2_{v'o} f_{v'o} \omega_{v'v''} \frac{N_o}{\mu} \qquad (24)$$

where the v'v" subscripts emphasize the fact that the initial absorption may occur in one electronic-vibrational transition while the subsequent fluorescence may occur at longer wavelengths involving other electronic-vibrational transitions. In the above expression, the F, f, and λ-values have subscripts v'o to indicate involvement of the absorption band of the lowest vibrational level (v" = 0) of the ground electronic state. The N_o-value indicates that the participating molecules generally reside at the lowest vibrational level of the ground state. As a further analogy to the case of atoms, the emission probability factor for molecular fluorescence may be expressed as

$$g_{v'v''} = \pi F_{v'o} \frac{\pi e^2}{mc^2} \lambda^2_{v'o} f_{v'o} \omega_{v'v''} \qquad (25)$$

so that

$$4\pi I_{v'v''} = g_{v'v''} \frac{N_o}{\mu} \qquad (26)$$

In general, the pertinent molecular f-values are not available so that the corresponding $g_{v'v''}$-factors are not readily calculable. However, the relative intensity distribution of the molecular resonance and fluorescent bands can be deduced for an optically thick atmosphere on the basis of the published theoretical results of Chamberlain and Sobouti (Ref. 63). They have shown that for this case

$$4\pi I_{v'v''} = \pi F_{v'o}\, \omega_{v'v''}\, \Delta\lambda\, \frac{\mu_o}{\mu}\, H(\mu_o) \qquad (27)$$

where $H(\mu_o)$ are tabulated functions by Chandrasekhar (Ref. 64) and $\Delta\lambda$ is the effective line-width (Ref. 63). Thus, the relative intensities of both the resonance and fluorescence bands are proportional to the solar flux, $F_{v'o}$ and the albedo for single scattering, $\omega_{v'v''}$. The $f_{v'o}$-values are not involved in Equation (27) since the solar flux penetrates into the optically thick atmosphere to saturate the bands. If the $\Delta\lambda(\mu_o/\mu)H$-value is assigned the value of unity, then

$$4\pi I_{v'v''} \approx \pi F_{v'o}\, \omega_{v'v''} \qquad (28)$$

which yields reasonable signal estimates for the optically thick case, as well as indicating the relative intensities in a given fully solar illuminated band system.

A number of pertinent parameters for several possible molecular constituents in the Martian atmosphere are summarized in Table 4. The band systems are identified and the appropriate electronic transitions are indicated in column 2 while column 3 includes some selected v'v'' transitions and their corresponding λ-values as presented by Barth (Ref. 65). In each case, the initial absorption (i.e., $v' = 0$) transition can be identified easily while the subsequent fluorescent emissions were selected on the basis of their relative efficiency over the spectral region $\lambda\lambda > 2000$Å. In accordance with Equation (28), the $4\pi F_{v'o}\omega_{v'v''}$-values corresponding to the selected fluorescent emission bands are presented in column 4 of the table. At best, these values represent maximum signal estimates which can be expected to be reduced significantly in practice for specific cases. Finally, some general comments are presented in column 6 which are pertinent to each of the individual transitions.

Detailed evaluation of the probability of observing any specific emission indicated in the table would require a complex analysis where much of the basic input data which at this point are at best speculative or just not available. For example, it is important to ascertain whether a particular molecular constituent is well-mixed or is resident in layer form in the upper Martian atmosphere. It can be assumed that the major model atmospheric constituents, N_2 and CO_2 are mixed, while for such

TABLE 4

Molecular Constituent	Band System Transition	Absorption-Fluorescence Transition v'-v''	λ	$F_{v'o}^{\omega}$ - value, photons/cm^2/sec/Å	Comments
CO	4th Pos. System $A\ ^1\Pi - X\ ^1\Sigma^+$	5-0	1393	2.8 (7)	Allowed Transition Screening height for 1393Å ≈ 160km (see Fig.)
		5-11	2012	1.5 (7)	
		5-12	2089	1.8 (7)	
		5-13	2172	1.1 (7)	
	Hopfield-Birge Bands $a'\ ^3\Sigma^+ - X'\ ^1\Sigma^+$	0-0	1804	2.9 (6)	Forbidden Transition Screening height for 1804Å ≈ 90km
		0-5	2223	1.1 (9)	
		0-6	2327	1.3 (9)	
		0-7	2440	1.3 (9)	
	Cameron Bands $a\ ^2\Pi - X\ ^1\Sigma^+$	0-0	2063	2.3 (10)	Forbidden Transition Screening height for 2063Å ≈ 20km Very rich fluorescence spectrum for λλ 2000-2800Å (a)
		0-1	2158	2.8 (10)	
NO	Gamma Bands $^2\Sigma^+ - X\ ^2\Pi$	0-0	2262	5.9 (10)	Allowed Transition Screening height for 2262Å ≈ 15km Screening height for 2149Å ≈ 15km
		0-1	2363	8.2 (10)	
		1-0	2149	9.8 (10)	
O_2	Schumann-Runge $B\ ^3\Sigma_u^- - X\ ^3\Sigma_g^-$	0-0	2026	8.0 (2)	Allowed Transition Screening height for 2026Å ≈ 20km Fluorescence spectrum rich in bands for λλ 1700Å - 4000Å (b)
		0-12	3105	8.0 (9)	
		0-13	3234	8.8 (9)	
	Herzberg Bands $A\ ^2\Sigma_u - X\ ^3\Sigma_g^-$	0-0	2885	2.4 (7)	Forbidden Transition Screening height for 2885Å ≈ 5km Fluorescence spectrum rich in bands for λλ 2400-5000Å (c)
		0-8	4370	3.8 (11)	
		0-9	4647	3.9 (11)	
		0-10	4955	3.2 (11)	

Molecular Constituent	Band System Transition	Absorption-Fluorescence Transition $v'v''$	λ	$F_{v'o}\omega$ - value photons/cm^2/sec/Å	Comments
N_2	Vegard-Kaplan Bands $A\ ^2\Sigma_u^+ - X\ ^1\Sigma_g^+$	0-0 0-4 0-5 0-6	2010 2463 2605 2762	7.8 (7) 8.5 (9) 1.0 (10) 9.7 (9)	Forbidden Transition Screening height for 2010Å ≈ 20km
	Hopfield-Birge Bands $b\ ^1\Pi_u - X\ ^1\Sigma_g^+$	0-0	986		Allowed transition Screening height for 986Å > 200km No significant fluorescence for $\lambda > 2000$Å
	Lyman-Birge-Hopfield Bands $a\ ^1\Pi_g - X\ ^1\Sigma_g$	0-0 0-9 0-10 0-11	1450 2040 2130 2227	1.5 (7) 5.0 (4) 7.1 (3) 7.3 (2)	Forbidden transition Screening height for 1450Å ≈ 150km Photon emission flux for $\lambda > 2000$Å too weak to observe
OH	Hydroxyl UV Bands $A\ ^2\Sigma^+ - X\ ^2\Pi$	0-0 1-0	3064 2811	4.0 (12) 5.4 (11)	Allowed transition The g-values for the transitions 0-0, and 1-0 are 8.6 (-4) and 2.4 (-5) photon-sec-atom respectively (d)
CN	Cyanogen Violet Bands $B\ ^2\Sigma^+ - X\ ^2\Sigma^+$	0-0 1-0	3876 3582	8.1 (12) 9.2 (11)	Allowed transition The g-values for the transitions 0-0, and 1-0 are 7.4 (-2) and 7.3 (-4) photon-sec-atom respectively (e)
N_2^+	First Negative Bands $B\ ^2\Sigma_u^+ - X\ ^2\Sigma_g^+$	0-0	3914	6.4 (12)	Allowed transition From published f-values, 4×10^{10} ion-cm^2 results in signal intensity of 1 kR.

Molecular Constituent	Band System Transition	Absorption-Fluorescence Transition v'v''	λ	$F_{v'o}\omega$ - value photons/cm^2/sec/Å	Comments
O_2^+	Second Negative System $A\ ^2\Pi_u - X\ ^2\Pi_g$	0-0 11-0 11-1	2610 2153 2242	8.0 (6) 2.0 (10) 6.0 (10)	Allowed transition Screening height for 2610 ≈ 15km
CO^+	First Negative Band $B\ ^2\Sigma^+ - X\ ^2\Sigma^+$	0-0	2191	1.4 (11)	Allowed transition Screening height for 2191Å ≈ 15km The g-value for the transition 0-0 is 1.2 x 10^{-4} photons-sec-atom (f)
	Comet Tail Bands $A\ ^2\Pi - X\ ^2\Sigma^+$	0-0 0-1	4900 5487	2.2 (12) 5.5 (12)	Allowed transition The g-value for the transition 2-0 is 1.3 x 10^{-3} photon-sec-atom (g)
CO_2^+	Fox, Duffendale and Barker Comet Bands $^2\Pi_u - X\ ^2\Pi_g$		3378 3505 3674	5.0 (11)* 5.0 (11) 5.0 (11)	Allowed transition Intense bands seen in comets by fluorescence radiation. (h) Believed to be initially excited by λ ≈ 2800Å; screening height ≈ 5km.

(a) Barth, C. A., UV Spectroscopy of Planets, JPL TR No. 32-822 (December 15, 1965)(see Figure 20)
(b) Ibid, see Figure 5
(c) Ibid, see Figure 8
(d) Ibid, see Table X
(e) Ibid, see Table XI
(f) Lawrence, G. M., Journal of Quantitative Spectroscopy and Radiative Transfer, 5, No. 2, 359 (1965)
(g) Dalby, F. W., Handbuch der Physik, 27, 464 (1964)
(h) Dufay, M. and Poulizac, M. C., Memoires de La Societe Royales de Sciences de Liege, pp. 427 (c.1966)

species as OH, CN, N_2^+, O_2^+, CO^+, and CO_2^+ layering could be invoked. Furthermore, for such molecules as CO, NO, and O_2 the atmospheric distribution question can not be answered at this time. Additionally, an important factor in evaluation of twilight observation of molecular fluorescence involves the horizon screening height shown in Figure 42 and discussed in the next section. For example, if the initial absorption occurs at a wavelength of about 1400Å, (i.e., see the 4th positive 5-0 transition for CO in Table 4) the resultant screening height is approximately 160 km. When this value is added to the h_z-values of Figure 40, it is evident that the column count of solar-illuminated CO molecules is relatively limited. Accordingly, under certain conditions it may be advantageous to select absorption transitions which involve relatively long wavelengths and correspondingly lower screening heights. Additionally, it should be noted that unless the molecular constituent resides in an atmospheric layer configuration, the performance of twilight measurements may not be particularly advantageous. Alternatively, the performance of both day and twilight airglow experiments could provide data from which the existence of either the mixing or layering configuration could be ascertained. Finally, the role of quenching must be considered for relatively low altitude airglow phenomena. This is especially true in cases where forbidden transitions (i.e., long lifetimes) are involved.

Many of the transitions specified in Table 4 can result in fluorescence caused by the interaction of photoelectrons in the upper atmosphere of Mars. It should be noted that in the earth case for certain constituents, this phenomena represents the major emission factor so that its effect on Mars should also be recognized. However, this well known additive source function is not stressed here since it is a tractable problem so long as the appropriate data are available.

On the basis of the foregoing discussions, and the data presented in Table 4, it is evident that the definition of specific measurements is an extremely complex matter. However, with appropriate effort, some selectivity for the ensemble of possibilities in Table 4 could be made in order to isolate the more promising cases. For the present purposes, this task is considered to lie beyond the scope of this presentation.

In summary, then, it is felt that the data shown in Table 4 and the foregoing discussions indicate the potential of performing fluorescence experiments in the spectral region $\lambda\lambda > 2000$Å, in order to identify a number of possibly important molecular constituents in the Martian atmosphere and ionosphere.

It is conjectured that various possibilities exist for the generation of chemiluminescent atomic and molecular emissions due to reactions between ambient chemical constituents in the Martian atmosphere. As an example of the former (atomic emissions), chemiluminescence may result typically

from the debris species enumerated in Table 3 by mechanisms related to those which photochemically produce the nighttime sodium-D lines observed in the earth's atmosphere. In addition, twilight and night airglow emissions at 6300, 6364, 5199Å, etc. may be produced from a variety of processes which include photodissociation, recombination, photoionization, electron and proton impact, etc. Concerning molecular system chemiluminescence, it has been suggested that a significant portion of the terrestrial night airglow is attributable to the production of NO_2^* produced by the reaction between NO and O. This process as well as a similar one involving CO and O may occur in the Martian atmosphere. These latter two possibilities are discussed in a more detailed evaluation below where resultant order of magnitude signal intensity estimates are derived.

Inn (Ref. 66) first suggested that the blue haze observed on Mars may be due to chemiluminescence from a reaction involving CO and O which resulted in the production of excited CO_2^*. The subsequent emission from this excited species resides in a band system in the spectral region $\lambda\lambda$ 3200-6000Å with a peak intensity occurring at a wavelength of 4000Å. The spectrum was photographed and classified by Mahan and Solo (Ref. 67) who reported that this system consisted of 250 bands with relatively little continuum background. Inn (Ref. 66) employed a photochemical equilibrium model (using local number densities for $[CO] = [O] = 10^{12}$ cm^{-3} at an altitude of about 100 km) and the chemiluminescence efficiency data of Clyne and Thrush (Ref. 68) to estimate a total band system brightness of about 20 kR. On the basis of this value and the spectral distribution observed by Mahan and Solo (Ref. 67), it can be estimated that the signal brightness of the most intense band of the system could amount to about 1 kR. A signal intensity of this magnitude would be easily detectable under the appropriate twilight conditions (see Figures 40 and 41).

With respect to the possibility of observing the NO_2^* emissions in the twilight or night airglow, it is necessary to establish an upper limit value for NO in the Martian atmosphere. Marmo and Warneck (Ref. 69) have shown recently that under thermodynamic equilibrium an NO/O_2 ratio greater than 1 obtains throughout the mixed region of the Martian atmosphere. Additionally, Belton and Hunten (Ref. 70) experimentally established an upper limit value for O_2 of about 20 cm-atm. or about 5.4×10^{20} cm^2 column in the Martian atmosphere. If this value is also applied to the case of NO, then a mixed atmosphere, at an altitude of about 100 km the local number density of NO, $[NO] \approx 10^{11}$ cm^{-3}. Jonathan and Doherty (Ref. 71) have demonstrated that the chemiluminescence efficiency for the NO_2^* emissions is about 2000 times greater than that measured for the CO_2^* throughout the investigated spectral ranges. Thus, it is evident that under conditions similar to those specified by Inn (Ref. 66) (i.e., where $[O] = 10^{12}$ cm^{-3}) the resultant chemiluminescent signal intensity may be as large as 4×10^3 kR. However, it should be noted that this latter value

is predicated on the photon emission rate over the entire continuum which extends over a spectral interval of about 2000Å. Thus, on a unit spectral interval basis, the average chemiluminescence signal amounts to about 2 kR/Å. However, since the continuum peaks around 6200Å, observations conducted at this spectral position can be expected to amount to about an order of magnitude greater or about 20 kR/Å. Clearly, such signal magnitudes could be observed easily during the course of the proposed experiment. However, in reality the local NO number density at a Martian atmosphere altitude of 100 km is probably less than 10^{11} cm^{-3} so that a concommitant reduction in signal intensities would result.

Finally, with respect to the two chemiluminescent reaction examples discussed above, it should be noted that the pertinent chemical consumption rates are such that the active constituent number densities are essentially conserved throughout the night. Under these minimum background intensity conditions, it is evident that a sensitive technique is available for positively observing and identifying these emissions and subsequently establishing meaningful upper limit values for the constituents involved.

In this section is described an experimental technique designed to detect, identify, and measure the altitude profiles of minor constituent absorbing species in the lower atmosphere of Mars. For this purpose, twilight measurements are performed to measure the irradiances of both the zenith and horizon directions. It will be demonstrated that these irradiances are sensitively perturbed by the presence of absorbing trace constituents in the lower atmosphere of Mars. This technique involves the following advantages: (a) the detection capability is enhanced by about a factor of 25 greater than that available with currently employed techniques; (b) the unambiguous identification of the constituent involved is possible owing to its absorbing characteristic for $\lambda\lambda > 2000$Å; and finally (c) the species altitude distribution can be ascertained on the basis of the geometric factors involved in the performance of cogent twilight experiments.

As discussed previously, the Martian atmosphere is essentially transparent to solar zenith radiation for wavelengths above about 2000Å as shown by the results of Figure 38 and confirmed by the recent observations of Evans (Ref. 72). On this basis, it is possible to experimentally establish upper limit vertical column count values for any gas which absorbs radiations of wavelengths greater than 2000Å. For example, employing the measured absorption cross sections for ozone in this spectral region (Ref. 52), a corresponding upper limit vertical count value of about 1×10^{17} cm^2 column can be established. Identification of the existence and establishment of the upper limit estimate of the content of this particular constituent has important implications on both aeronomic and biological processes occurring in the Martian atmosphere.

Similarly, upper limit values can be established for other potentially important species which exhibit distinctive absorption features. The

absorption curves for a number of such potentially important candidate species which qualify in this regard are presented in Figures 45, 46, and 47 over the spectral region λλ 2000-3000Å. These data were extracted directly from Calvert and Pitts (Ref. 73). It should be noted that the curves pertinent to inorganic species are presented in Figure 45 which the absorption characteristics of several interesting organic materials, which may be related to biological interests, are shown in Figures 46 and 47.

With respect to the data of Figure 45, it should be noted that in biological processes, H_2O_2 is required to oxidize both sulfides and certain carbon compounds to simple sulfates and carbonates. In addition Marmo and Warneck (Ref. 69) have demonstrated that SO_2 or H_2S can participate as precursor sources for sulfur in the photochemical generation of sulfur containing amino acids in the Martian atmosphere. Marmo and Warneck (Ref. 69) have also shown that, in the Martian atmosphere, a thermodynamic relationship obtains for the NO/O_2 ratio, which can be further related to the content of NO_2, N_2O, and $NOC\ell$ so that the presence of these constituents may involve both important aeronomic and biological implications. For inorganic gases, a number of additional candidate species have been enumerated previously in Table 4 where appropriate absorption ($v'' = 0$) bands are shown to occur at $\lambda > 2000$Å for several transitions.

Absorbing gases (for $\lambda\lambda > 2000$Å) which may be present in the lower Martian atmosphere may act as photosensitizers to allow solar photolysis of CO_2, HOH, organics, and other molecules which do not absorb the relatively intense solar flux in this spectral region. For example, although CO_2 and water vapor do not absorb strongly in this region, the invocation of photosensitization by an absorbing species (i.e., SO_2, H_2S) could result in the photolysis of these species and subsequent generation of several simple organic molecules which may have important implications on the exobiology of Mars. In fact, several compounds possibly produced by the above mechanism are also represented in the life-cycle. Characteristically, simple organic compounds often absorb strongly in the region λλ 2000-3000Å as illustrated by the data of Figures 46 and 47 pertinent to a variety of formaldehydes, ketones, organic acids, hydrides, and esters. Calvert and Pitts (Ref. 73) present a number of photolytic mechanisms involving these and other organic materials, the products of which would undoubtedly be important to Martian biological investigations. The detection of these or other organic materials does not intrinsically assure a biological origin, although the presence of these constituents could represent and possibly be identified with key residue materials of biological processes. In this regard, it would be or particular value to review the experimental requirements and expected results of complementary exobiological experiments aboard the Martian Lander.

The salient features of an atmospheric absorption measurement experiment can be discussed both in terms of the geometry illustrated in Figure 37 and the corresponding twilight zenith and horizon radiances presented

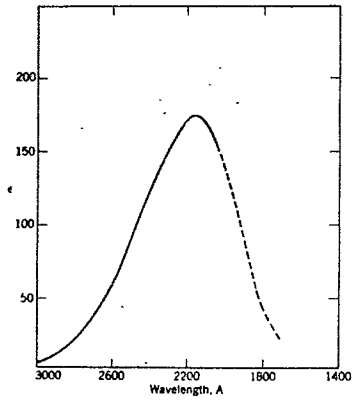

Absorption spectrum of HI. From Romand.

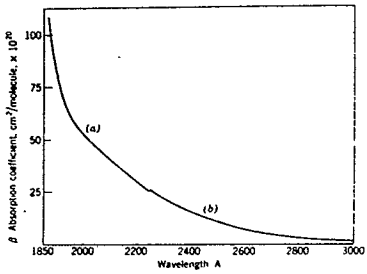

The absorption spectrum of H_2O_4 vapor, the absorption coefficient β is defined by $\beta = 2.303 \log (I_0/I)/nl$, where n is the concentration in molecules/cubic centimeter and l the path in centimeters. From Volman[56] originally from Refs 55 (curve *a*) and 56 (curve *b*)

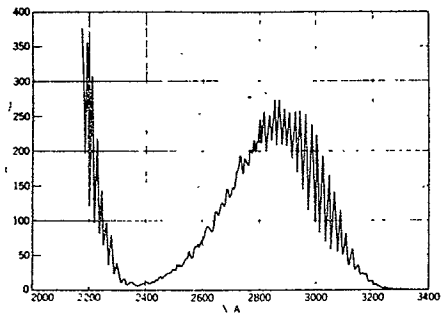

The absorption spectrum of $SO_3(g)$, 25°. Spectra determined by Mrs. Veronique McMillan

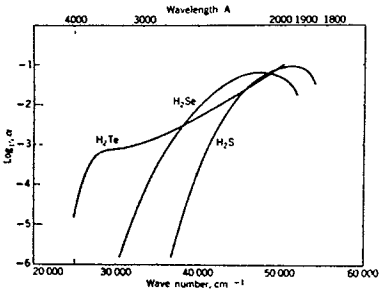

The absorption spectrum of H_2S, H_2Se, and H_2Te, the absorption coefficient $\alpha = [\log (I_0/I)]/p(\text{atm})l(\text{cm})$. From Rollefson and Burton,[56b] p. 179, originally from Goodeve and Stein

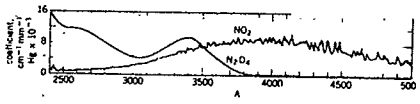

Absorption spectrum of nitrogen dioxide, NO_2, and dinitrogen tetroxid O_4, at 25° corrected to pure compound spectra. From Hall and Blacet

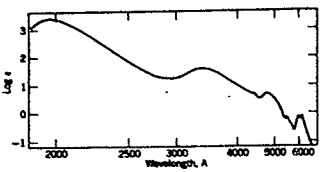

Absorption spectrum of nitrosyl chloride, NOCl. From Goodeve and Katz.

Figure 45 Absorption spectra of selected inorganic molecules.

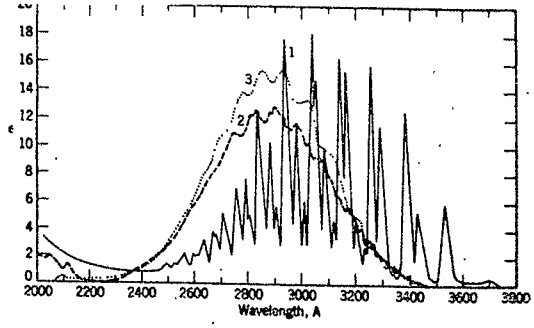

Absorption spectra for (1) formaldehyde [$CH_2O(g)$], ~75°; (2) acetaldehyde [$CH_3CHO(g)$], 25°; (3) propionaldehyde [$C_2H_5CHO(g)$], 25°.

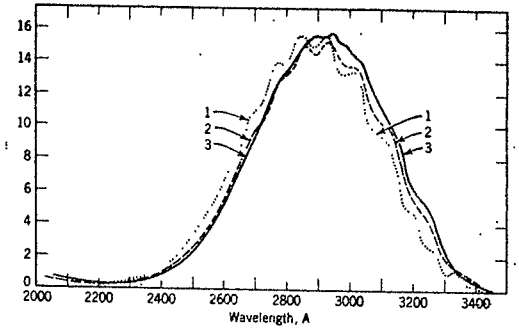

Absorption spectra for (1) propionaldehyde [$C_2H_5CHO(g)$], 25°; (2) *n*-butyraldehyde [*n*-$C_3H_7CHO(g)$], 25°; (3) isobutyraldehyde [iso-$C_3H_7CHO(g)$], 25°.

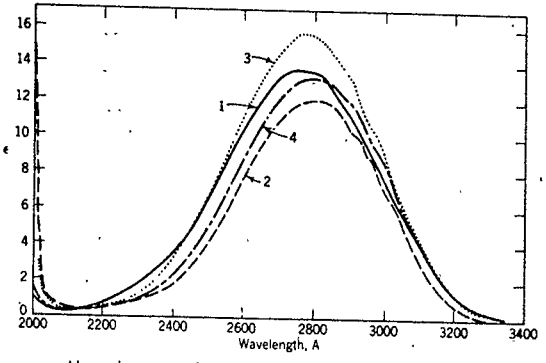

Absorption spectra for (1) acetone [$CH_3COCH_3(g)$], 25°; (2) diethyl ketone [$C_2H_5COC_2H_5(g)$], 25°; (3) methyl ethyl ketone [$CH_3COC_2H_5(g)$], 25°; (4) methyl-*n*-butyl ketone [$CH_3CO(CH_2)_3CH_3(g)$], 25°.

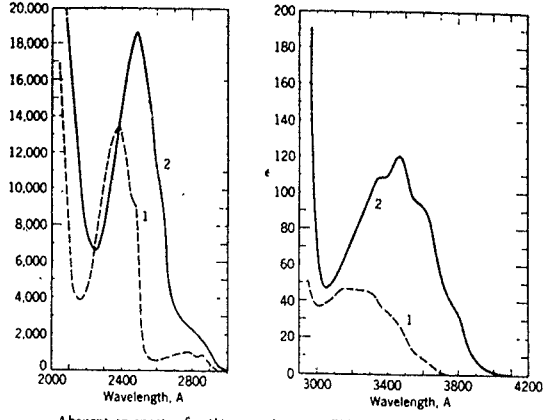

Absorption spectra for (1) acetophenone ($CH_3COC_6H_5$) in cyclohexane, 25°, (2) benzophenone ($C_6H_5COC_6H_5$) in cyclohexane, 25°.

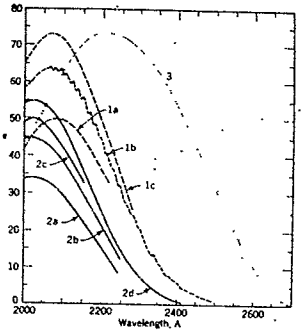

Absorption spectra for (1) formic acid [$CHO_2H(g)$] 27 (a) 2.45 mm, (b) 16.4 mm, (c) 35.2 mm, undefined amount of monomer and dimer contribute, calculated assuming monomer only. (2) acetic acid [$CH_3CO_2H(g)$] 26 (a) 3.6 mm, (b) 8.3 mm, (c) 11.0 mm (d) 12.9 mm, calculated assuming monomer only; (3) acetic anhydride [$(CH_3CO)_2O(g)$], 25°.

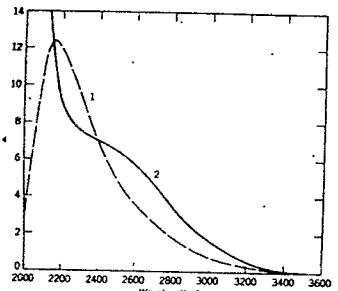

Absorption spectra of
(1) dimethyl peroxide [$CH_3OOCH_3(g)$], from Takezaki, Miyazaki, and Nakahara,[178]
(2) di-*tert*-butyl peroxide [$(CH_3)_3COOC(CH_3)_3(g)$], 25°

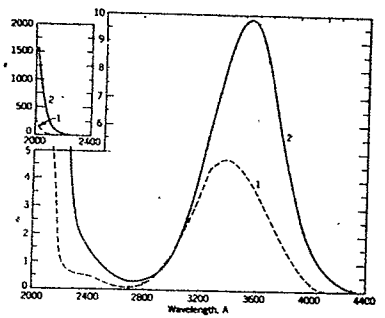

Absorption spectra of (1) azomethane [$CH_3N{=}NCH_3(g)$], 25°; (2) [$C_2H_5N{=}NC_2H_5(g)$] 25°

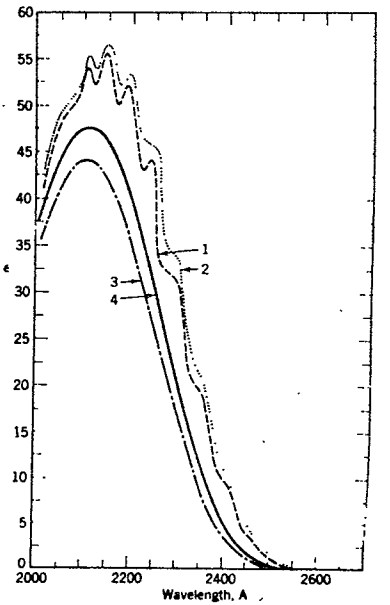

Absorption spectra for:
(1) methyl formate [$CH_3O_2CH(g)$], 25°;
(2) ethyl formate [$C_2H_5O_2CH(g)$], 25°;
(3) methyl acetate [$CH_3O_2CCH_3(g)$], 25°;
(4) ethyl acetate [$C_2H_5O_2CCH_3(g)$], 25°

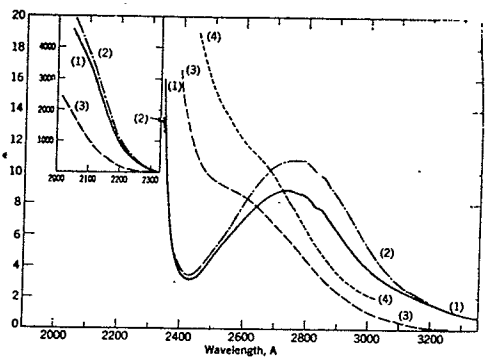

Absorption spectra of (1) nitromethane [$CH_3NO_2(g)$], 25°; (2) nitroethane [$C_2H_5NO_2(g)$], 25°, (3) methyl nitrate [$CH_3ONO_2(g)$], 25°; (4) ethyl nitrate [$C_2H_5ONO_2(g)$], 25°.

Figure 47 Absorption spectra of selected organic molecules.

in Figures 40 and 41, respectively. The detection of minor constituents will be achieved by performing both zenith and horizon spectral scans ($\lambda\lambda$ 2000-3000Å) throughout twilight observation periods. It can be seen from Figure 37 that a significantly enhanced cm^2 column count is involved along the path ACD. On this basis, the presence of minor constituents along this path would sensitively affect the observed zenith and horizon radiances as a function of both solar depression angle and wavelength. The application of appropriate analytic techniques should result in the extraction of the absorption characteristics of the lower atmosphere and, under certain conditions, specific constituents may be identifiable. Finally, if the major absorption contribution over a given spectral interval can be ascribed to a specific constituent (i.e. NO, CO, OH, CN, etc.), that it might be possible to obtain the scale height or number density-altitude profile for that species. In any event, it is evident that the highly sensitive absorption experiment described above can serve to establish new identifications, upper limit content values and distributions of trace constituents resident in the lower Martian atmosphere.

There appears to be little question regarding the occasional existence of dust and/or haze layers in the lower Martian atmosphere (Ref. 74) Physical, photographic and polarometric measurements have indicated that several cloud forms exist including white clouds, blue clouds, "yellow veils", and "violet hazes". The white clouds probably involve a particle size range between 1 to 60 microns and are believed to consist of either ice or solid CO_2. It is believed that their formation is favored in low temperature regions since they have often been observed at the sunrise and sunset limbs of the planet. The blue clouds, characterized probably by a particle size range between 0.1 to 1 micron have been compared by some to terrestrial noctilucent clouds, while others feel they represent an accumulation of micrometeorites suspended in the lower Martian atmosphere. The relatively rarely observed low-level yellow clouds probably consist of white desert dust blown about by Martian surface winds. In summary, it appears that not only is the presence of dust in the Martian atmosphere confirmed, but that the particle diameters appear to range from 0.1 to 60 microns.

The general experimental configuration and the procedures applied herein should closely resemble those described in the previous section concerning detection of trace molecular constituents by absorption differentiation over the spectral region $\lambda\lambda$ 2000-8000Å. However, the conduct of the observations should not be confined to twilight since it certainly appears feasible to search for particulate scattering from dust layers under full solar illuminated daytime conditions as well as during times of Phobos illumination on the night side of the planet.

For the ranges of wavelengths and particle diameters involved, it appears that both Rayleigh and Mie scattering contribute to the observed signals, so that performance of the spectral scanning procedure over the specified geometry should result in confirmation of the presence or absence of dust or haze layers in the lower Martian atmosphere. Additionally,

application of appropriate analytic procedures to representative spectral scans under the variety of conditions encountered during the experiment may produce data relevant to the size distribution, nature, and other physical characteristics of the particulate matter. Twilight observations could be employed for example, to locate the tops of layers. While this latter information is of great interest intrinsically, it could also be applied to the analysis of the other proposed twilight measurement experiments discussed previously.

With respect to nighttime measurements, the white clouds (size distribution from 1 to 60 microns) appear to form in the vicinity of the planetary sunrise and sunset limbs, so that such clouds may exist throughout the entire dark side of the planet owing to the relatively low ambient temperature conditions. This possibility could be verified simply by observing the presence of Mie scattering (far more efficient than Rayleigh scattering) from the particles illuminated by Phobos during its orbit into and around the dark side of the planet. For this particular case, however, preliminary calculations indicate that the relatively low signal intensities involved would probably require that the spectral resolution of the instrument be increased to about 100Å.

Finally, the employment of a polarization disc should be considered in order to acquire pertinent information to further characterize the size, distribution, and physical nature of the observed particles. However, it should be noted that employment of such a polarization disc generally involves signal intensity losses as well as imposing a short wavelength limitation on the observations.

The discussions presented in the previous sections have identified the general operational requirements and constraints of the proposed instrumentation system. Among the specific requirements are included (a) spectral scanning capability to cover both the ultraviolet and visible regions from $\lambda\lambda$ 2000-8000Å; (b) a spectral resolution of approximately 1Å would be desirable; (c) a highly ruggedized instrument having minimum moving parts due to the nature of the mission; (d) sensitivity such that brightness values of between 1 to 10 R/Å can be observed over the ultraviolet spectral region; and finally (e) employment of a double-pass configuration in order to minimize significant instrumental scattering problems which may be encountered in the adopted experimental mode.

In this regard, under Contract NAS5-9472 the GCA Technology Division designed a double-pass UV scanning spectrometer for operation in a satellite environment for the purpose of measuring the content and distribution of ozone in the earth atmosphere. The salient features of this latter instrument shown schematically in Figure 48 can be applied directly to the proposed experimental requirements enumerated above. The general features and pertinent operational aspects of the instrument are described elsewhere (Ref. 50).

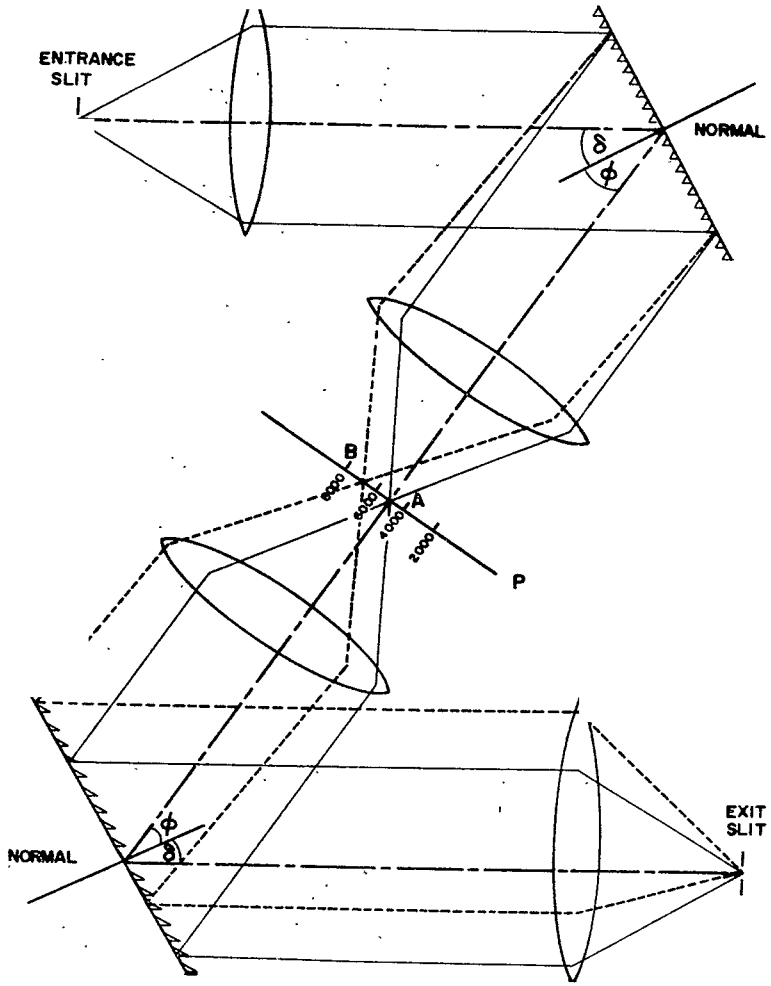

Figure 48. Schematic diagram of proposed instrument.

Order of magnitude calculations indicate that the employment of a 5 x 5 cm grating with 2400 lines/mm and a 50 cm focal length would result in the achievement of a 1Å resolution with a slit width of about 25 microns (if the grating is set for an angle of incidence of 45 degrees as shown in the figure). These calculations also indicate that the resultant photon flux at the exit slit will be about 100 photons/second for an emission rate of ten R/Å. Using these parameters, further analysis indicates that the entire spectral interval from 2000-8000Å would be spread over a length of about 15 cm across the focal plane as shown in Figure 48.

It should be noted that the optical components shown in Figure 48 are schematically indicated by lenses; however, in practice mirrors would be involved. There is no requirement for the optical components to vary their positions during scanning operations so that the fabrication of a ruggedized version of this design should constitute a relatively straightforward task.

Much of the material generated under this study has been utilized in the preparation of a suggested experiment for the forthcoming Mars Lander program.

"The Rocket Measurement of the 62 Micron O I Emission in the Upper Atmosphere." The elucidation of the various processes responsible for the thermal structure of the upper atmosphere of the so-called thermosphere (Ref. 75) is of importance for the understanding of the thermal structure of the planetary upper atmosphere. The thermal structure of the lower atmosphere is mainly controlled by the local absorption and emission of radiation, and the transport of thermal energy by conduction is relatively unimportant. However, Spitzer (Ref. 76) pointed out that, in the upper regions of the atmosphere, the role of absorption and emission is very much decreased due to the low total particle density, and the conduction of thermal energy becomes important. This is due to the fact that the thermal conductivity of a gas is independent of the gas density.

Bates (Refs. 77,78) has considered in detail the heat input by the absorption of solar ultraviolet radiation and its loss by the 62 micron emission by atomic oxygen. The thermal balance of the atmosphere is given by

$$k \times \frac{d^2T}{dz^2} = -G + R, \qquad (29)$$

where k is the thermal conductivity,
R is the loss of heat by the radiation of 62 micron emission, and
G is the local heating caused by solar uv radiation and is given by

$$G(z) = \epsilon I(\infty)\sigma\, n(Z)\, e^{-n(Z)\sigma H} \qquad (30)$$

where $I(\infty)$ is the solar flux at the top of the atmosphere,

σ is the absorption cross section,

$n(Z)$ is the particle concentration of the absorbing constituents,

H is the scale height, and

ϵ is the heating efficiency factor or the fraction of the absorbed uv energy which is used in local heating.

The information regarding solar VUV radiation flux and that of absorption cross section is fairly satisfactory. However, the heating efficiency factor is poorly known. McElroy, et al (Ref. 79) have discussed the various processes responsible for the conversion of the absorbed VUV radiation into local thermal energy. Their discussion indicates that, from the consideration of the complexity of the processes, the theoretical determination of the heating efficiency factor is difficult. Hunt, et al (Ref. 80) have concluded that the estimated heating efficiency factor varies between 6 percent and 50 percent. It is proposed here that the simultaneous observation of the transmission of solar VUV radiation and that of 62μ emission by rockets can yield reliable information regarding the heating efficiency factor.

If we substitute Equation (30) in Equation (29) and integrate, we have

$$k \times \frac{dT}{dZ}\Big|_{Z} = I(\infty)\epsilon \left[1 - \exp\left(-n(Z)\sigma H\right)\right] - \int_{Z}^{\infty} R(Z)\, dZ. \qquad (31)$$

At thermopause, the temperature gradient is zero and; therefore, the thermal efficiency factor is given by

$$\epsilon = \frac{\int_{Z}^{\infty} R(Z)dZ}{I(\infty)\left[1 - \exp(-n(Z)\sigma H)\right]}. \qquad (32)$$

Therefore, it can be concluded that the measurement of 62μ flux can give valuable information regarding the thermal structure of the atmosphere.

The O I emission resulting from the transitions between the fine structure levels of the ground ^3P state of the atomic oxygen are shown in Figure 49.

$$k\, n(M) \gg \frac{g_1}{g_2} A_{1-2}$$

$$\gg 5.34 \times 10^{-5}$$

$$\text{or } n(M) \gg \frac{5.34 \times 10^{-5}}{k} \qquad (36)$$

TABLE 5

State	eV	A sec^{-1}	g	exp $(-\epsilon_n/kT)$ 100°K	500°K	1000°K	1500°K	2000°K	3000
$^3P_0$	0.028	1.7×10^{-5}	1	3.88×10^{-2}	5.22×10^{-1}	7.23×10^{-1}	8.02×10^{-1}	8.52×10^{-1}	8.95x
$^3P_1$	0.020	8.9×10^{-5}	3	9.83×10^{-2}	6.31×10^{-1}	7.95×10^{-1}	8.56×10^{-1}	8.90×10^{-1}	9.23x
$^3P_2$	0.000	---	5	---	---	---	---	---	--
		$\Sigma g_n \exp(-\epsilon_n/kT)$		5.33	7.41	8.11	8.37	8.52	8.6

The information regarding collisional energy transfer between the fine structure levels of the ground state atomic oxygen by process (33) is not available. However, the information regarding the rate constant of similar processes for Hg and alkali atoms (Mitchel and Zemansky) (Ref. 81) is known, and it varies between 5×10^{-10} cm^3/sec for Na and 1.5×10^{-12} for Hg. Assuming $k \sim 10^{-12}$ cm^3/sec, we find that the above condition is satisfied for

$$n(M) \gg 5.3 \times 10^7. \qquad (37)$$

Therefore, it can be concluded that the distribution of atomic oxygen between the fine structure levels of its ground state will be in thermodynamic equilibrium with the ambient up to altitudes of about 250 km in earth's atmosphere; of course this may be correspondingly higher if the rate constant is larger than the value used above.

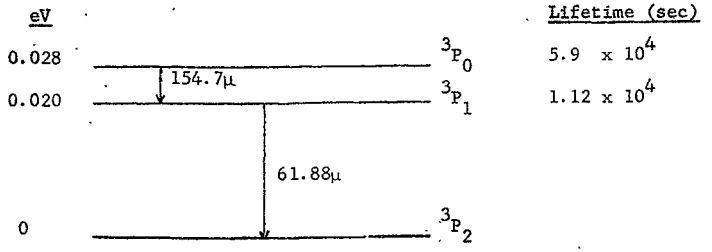

Figure 49

The $^3P_0$ and $^3P_1$ levels of O I lie only about 0.028eV and 0.020eV above the lowest $^3P_2$ level, so that the excitation potentials involved are of the same order as the energy of the thermal motion. The transition probabilities of the two transitions $^3P_0 \rightarrow {}^3P_1$ is about 1.7×10^{-5} sec^{-1}, and that of $^3P_1 \rightarrow {}^3P_2$ is about 8.9×10^{-5} sec^{-1}. If the collisional excitation of $^3P_0$ and $^3P_1$ is made sufficiently rapid by the following process

$$O(^3P_2) + M \rightarrow O\ (^3P_1 \text{ or } {}^3P_0) + M, \qquad (33)$$

then the distribution of oxygen atoms in these levels will be the characteristic of the ambient temperature. Since the lifetime of $^3P_1$ level is shorter than that of $^3P_0$ level, we shall mainly consider the 62μ radiation.

The required condition for the Boltzmann distribution of O atoms between $^3P_1$ and $^3P_2$, which is characteristic of the ambient temperature, is

$$k \times n\ [O,\ ^3P_2]\ n\ [M]\ \exp\ (-\epsilon_1/kT) \gg A_{1-2}\ n\ [O,\ ^3P_1] \qquad (34)$$

and then

$$n\ [O,\ ^3P_1] = \frac{g_1}{g_2} \exp\ (-\epsilon_1/kT)\ n\ [O, {}^3P_2]\ , \qquad (35)$$

where g_1 and g_2 are the statistical weights of the two $^3P_1$ and $^3P_2$ states, respectively. T is the ambient temperature and ϵ_1 is the excitation energy of the $^3P_1$ level, which is equal to 0.02 eV. The relevant information is collected in Table 5. Using relations (34) and (35), the condition for the thermal equilibrium between $^3P_1$ and $^3P_2$ can be written as

The loss of radiation in a planetary atmosphere by atomic oxygen depends on its optical thickness above the reference altitude, which in turn depends on its absorption cross section. The absorption cross section at the line center is given by

$$\alpha_{2-1} = \frac{1}{4\lambda} \left(\frac{\ell n\ 2}{\lambda}\right)^{1/2} \frac{g_1}{g_2} \frac{\lambda^2 A_{1 \to 2}}{\Delta\nu_D} \tag{38}$$

where λ is the wavelength of the line center and

$$\Delta\nu_D = \left[\frac{2kT\ \ell n 2}{mc^2}\right]^{1/2} \times \frac{1}{\lambda}$$

is the Doppler half-width of the line. Therefore,

$$\alpha_{2-1} = \frac{1}{4\lambda}\left[\frac{mc^2}{2\lambda kT}\right]^{1/2} \frac{g_1}{g_2} \times \lambda^3 A_{1\to 2}$$

$$= 9.4 \times 10^{-17} \times T^{-1/2}\ cm^2; \tag{39}$$

and the optical thickness of the atmosphere is given by

$$\tau = \int_Z^\infty \alpha_{2-1} \left[1 - \exp\left(-\epsilon_1/kT\right)\right]\ n\ (0, {}^3P_2)\ dZ \tag{40}$$

$$\tau = 9.4 \times 10^{-17} \int_Z^\infty \frac{1}{\sqrt{T}} \left[1 - \exp\left(-\epsilon_1/kT\right)\right] n\ (0,\ {}^3P_2)\ dZ$$

and for an isothermal atmosphere

$$\tau = 9.4 \times 10^{-17} \times \frac{1}{\sqrt{T}} \left[1 - \exp\left(-\epsilon_1/kT\right)\right] \times \frac{g_2}{\Sigma g_n \exp\left(-t_n/kT\right)} \int_Z^\infty n(0)dZ$$

$$\tau = K \times \int_Z^\infty n(0)\ dZ \tag{41}$$

The calculated values of K for different temperatures are given below:

TABLE 6

Temperature °K	100	500	1000	1500	2000
K	8.82×10^{-18}	9.75×10^{-19}	3.76×10^{-19}	2.08×10^{-19}	1.36×10

Temperature °K	3000
K	7.63×10^{-20}

It can be concluded that, for the same optical thickness at the line center, larger numbers of atomic oxygen per cm^2 column are required at higher temperatures. This is understandable because at higher temperatures the absorption cross section at the line center decreases and also the concentration of $O\ ^3P_2$ atoms. The rate of emission of radiation after neglecting the effects due to large optical thickness is given by

$$R(0) = \epsilon_1 A_{1\to 2} n(0, {}^3P_1) \times 1.6 \times 10^{-12} \text{ erg/cm}^3 \cdot \text{sec}$$

$$= \epsilon_1 A_{1\to 2} n(0)\eta \times 1.6 \times 10^{-12} \text{ erg/cm}^3 \cdot \text{sec}, \qquad (42)$$

where η is the fraction of total atomic oxygen concentration which are in the $^3P_1$ state.

$$\eta = \frac{g_1 \exp(-\epsilon_1/kT)}{g_0 + g_1 \exp(-\epsilon_1/kT) + g_2 \exp(-\epsilon_2/kT)} \qquad (43)$$

Hence, the net emission rate is given by

$$R(0) = R_T\, n(0) \text{ erg/cm}^3 \cdot \text{sec}, \qquad (44)$$

where $R_T = \epsilon_1 \times A_{1\to 2} \times \eta \times 1.6 \times 10^{-12}$ (45)

which depends on the temperature. Substituting from Table 5, we have calculated R_T and its values are given below:

TABLE 7

Temperature ^{o}K	R_T (Erg/atom · sec)
100	1.58×10^{-19}
500	7.27×10^{-19}
1000	8.38×10^{-19}
1500	8.75×10^{-19}
2000	8.92×10^{-19}
3000	9.09×10^{-19}

The resultant flux of 62μ radiation in the earth's atmosphere can now be calculated for a given standard model atmosphere. The relevant parameters for CIRA (1965) model are shown in Table 8. Using Equation (41) and the values of K given in Table 6, the optical thickness of the atmosphere above different altitudes are calculated and shown in the last column of Table 8. It can be concluded from Table 8 that the optical thickness for 62μ radiation is much less than 1 at altitudes above 150 km. It should also be noted that the required condition (Equation 37) for the Maxwell-Boltzmann distribution is satisfied at least up to 300 km and may be to higher altitudes. Therefore, the flux of 62μ emission radiation in a region between 150 km and 300 km can be calculated from Equations (44) and (45) and using the values of R_T given in Table 7. The calculated rate of emission per unit volume is given in Table 9. The rate of emission per cm^2 column seen by a detector pointing upward in a rocket is given in the last column of Table 9 and is obtained by multiplying the volume emission rate by the atmospheric scale height. It should, however, be noted that the emission flux seen by a rocket borne detector pointed in the horizontal direction is about 30 times that seen in the vertical direction. It can be concluded from Table 6 that, between 100 to 300 km altitude, the observed flux varies between about 10^{-8} to 2.5×10^{-10} watt/cm^2 for a detector pointed to the upward direction and between 3×10^{-7} to 7×10^{-9} watt/cm^2 for a detector pointed to the horizontal direction.

It is now appropriate to consider the feasibility of detecting the 62μ radiation by means of a rocket platform experiment.

The detectability of the radiation by O.I at 62μ depends on celestial background at the top of the atmosphere due to stellar radiation and that originating in the solar system. The infrared background at the top of the earth's atmosphere, due to the latter source, is due to the reflection of solar radiation by planets and satellites and also due to the thermal emissions. A major component is also due to the infrared radiatior

TABLE 8

Altitude (km)	Temperature (^{o}K)	Scale Height (km)	Total Particle Density cm^{-3}	Atomic Oxygen Density cm^{-3}	Optical Thickness
100	208	6.44	1.07×10^{13}	5.00×10^{11}	3
150	750	23.05	5.23×10^{10}	1.41×10^{10}	3×10^{-2}
200	1198	37.37	6.88×10^{9}	3.23×10^{9}	4×10^{-3}
250	1524	48.27	1.86×10^{9}	1.18×10^{9}	1×10^{-3}
300	1755	46.40	6.75×10^{8}	5.12×10^{8}	4×10^{-4}

TABLE 9

Altitude	Emission Rate Per Unit Volume Erg/cm^3 sec	Emission Flux Erg/cm^2 sec
100	1.55×10^{-7}	9.98×10^{-2}
150	1.10×10^{-8}	2.53×10^{-2}
200	2.75×10^{-9}	1.03×10^{-2}
250	1.03×10^{-9}	4.97×10^{-3}
300	4.52×10^{-10}	2.55×10^{-3}

from zodiacal light and gegenschein. The information regarding the infrared background at the top of the earth's atmosphere is not available in the 62μ region. However, the total infrared irradiance in the 0.8 to 3μ region is as follows (Handbook of Geophysics and Space Environments, 1965)

Source	Irradiance W/cm^2
Stellar	$\sim 10^{-10}$
Sun	1.19×10^{-1}
Moon (Full)	2.6×10^{-7}
Mercury (Elongation)	1.2×10^{-11}
Venus (Elongation)	1.8×10^{-10}
Mars (Quadrature)	3.7×10^{-12}
Jupiter (Quadrature)	8.2×10^{-12}
Saturn (Quadrature)	8.4×10^{-13}
Uranus (Apposition)	1×10^{-15}
Neptune (Apposition)	8×10^{-15}
Zodiacal and Gegenschein (between Elongation of 50° to 18°)	$\sim 10^{-10}$

It can be concluded from the above table that the infrared irradiance between 0.8 to 3μ at the top of the earth's atmosphere and in the absence of solar or lunar illumination is about 10^{-10} W/cm^2. If this radiation is assumed to be characteristic of effective black body temperature of a few thousand degrees (the effective black body temperature of the sun and other stellar sources) then at longer wavelengths, the irradiance should decrease as λ^{-4}. Therefore, the extrapolated irradiance at the top of the earth's atmosphere is about 10^{-15} W/cm^2 around 62μ O I emission is several orders of magnitude above the natural background due to extra terrestrial sources.

We shall now consider the detectability of the 62μ O I emission by an appropriate rocket-borne detector for this spectral region. A suitable detector in this region is the low-temperature gallium-doped germanium bolometer system which operates a liquid helium temperature (Ref. 82). The general characteristics of this detector have been discussed elsewhere (Ref. 83) and are not repeated here. Specifically, the total flux F_D received by the detector is approximately given by

$$D = \frac{\Omega D}{4\lambda} \int_{Z}^{\infty} n(O)\ R_T\ dZ$$

$$= \frac{\Omega D}{4\lambda} F = KF,$$

where: D = element area

F = emission flux (in W/cm^2)

Ω = effective solid angle of the instrument

K = instrument constant

The N.E.P. of the above types of detectors is about 10^{-12} watts (Ref. 82), and it can be concluded that the atmospheric emission at 62μ of O I can be successfully measured by available detectors since the emitted flux is between 6×10^{-17} W/cm^2 to 10^{-10} W/cm^2.

"The Deposition of Meteoric Debris Constituents into the Upper Atmospheres of Earth, Venus and Mars." Notwithstanding the lack of quantitative data on the influx rate and mass distribution of meteoric debris sufficient data are available to make it evident that the major contribution to the accretion of this debris by earth is due to particles with masses less than about 10^{-7} grams (which corresponds to radii less than 50μ). (Refs. 84-86). Prior studies (Refs. 87-95) to determine flux from rocket collections have assumed that no mass loss by ablation occurs when the radius of the particles is less than 50μ. A series of studies on the interaction of micrometeoroids with the earth atmosphere (Refs. 96-98) have made it evident that the above assumption is not true and that particles with radii less than 50μ do indeed ablate so as to result in a deposition of micrometeoroid constituents into the upper atmosphere of earth. Specifically, Whipple (Ref. 97) demonstrated that spherical particles of density 3 grams/cm^3 entering vertically with velocities of 12, 15, 30, and 70 km/sec ablate for radii less than 39, 19, 3, and 0.3μ respectively. Clearly, the deposition of this debris into the upper atmosphere of planets can have important aeronomic effects as well as contributing to ionospheric phenomena, noctilucent clouds, haze layers, airglow phenomena, etc. It is the purpose of this study to obtain estimates of the mass deposition rates of ablated atomic matter within the atmospheres of earth, Venus, and Mars. In accordance with the above discussion, this study is limited to meteoric debris particles with masses less than 10^{-7} grams, i.e. radii less than 50μ.

Allen, et al. (Ref. 99) have shown that shielding and fragmentation do not obtain for all r-values less than 50μ; whereas Levin (Ref. 100)

has shown that heat storage effects can be neglected for such particles so long as the entering velocity is less than approximately 60 km/sec. Accordingly, for this preliminary study it was felt that the classical theory of meteor ablation (Refs. 96-98, 101-105) could apply in order to obtain the desired estimates. The appropriate techniques are first developed and applied to the atmosphere of earth. These findings are then extrapolated and applied to appropriate model atmospheres for Venus and Mars in order to obtain corresponding ablation-mass profiles.

According to the classical theory for meteoric ablation (Ref. 106) once the ablation temperature has been achieved the instantaneous mass, m, of the ablated meteoroid at altitude, z, is

$$m = m_\infty \left(1 - \frac{\gamma F v^2}{8\xi\rho r_\infty \cos\chi} \int_\infty^z \rho_a dz\right)^3 \qquad (46)$$

where: m_∞ = the initial mass

γ = the drag coefficient (a value of 1.1 is assumed here after Reference 107)

F = the shape factor, [defined as $\sigma/\pi r^2$ where σ is the cross sectional area of the meteoroid and r is the radius of a spherical meteoroid (F = 1 for a sphere)]

v = the velocity

ξ = the energy of ablation (a value of 1.1×10^{11} cm^2/sec^2 is assumed here after Reference 107)

ρ = the meteoroid density

r_∞ = the initial radius (of a spherical meteoroid)

χ = the zenith angle of the radiant

ρ_a = the atmospheric density

For ready solution of Equation (46) the atmosphere is considered to be composed of a series of concentric layers wherein each zone is sufficiently small compared to the scale height, H, so that for computation purposes an average scale height $\bar{H}$, obtains. Under these conditions, Equation (46) can be approximated by

$$m = m_o \left[1 - \frac{\gamma F v^2 \bar{H}}{8\xi\rho r_o \cos\chi} (\rho_a - \rho_o)\right]^3 \qquad (47)$$

which obtains for each individual layer.

The corresponding ablation rate, n, or atoms ablated per unit time for an individual particle is then given by:

$$n = -\frac{1}{\mu}\cdot\frac{dm}{dt} = \frac{3n_o'\rho_a\gamma F v^3}{8\xi\rho r_o}\left[1 - \frac{\gamma F v^2 \bar{H}}{8\xi\rho r_o \cos\chi}\,(\rho_a - \rho_o)\right]^3 \quad (48)$$

atoms/sec

or

$$n = \frac{3n_o'\rho_a\gamma F v^2}{8\xi\rho r_o \cos\chi}\left[1 - \frac{\gamma F v^2 \bar{H}}{8\xi\rho r_o \cos\chi}\,(\rho_a - \rho_o)\right]^2 \quad (49)$$

atoms deposited/unit vertical path

The the above equations the subscripts $_o$ refer to the upper boundary of a given zone and n_o' is the number of unablated atoms remaining in the particle at the upper boundary of a given zone and μ is the molecular mass (grams/molecule) of the meteoric material.

The present study is concerned with the chemical interaction of the atomic debris with atmospheric constituents so that the role of the surviving particles is not considered further. However, it is clear that these studies can be applied to the latter problem for the purposes of relating incoming flux values with empirical data obtained by satellites, rockets, balloons and surface measurements. In order to apply these equations to the present problem, a number of meteoric physical parameters must be established. For this purpose the following comments apply.

For the present purpose the particle influx-particle mass relationship (Ref. 84) shown in Figure 50 is selected and considered to represent an upper limit value for the particle influx rate. The indicated distribution has not been firmly established so that the present results should be viewed with appropriate caution. In any case, this distribution makes it evident that the major contribution to mass deposition in the earth atmosphere is indeed due to particles with masses less than approximately 10^7 and 10^8 grams, i.e. less than 50μ. Since there is considerable disagreement in the literature on the correct particle influx-particle mass relationship, it is appropriate that the techniques illustrated in the present study be applied to other distributions so that some upper and lower limit values can be acquired.

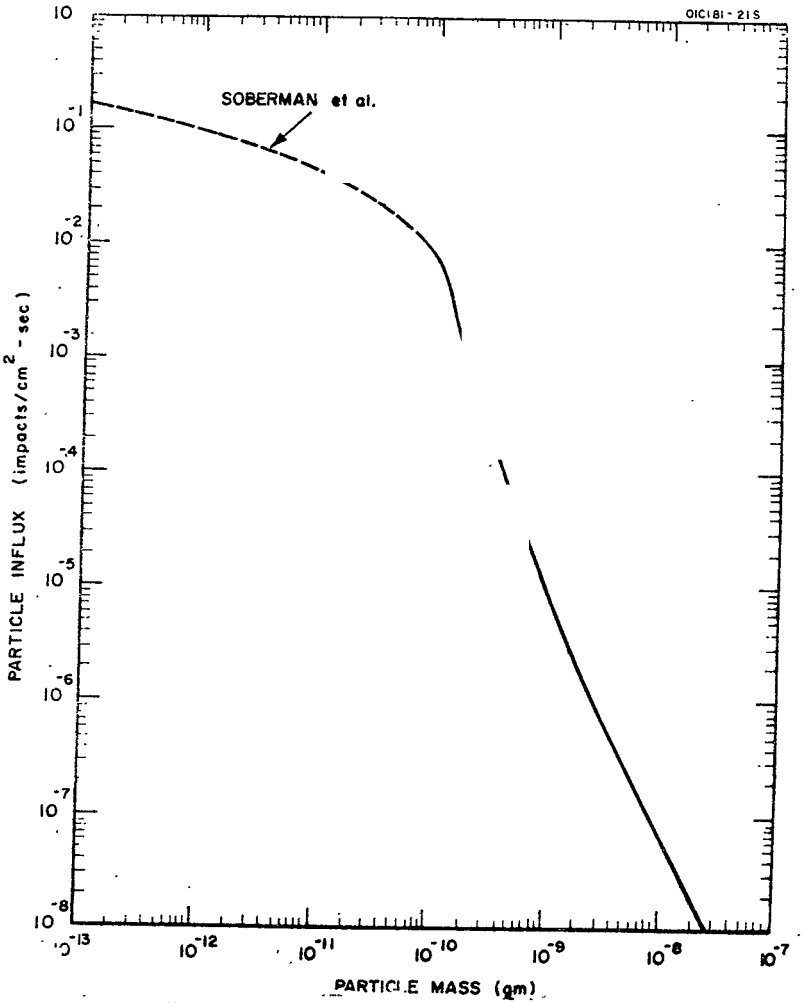

Figure 50 Adopted distribution for particle influx *vs.* particle mass. Distribution is considered to represent an upper limit.

Concerning the assumed shape of the micrometeoroid it is appropriate to assume spherical bodies since these result in a considerable simplification of the calculations involved. However, it is recognized that photographs of these particles collected during rocket investigations (Ref. 87) show that the micrometeoroids can assume a variety of shapes which appear to be rather irregular.

For the present purposes the particle density-particle radius relationship shown in Figure 51 was adopted on the basis of fitting and extrapolating a smooth curve to the several derived densities and estimates of densities appearing in the literature (Refs. 87, 107, 108). In this regard it will be later demonstrated that most of the mass deposition is due to the ablation of micrometeoroids with r-values between 0.20 and 4.0μ so that particle densities of about 2.0 to 3.5 grams/cm^3 obtain. However, here again it is appropriate to caution that this relationship has not been firmly established.

A representative value of 23 grams/molecule is taken for the atomic weight of micrometeoroid particles since this is the average value for stony meteorites (Ref. 102) which constitutes 90 percent of all incident micrometeoroids.

Perhaps the most important single parameter to establish is that of the velocity distribution of the incident micrometeoroid particles. The distribution adopted for this study leaned heavily on the data relevant to twelfth visual magnitude radar meteors established by Eshleman, et al (Ref. 109). This procedure was adopted since there are no pertinent data on the size distributions considered here and the data cited represent the faintest meteors for which velocity histograms have been established. The velocity histograms reported by Eshleman, et al (Ref. 109) included micrometeoroids of interstellar origin, i.e. velocities greater than 72 km/sec. However, since this component amounts to only between 1 and 2 percent of the total incoming flux (Ref. 110) it has been neglected in the present study. Furthermore, the published velocities were slightly redistributed so as to include velocities between 11-35 km/sec, which were absent from the published data. In any case, the velocity histogram shown in Figure 52 obtains for the present study and is considered to be a reasonable representation of the distribution involved. Corresponding velocity histograms for the planets Venus and Mars have been derived on the basis of data shown in Table 10.

TABLE 10

Meteoroid Velocity Ranges for Earth and Proximate Planets

Planet	Mean Orbital Velocity	v_{esc}(sun)	v_{esc}(planet)	$v_{minimum}$	$v_{maximum}$
Venus	35	49	10	10	85
Earth	30	42	11	11	73
Mars	24	34	5	5	58

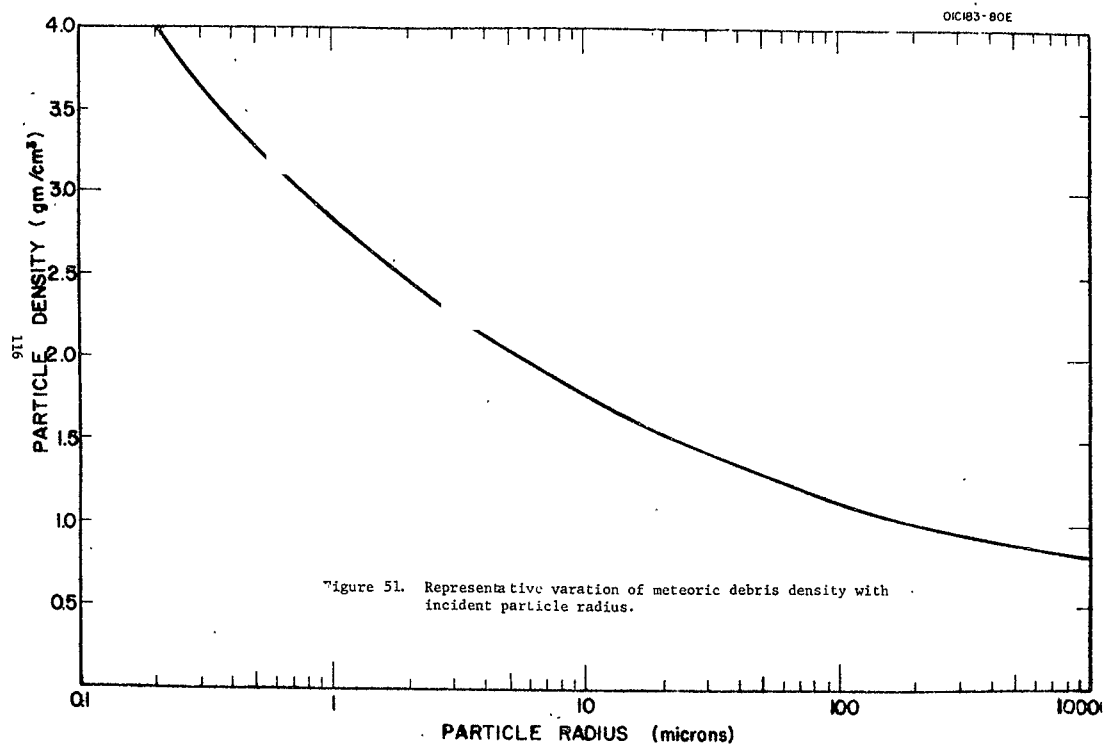

Figure 51. Representative varation of meteoric debris density with incident particle radius.

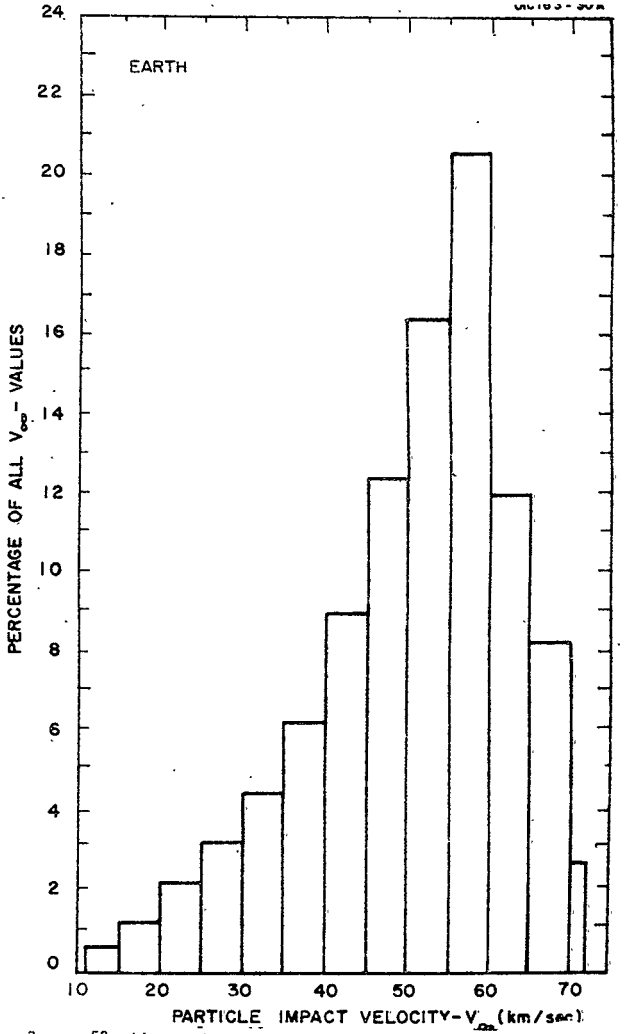

Figure 52 Adopted distribution for percentage of all incident v-values vs. particle impact velocity for planet earth.

The resultant histograms are graphically shown in Figures 53 and 54 for Venus and Mars respectively.

It has been established (Refs. 96-98,101-105) that a critical mass/surface area ratio (m/s) obtains wherein incoming micrometeoroids with m/s-values less than critical will survive passage through the atmosphere (with no ablation)owing to the fact that they can not attain melting temperature, i.e. about 1800°K for stony meteors (Ref. 98). Specifically, Whipple (Ref. 97) has shown that for a non-isothermal atmosphere

$$\frac{m}{s} = \frac{3e\gamma T_1}{(\nu+q)\cos\chi}\left(\frac{\rho_1}{8}\right)^{\nu/(\nu+q)}\left[\frac{\epsilon a(T^4-T_o^4)}{Av_\infty^3}\right]^{q/(\nu+q)} \qquad (50)$$

Where: e = natural logarithm, 2.718

T_1 = temperature at base of region for which temperature gradient is $\nu = dT/dz$

ρ_1 = atmospheric density at base of region

$q = \bar{\mu}g/R$, $\bar{\mu}$ = mean molecular weight of air, gms/mole, g = acceleration due to gravity, R = universal gas constant, 8.31×10^7 ergs/mole-deg

ϵ = emissivity

a = Stefan-Boltzman constant, 5.67×10^{-5} erg

T = instantaneous temperature of micrometeoroid

T_o = exoatmospheric temperature of micrometeoroid

For a spherical particle $\frac{m}{s} = \frac{r\rho}{3}$ (51)

From Equations (50) and (51), $r\rho$-values were calculated for the respective velocity ranges at the three planets using the parametric values in Table 11.

Using the relationship between radius and density shown in Figure 52, the data in Figure 55 were obtained to indicate the minimum threshold radii for melting as a function of initial particle velocity. Specifically,

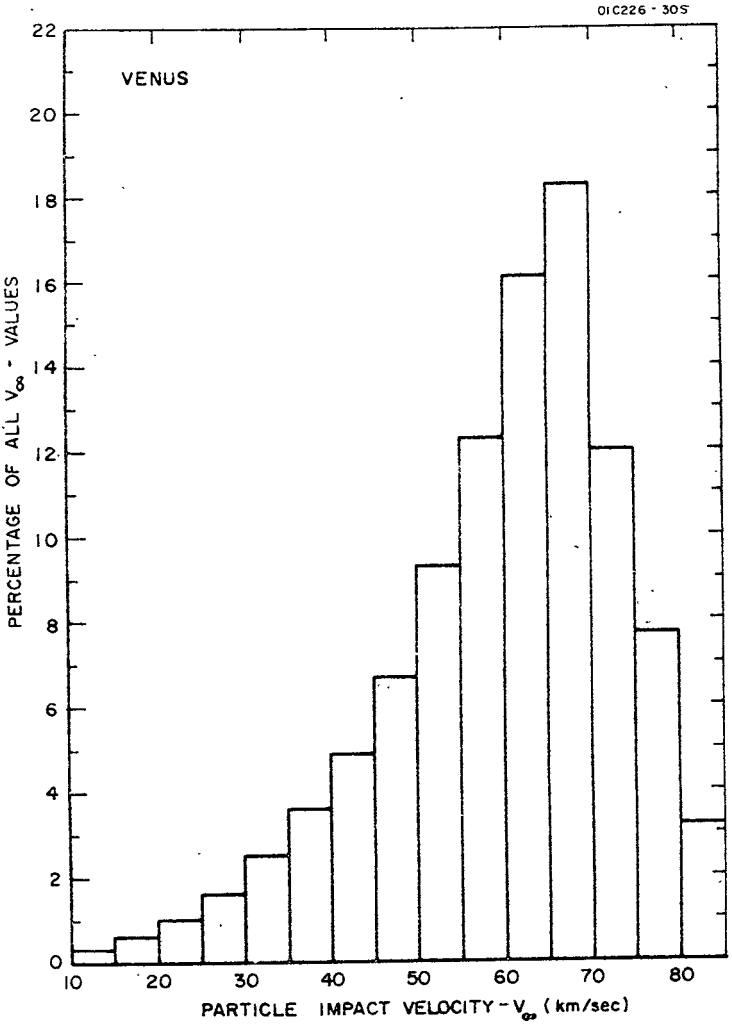

Figure 53 Adopted distribution for percentage of all incident v-values vs. particle impact velocity for planet Venus.

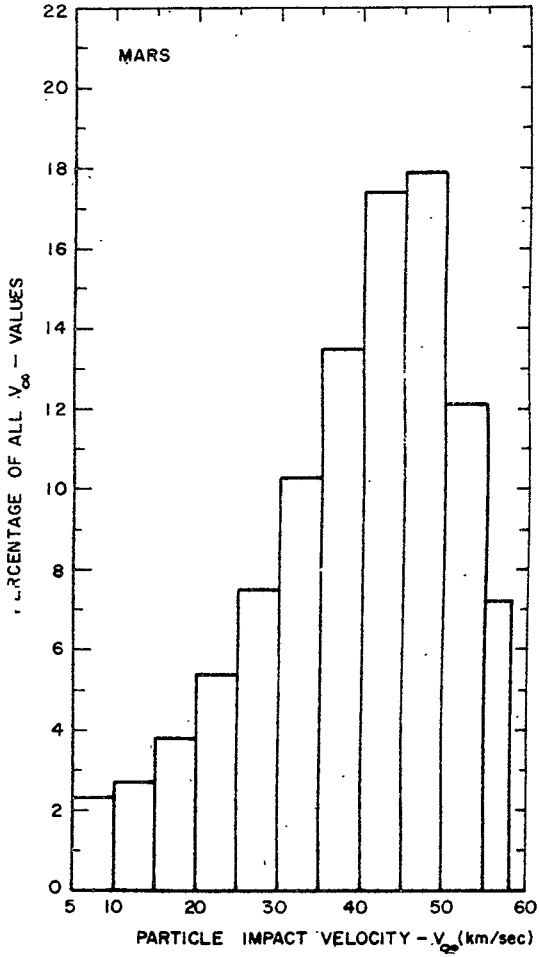

Figure 54. Adopted distribution for percentage of all incident v-values vs. particle impact velocity for planet Mars.

TABLE 11

	Earth	Venus	Mars	Reference
γ	1.1	1.1	1.1	(57)
$\cos\chi$	0.8	0.8	0.8	(61)
T_o	300^oK	300^oK	300^oK	(47)
T	1800^oK	1800^oK	1800^oK	(52)
Λ	1	1	1	(54)
$\bar{\mu}$	30	44	38.3	Model Atmosphere*
q	3.43×10^{-4} deg/cm	4.48×10^{-4} deg/cm	1.65×10^{-4} deg/cm	Model Atmosphere
ref. alt.	93km	110km	110km	Model Atmosphere
T_1	181^oK	210^oK	172^oK	Model Atmosphere
ρ_1	1.76×10^{-9} gm/cm^3	1.22×10^{-10} gm/cm^3	0.932×10^{-10} gm/cm^3	Model Atmosphere
ν	4.58×10^{-5} deg/cm	9×10^{-5} deg/cm	3.73×10^{-5} deg/cm	Model Atmosphere

*The Model Atmosphere for Venus follows McElroy (Ref. 112), and for Mars, House, et al (Ref. 113).

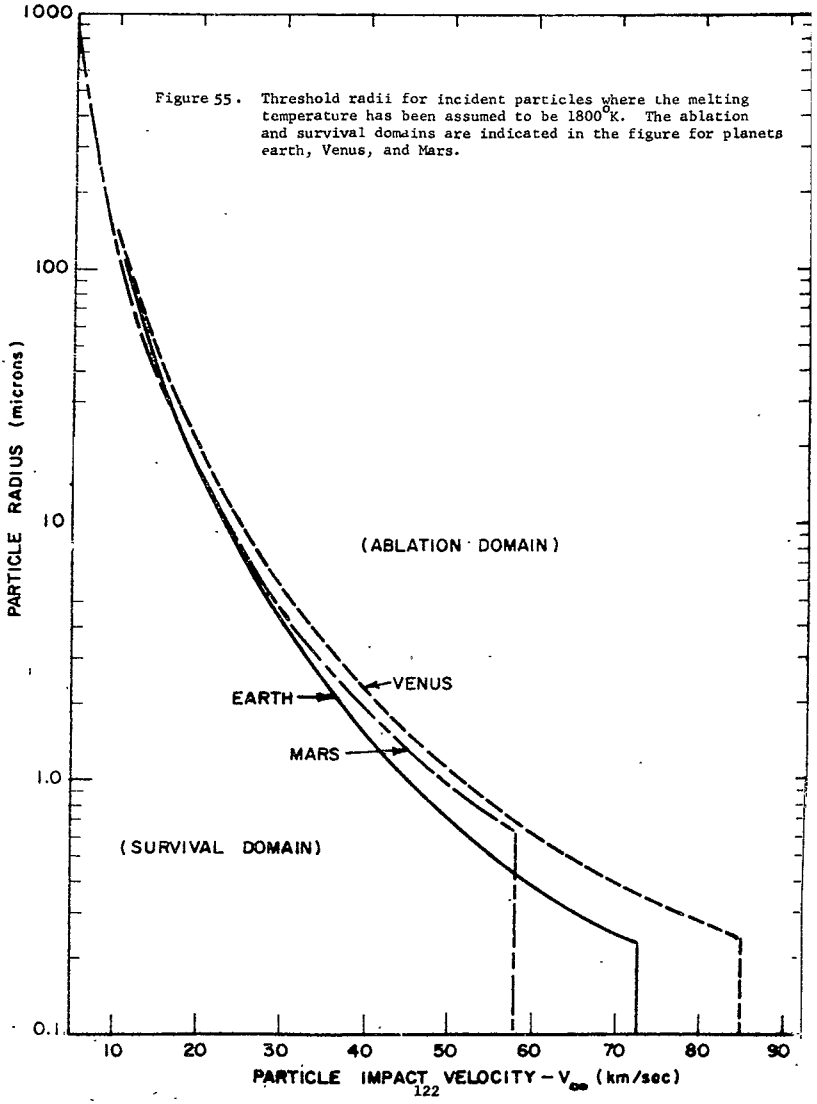

Figure 55. Threshold radii for incident particles where the melting temperature has been assumed to be 1800°K. The ablation and survival domains are indicated in the figure for planets earth, Venus, and Mars.

then, the area to the left hand side of a curve defines the radius-velocity domain of micrometeors, i.e., particles that do ablate upon entry.

It can be shown (Ref. 97) that for an initial m/s value and a given velocity, one can compute the corresponding altitude at which significant ablation commences, i.e., the temperature of melting is first achieved. The appropriate calculations have been made for an exoatmospheric micrometeoroid temperature of 300°K (Ref. 102) and a temperature of melting-ablation of 1800°K previously established for stony micrometeoroids (Ref. 98). The resultant data for the planets Venus, earth and Mars are shown in Figure 56.

For the calculations to be performed on the interaction of micrometeoroids with the atmospheres of earth, Venus and Mars the micrometeoroids mass distribution shown in Figure 50 is assumed to apply for each case. This is justified on the basis that no relevant data exist for the other planets. On the other hand, it is evident that the particle influx rate can be expected to vary for the three planets; however, in the present approach the debris deposition rate altitude profiles are normalized to the total incident flux so that the resultant values can be readily adjusted in a linear manner on the basis of specific values adopted. Once this is established, it is a straight-forward task to demonstrate that more than 99 percent of the incident mass ablated into a planetary atmosphere results from micrometeoroids whose radii are less than only 4.0μ. To demonstrate this the data in Figures 50 and 52 have been convolved to determine the percent of incident mass-incident particle radius relationships as shown in the histogram of Figure 57. At this point it is appropriate to summarize the following factors: (1) more than 99 percent of the incident mass is due to micrometeoroids with r-values less than 4.0μ, (2) for a given r-value only those micrometeoroids entering at velocities above the threshold value will significantly ablate (see Figure 55), (3) for all incoming particles with m/s-values greater than critical there is an altitude at which ablation commences which is a function of the particle impact velocity (see Figure 56).

Figures 52, 53, and 54 represent plots of the percentage of incoming v_∞-values against particle impact velocity for the planets earth, Venus and Mars respectively. It is a straight-forward task to compute the fraction of mass that will ablate for any given velocity increment in order to derive some idea of the fraction of material ablating in a given atmosphere. The relevant histograms are shown in Figures 58, 59 and 60 for the planets earth, Venus, and Mars. In these histograms the shaded portions represent the ablated fraction in a given velocity increment. Thus, the integrated shaded area in each case gives a measure of the percent of incident meteoroid mass that ablates within a given planetary atmosphere. These percentages are 86, 87 and 58 for earth, Venus and Mars, respectively. An analogous calculation has been performed for the

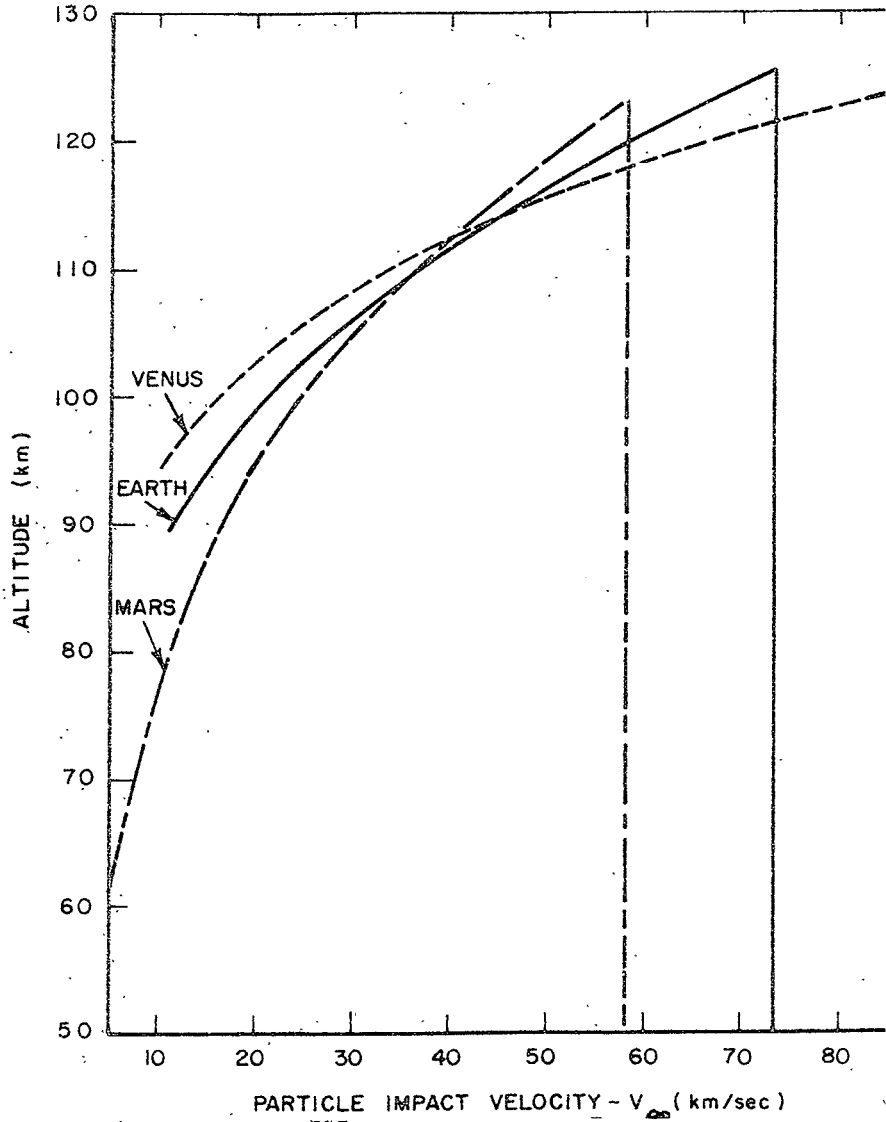

Figure 56. Threshold altitudes vs. particle impact velocities where incoming particles commence melting at a temperature of 180(

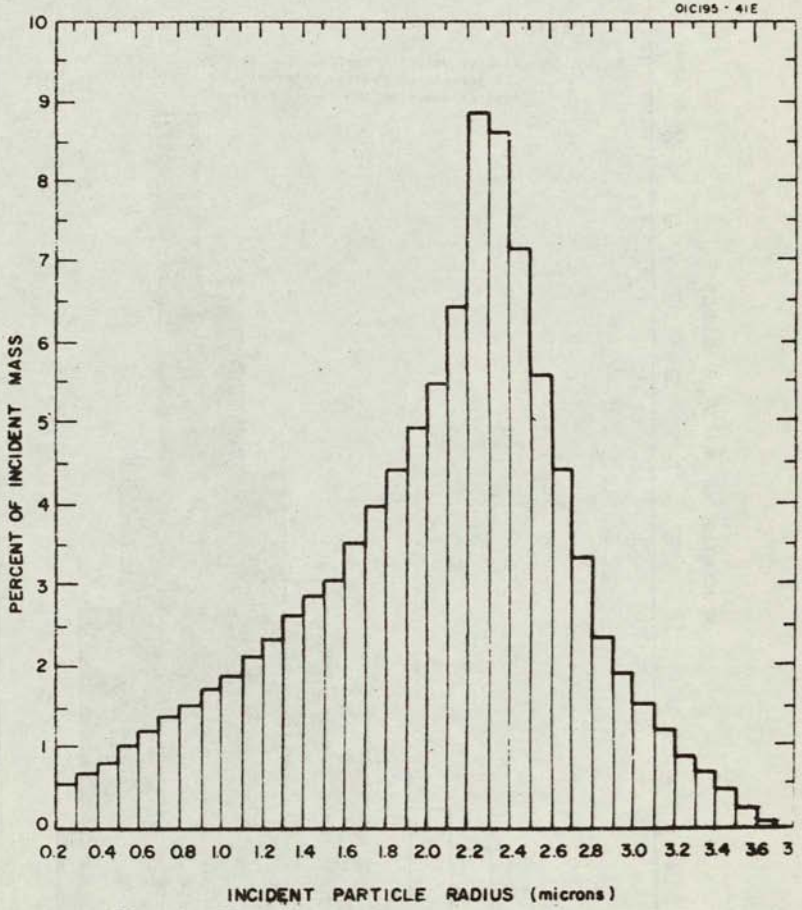

Figure 57. Plot of percent of incident mass contained within incident particle radii increments between 0.2 and 3.8 microns. This plot is derived on the basis of the distribution shown in Figure 50.

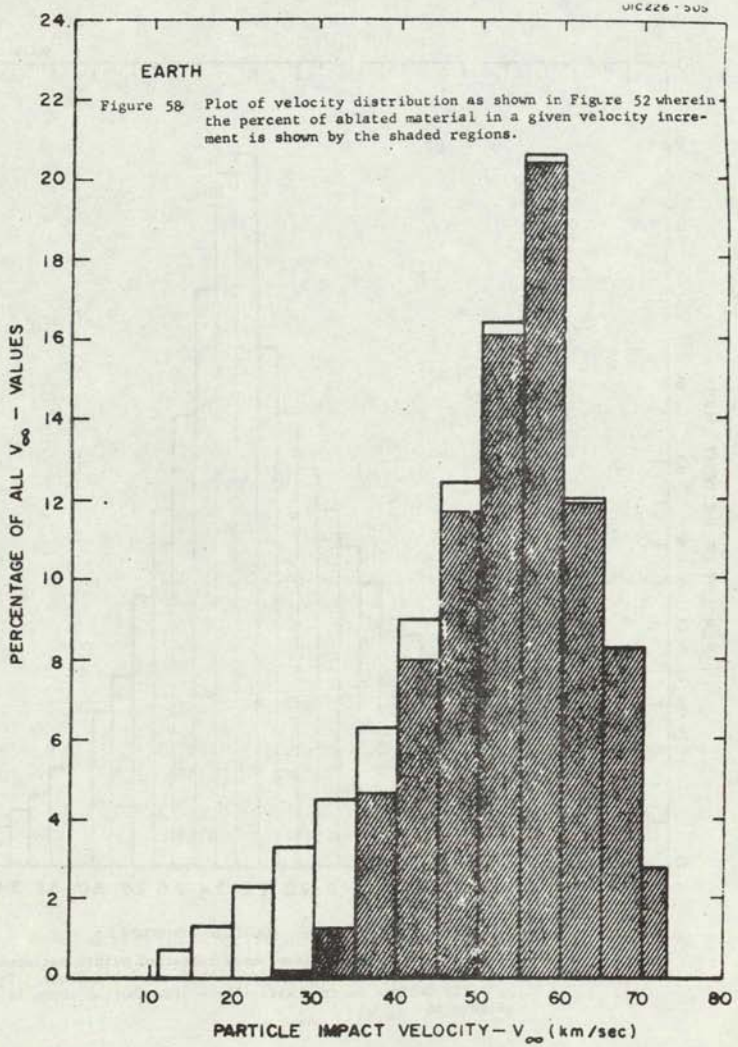

Figure 58 Plot of velocity distribution as shown in Figure 52 wherein the percent of ablated material in a given velocity increment is shown by the shaded regions.

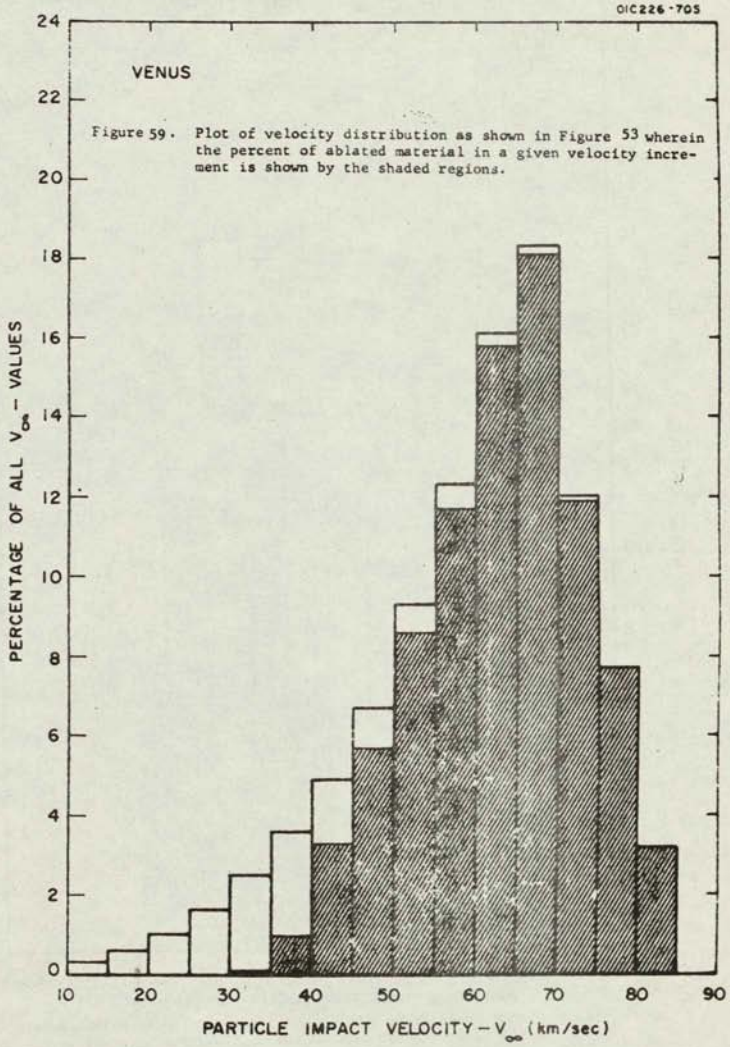

Figure 59. Plot of velocity distribution as shown in Figure 53 wherein the percent of ablated material in a given velocity increment is shown by the shaded regions.

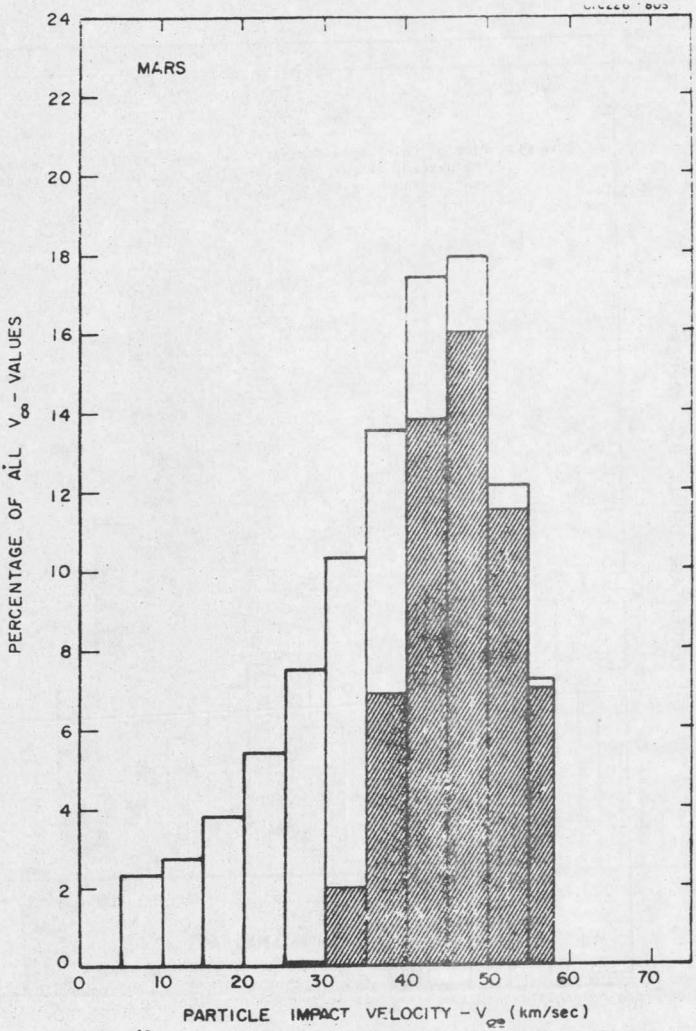

Figure 60. Plot of velocity distribution as shown in Figure 54 wherein the percent of ablated material in a given velocity increment is shown by the shaded regions

planet earth to derive a relationship between the percent of deposited mass and the incident particle radius. In this case for each individual particle radius it was assumed that the velocity distribution shown in Figure 52 obtains. The resultant histogram is shown in Figure 61 by the shaded portion which is superimposed on the data shown in Figure 57 for convenient reference. This display makes evident the fact that for micrometeoroid particles with r-values less than 0.2μ only an insignificant fraction of incident material is ablated into the upper atmosphere. This behavior of course, serves to limit the contributing radii to values between 0.2-4.0μ.

It is now appropriate to calculate the ablation rate-altitude profiles for the planets earth, Venus, and Mars. For this purpose it is convenient to rearrange Equation (49) as follows:

$$\frac{n}{N} = \frac{3F\gamma\bar{v}^{-2}\bar{H}f}{8\xi\rho\bar{r}_o\cos\chi} \quad \frac{\Delta\rho_a}{\Delta z} \left[1 - \frac{F\gamma\bar{v}^{-2}\bar{H}}{8\xi\rho\bar{r}_o\cos\chi}\left(\rho_a - \rho_o\right)\right]^2 \text{cm}^{-1} \qquad (52)$$

Where: $\bar{v}$ = the average velocity for a velocity increment

$\bar{r}_o$ = the average radius for a radius increment Δr

f = $(\Delta m/\Sigma\,\Delta m)$ $(\Delta v/\Sigma\,\Delta v)$ is the convolved fraction of (a) the ratio of the incident mass contained in the radius increment, Δr, to the total incident mass and (b) the ratio of the histogram percentage of velocities in the appropriate velocity increment -- above the threshold velocity for the corresponding value of r_o -- to all meteoroid velocities (100 percent).

For computational purpose to each velocity increment an average $\bar{v}$-value was assigned and a series of mass deposition-altitude profiles were then computed for a given radius increment, average value radius increment, $\bar{r}_o$.

The final curves of altitude vs. normalized ablation rate are shown in Figure 62 for the three planets earth, Venus and Mars. It is evident that these new results are predicated on the fact that the major deposition process is due to micrometeoroid particles with r-values less than about 4.0μ. Hence, previous investigators (Refs. 101,114) employed earlier models of meteor influx rates which more heavily weighted contributions from larger particles so that the calculated peak altitudes were considerably lower than those shown by the solid curve (earth values) in Figure 62. On the basis of these published data (Refs. 101,114) Marmo and Brown (Ref. 115) arbitrarily adopted a peak deposition altitude of 105 km for their investigation on the role of interplanetary debris in planetary atmospheres.

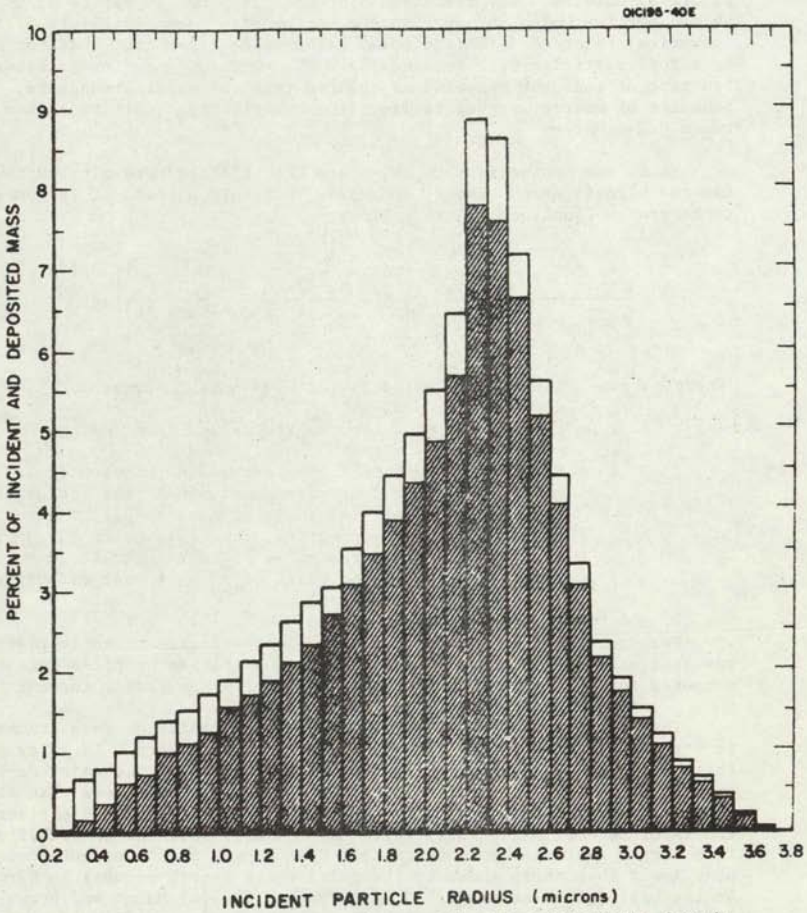

Figure 61 Plot of mass-incident particle radius distribution shown in Figure 57 wherein the percent of ablated material in a given radius increment is shown by the shaded regions.

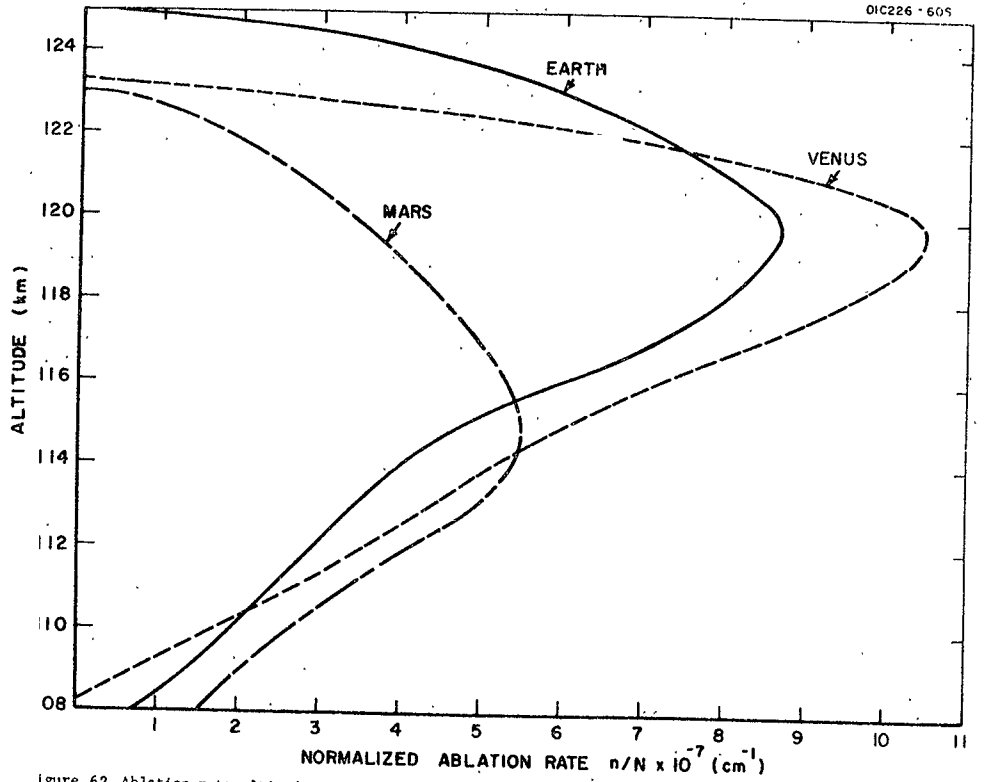

igure 62. Ablation rate-altitude profiles for the deposition of meteoric debris into the upper atmospheres of the planets earth, Venus, and Mars. The rates are normalized for extrapolation to the incident flux

Finally, these new data can find direct applicability to the mass spectrometric observations of metallic ions (presumably due to meteoric sources) recently reported by Narcissi, et al (Ref. 116), it should be recognized that the calculations performed in the present study are rather speculative and should be used with appropriate caution. However, they do serve to illustrate the general nature of the deposition of meteoric debris in planetary atmospheres so that they may be applied with some degree of confidence to some of the aeronomic problems involved in the interpretation of observational data in the upper atmosphere of earth, Venus, and Mars.

"Solar EUV Induced Fluorescent Radiation in the Atmospheres of Mars and Venus." Using photoionization production rates for excited states of CO_2^+, estimates have been obtained for fluorescent radiation from the atmospheres of Mars and Venus. The most prominent spectral feature expected is the band emission at 2882 and 2896Å, which may have an intensity as high as 8 kilorayleighs in the atmosphere of Mars and 35 kilorayleighs in the atmosphere of Venus.

Using model atmospheres based on the pure CO_2 atmospheres of McElroy (Ref. 117) photoionization production rates have been determined for the $\tilde{X}\ ^2\Pi_g$, $\tilde{A}\ ^2\Pi_u$, $\tilde{B}\ ^2\Sigma_u^+$ and $\tilde{C}\ ^2\Sigma_g^+$ states of CO_2^+. Ion production by photoelectrons has been estimated by assuming that electrons with energy between 34 and 68 eV produce one ion pair and electrons with higher energy produce one ion pair per 34 eV. The total ionization was divided among the four states of CO_2^+ using the experimental data of Bahr, et al. (Ref. 118) for wavelengths greater than 600Å. The division at shorter wavelengths and that for electron induced ionization were determined by assuming the relative values at 600Å remain constant at shorter wavelengths. The total optical and photoionization cross sections used are those given by Henry and McElroy (Ref. 119).

The accompanying drawings show the total ionization production rates and the integrated production rate above a given altitude for solar zenith angles of 0, 60, and 70 degress (See Figures 63-70 inclusive).

In the absence of any deactivation process, each ion produced in the $\tilde{A}\ ^2\Pi_u$ state will decay to the $\tilde{X}\ ^2\Pi_g$ state by band emission at wavelengths greater than 3000Å. A large fraction of the ions produced in the $\tilde{B}\ ^2\Sigma_u^+$ state will decay to the ground state by band emission at 2882 and 2986Å. Emission in these two bands will probably be the most prominent dayglow feature in the atmospheres of Mars and Venus. The wavelengths and intensities of emission from the $\tilde{C}\ ^2\Sigma_g^+$ state are uncertain.

Table 12 summarizes ion production computations. Table 13 presents total possible emission rates for each of the excited states, assuming no deactivation or cascading.

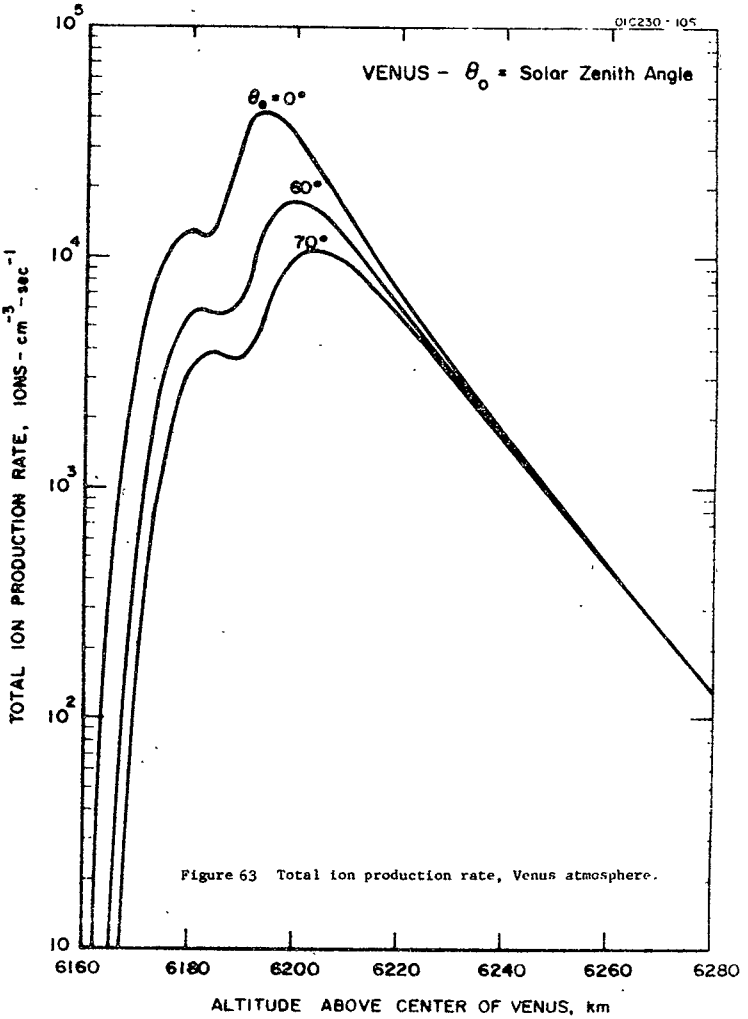

Figure 63 Total ion production rate, Venus atmosphere.

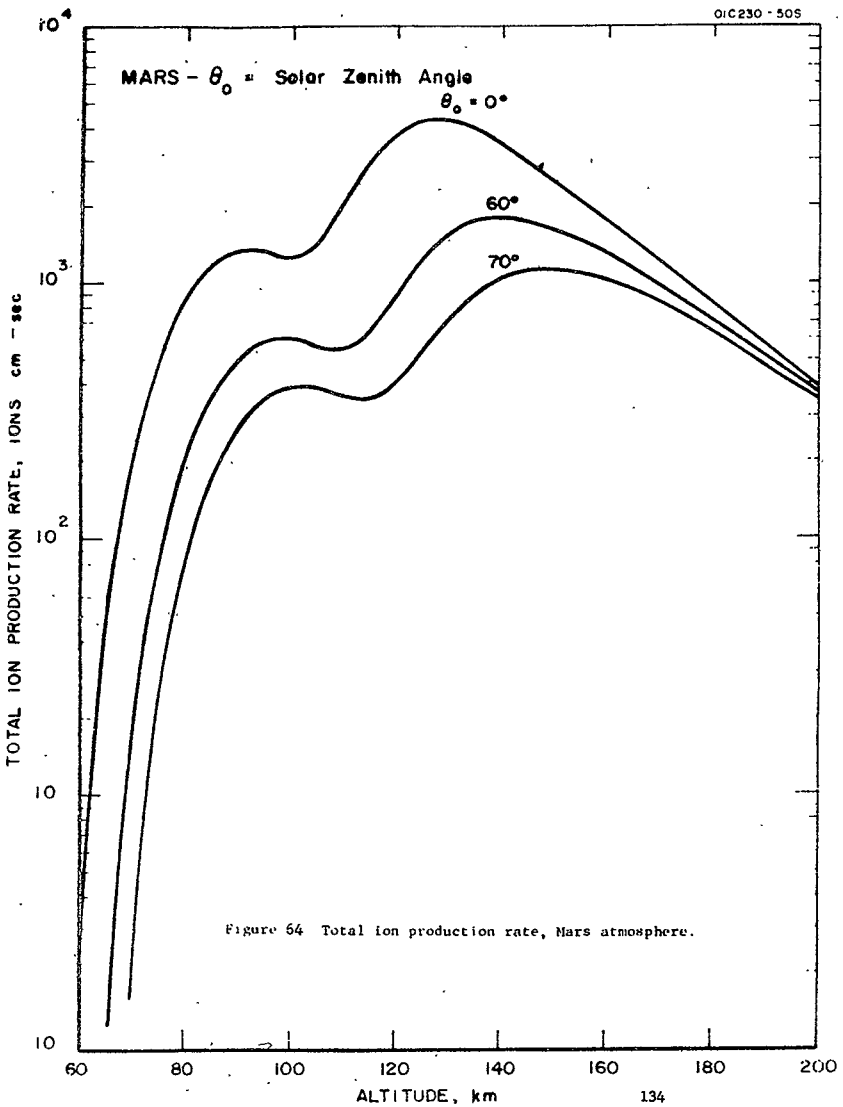

Figure 64 Total ion production rate, Mars atmosphere.

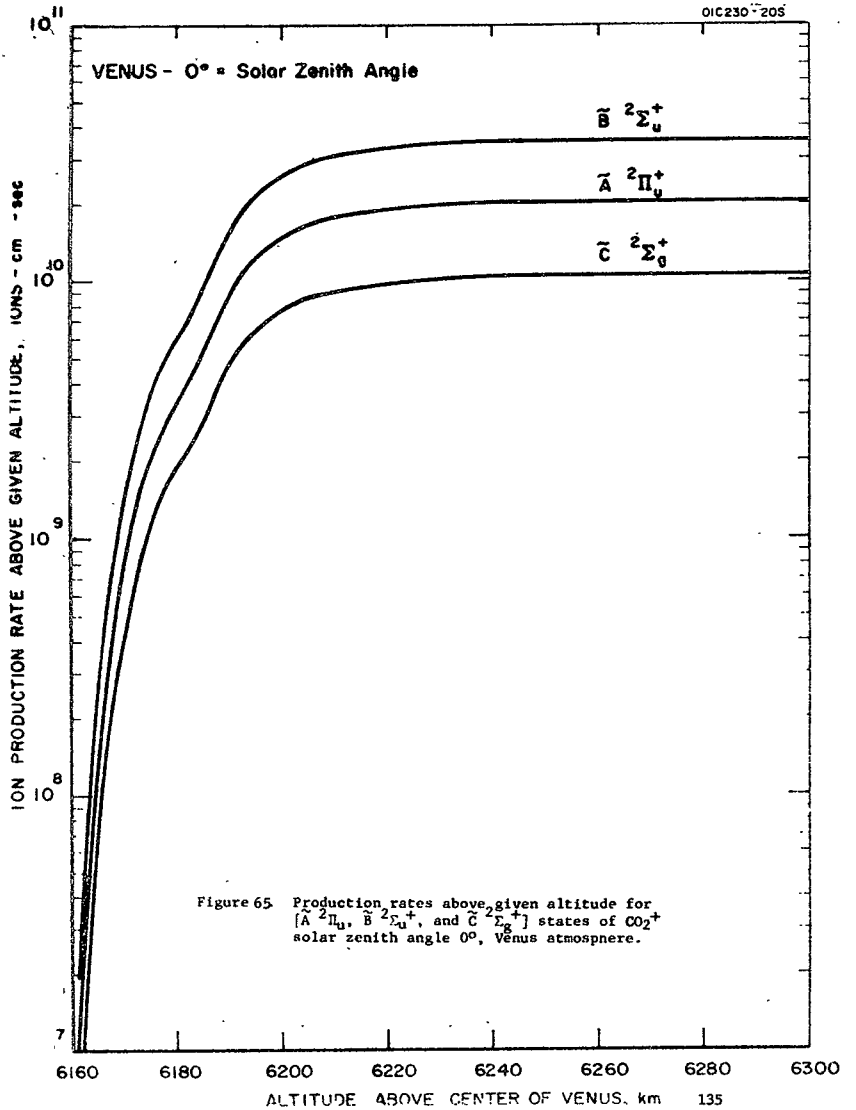

Figure 65. Production rates above given altitude for [$\tilde{A}\ ^2\Pi_u$, $\tilde{B}\ ^2\Sigma_u^+$, and $\tilde{C}\ ^2\Sigma_g^+$] states of CO_2^+ solar zenith angle 0°, Venus atmosphere.

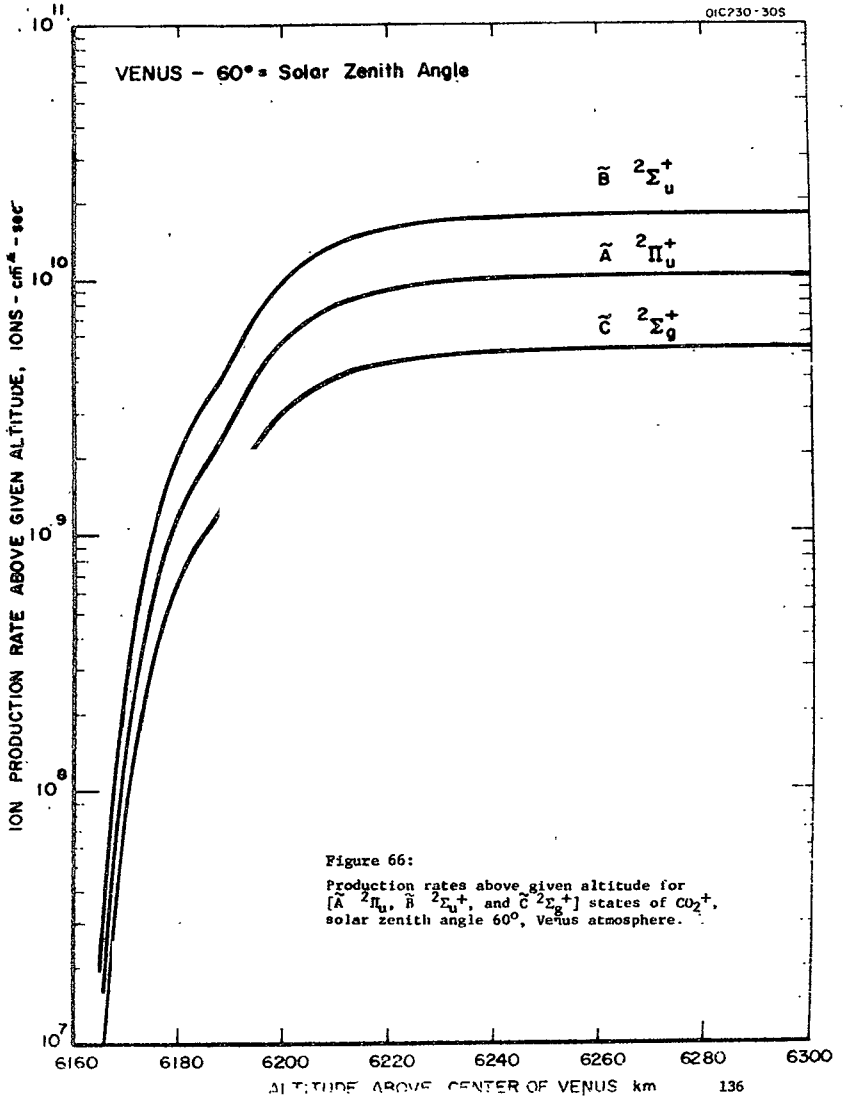

Figure 66:

Production rates above given altitude for [$\tilde{A}\ ^2\Pi_u$, $\tilde{B}\ ^2\Sigma_u^+$, and $\tilde{C}\ ^2\Sigma_g^+$] states of CO_2^+, solar zenith angle 60°, Venus atmosphere.

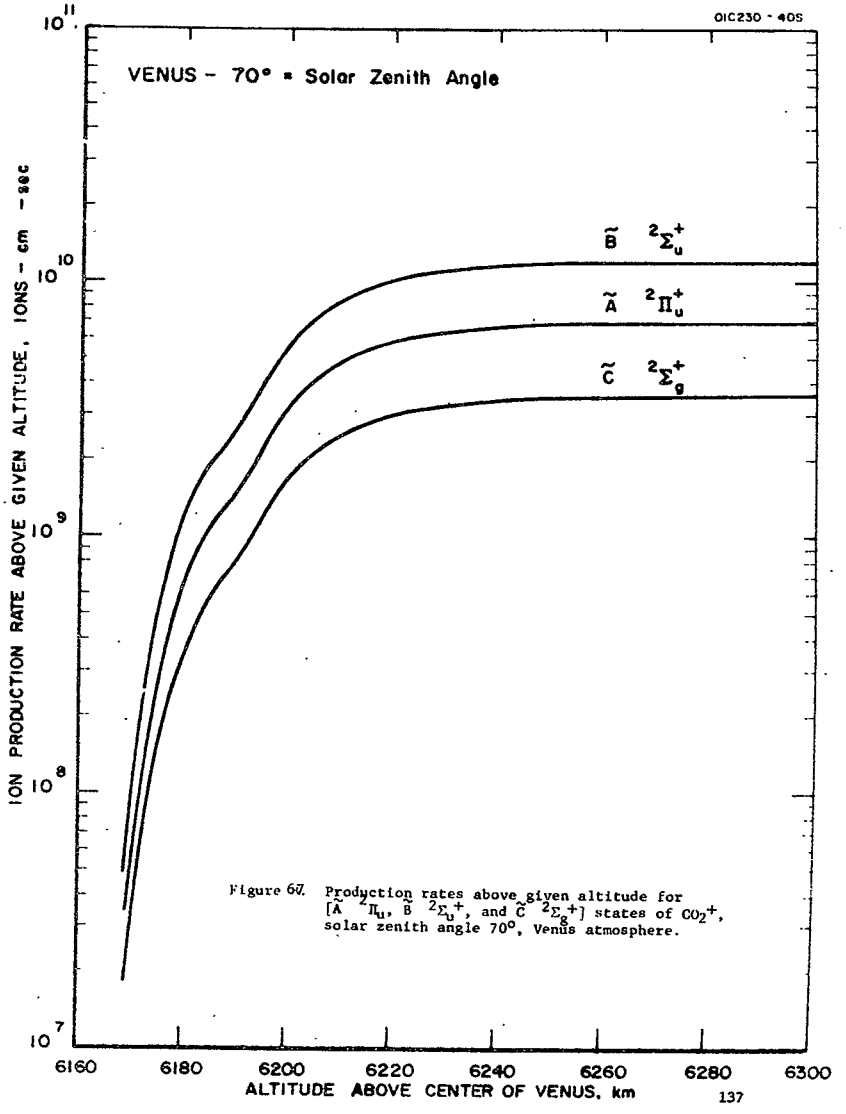

Figure 67. Production rates above given altitude for [$\tilde{A}\ ^2\Pi_u$, $\tilde{B}\ ^2\Sigma_u^+$, and $\tilde{C}\ ^2\Sigma_g^+$] states of CO_2^+, solar zenith angle 70°, Venus atmosphere.

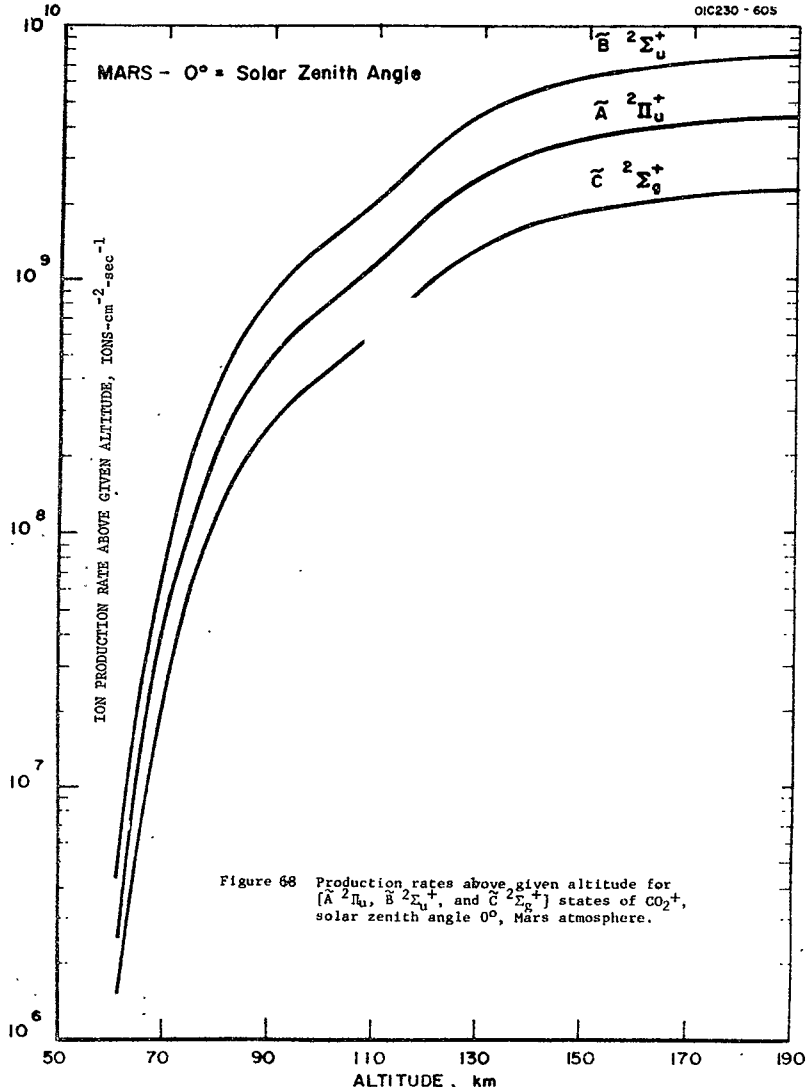

Figure 68 Production rates above given altitude for [$\tilde{A}\ ^2\Pi_u$, $\tilde{B}\ ^2\Sigma_u^+$, and $\tilde{C}\ ^2\Sigma_g^+$] states of CO_2^+, solar zenith angle 0°, Mars atmosphere.

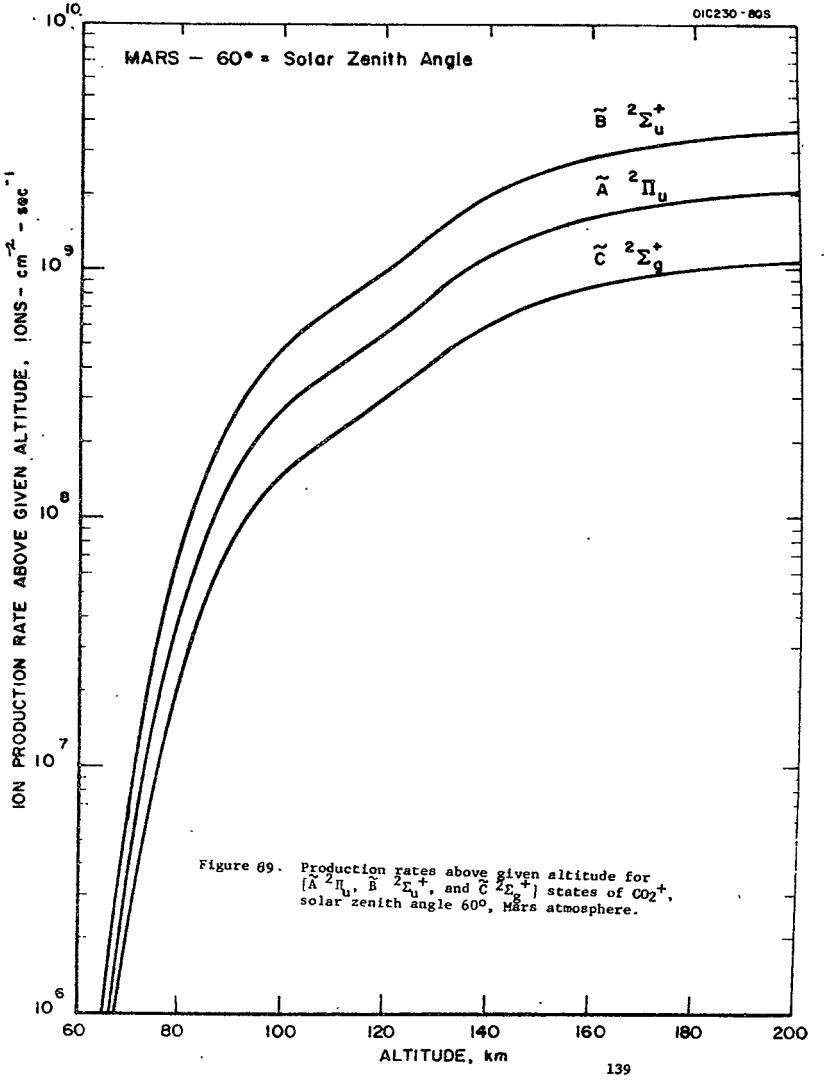

Figure 69. Production rates above given altitude for [$\tilde{A}\ ^2\Pi_u$, $\tilde{B}\ ^2\Sigma_u^+$, and $\tilde{C}\ ^2\Sigma_g^+$] states of CO_2^+, solar zenith angle 60°, Mars atmosphere.

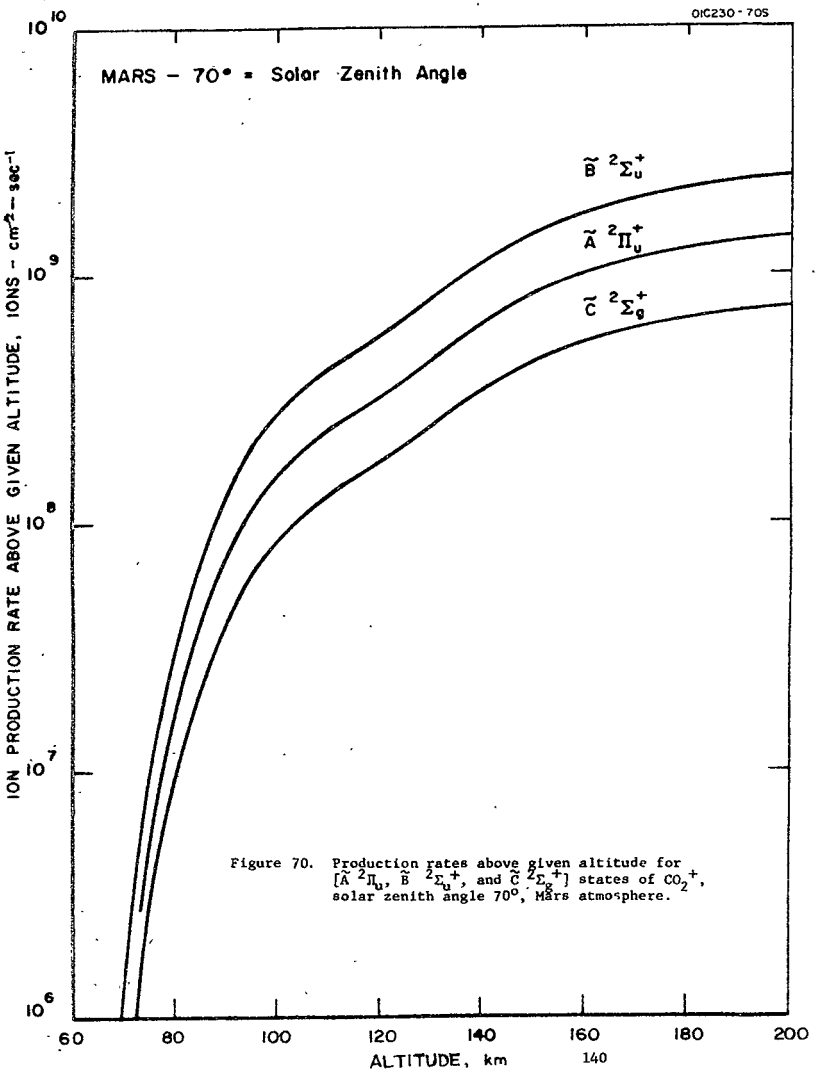

Figure 70. Production rates above given altitude for [$\tilde{A}\ ^2\Pi_u$, $\tilde{B}\ ^2\Sigma_u^+$, and $\tilde{C}\ ^2\Sigma_g^+$] states of CO_2^+, solar zenith angle 70°, Mars atmosphere.

TABLE 12

Total Production Rate of CO_2^+ States, Ions-cm^{-2}

Venus	Solar Zenith Angle, Degrees	STATE $\tilde{X}$	$\tilde{A}$	$\tilde{B}$	$\tilde{C}$	Total
	0	4.55×10^{10}	2.03	3.53	1.05	11.16
	30	3.94	1.76	3.06	0.908	9.67
	50	2.92	1.31	2.27	0.67	7.18
	60	2.28	1.02	1.76	0.52	5.58
	70	1.56	0.70	1.21	0.36	3.82
	80	0.79	0.35	0.61	0.18	1.94
Mars	0	10.25×10^{9}	4.58	7.95	2.36	25.15
	30	8.88	3.97	6.88	2.05	21.78
	50	6.59	2.95	5.11	1.52	16.16
	60	5.13	2.29	3.97	1.18	12.57
	70	3.51	1.57	2.72	0.81	8.60
	80	1.78	0.80	1.38	0.41	4.37

NOTE: Approximately 14 percent of the X $^2\Pi_g$ state ions are produced and approximately 25 percent of ions in the other states are produced in this way.

TABLE 13

Emission Rate from CO_2^+ States, kiloRayleighs

Venus	Solar Zenith Angle, Degrees	STATE $\tilde{A}$	$\tilde{B}$	$\tilde{C}$
	0	20.3	35.3	0.5
	30	17.6	30.6	9.1
	50	13.1	22.7	6.7
	60	10.2	17.6	5.2
	70	7.0	12.1	3.6
	80	3.5	6.1	1.8
Mars	0	4.58	7.95	2.36
	30	3.97	6.88	2.05
	50	2.95	5.11	1.52
	60	2.29	3.97	1.18
	70	1.57	2.72	0.81
	80	0.80	1.38	0.41

NOTE: Neglects any cascading, de-activation

"Spectrography of the Lunar Atmosphere." The proposed experimental investigation involves the employment of a compact, light weight, automatically operating spectrograph on the lunar surface to photographically record signature spectra of resonance and/or fluorescence scattering from solar illuminated lunar atmospheric species (or LEM contaminant species). The relatively high sensitivity achievable by the proposed instrumentation (ppm or less) and the extensive spectral region included in the measurement program ($\lambda\lambda$ 500 to 4500Å) result in the conduct of a survey experiment on establishing the presence or absence of specific lunar atmospheric species .

The proposed experiment is ideally suited for operation on the lunar surface. First, the spectrograph film format results in simultaneous integration over each individual spectral resolution so that the required broad spectral range can be covered at full sensitivity. In addition, since the proposed instrumentation encompasses a self-contained operational entity, power, telemetry, data sharing, interference, etc. characteristics need be considered in the conduct of the experiment. Upon comparison of the overall capabilities of the experiment performed at a remote observation platform to the suggested lunar surface program, the following advantages are apparent: (a) the experimental conditions remain essentially constant throughout the viewing time, i.e., the incident solar flux, the ambient background, column of specific species (signal source), the viewing position and angle, etc.; (b) species number densities are maximum at the surface so that the resultant cm^2-column count is optimized. This feature is especially evident in the detection of relatively heavy constituents, such as krypton, xenon, argon, etc. (which have relatively low scale heights from a remote platform); (c) the required astronaut activity is simple, minimum, and vital; (d) the delection of the surface-based viewing geometry is extremely flexible; (e) the instrumentation can be located in the vicinity of the LEM vehicle so that an opportunity exists for detecting fuel contaminants and measuring their inventories as a function of time.

The data acquired from the indicated experiments can be employed in the identification of dominant lunar atmospheric source and sink functions as well as the pertinent mechanisms involved. Additionally, the spectrographic data can be correlated with other Apollo mission measurement programs results, i.e., solar wind indicators, seismology, meteoric impact, etc.

Several observational experimental programs have been conducted previously to ascertain the existence, constituency, and extent of a lunar atmosphere. A concise summary of these results involving a broad variety of experimental techniques has been presented by Sytinskaya (Ref. 120). Highly sensitive experiments were performed by Lyot and Dollfus (Ref. 121) and Dollfus (Ref. 122) who were searching for the effects of Rayleigh scattering from a lunar atmosphere located just beyond the horns of a crescent moon. They employed a coronagraph to minimize instrumental

scattering of disk light and took advantage of the polarization characteristics of Rayleigh scattered light. Their results indicated that the total surface number density of the lunar atmosphere must be less than 10^{-9} that of the sea level terrestrial atmosphere (i.e. less than 3×10^{10} cm^{-3}).

On the basis of the results of a radio refraction experiment involving lunar occultation of the Crab Nebula, Elsmore (Ref. 123) deduced that a surface electron density of about 10^3 cm^{-3} in excess of that of the surrounding interplanetary medium obtains for the lunar atmosphere. On the basis of an extrapolation of these data, he suggested a new upper limit value for neutral species at the lunar surface of only about 2×10^{-13} earth atmospheres.

Herzberg (Ref. 124) suggested that the observation of characteristic fluorescences for specific species offered a sensitive species detection possibility. Subsequently, Kuiper (Ref. 125) established that lunar atmospheric SO_2 amounted to less than 7×10^{-10} earth atmospheres on the basis of the absence of absorption bands on observed lunar disk light. Recently, Marmo and Engelman (Ref. 126) defined a manned orbital experiment involving the observation of resonance radiations from solar illuminated neutral or ionic constituents in the lunar atmosphere. It was demonstrated both that a number of potentially important resonance lines occurred in the visible spectral region and that a meaningful experiment could be performed at an earth-based observatory.

Finally, Marmo and Manring (Ref. 127) utilized the Sacramento Peak coronagraph to image, occult, and track the lunar disk in an attempt to observe atmospheric contents of NaI, CaI, and CaII along the lunar limb. The results indicated upper limit values for these species of about 10^9/ cm^2-column.

For the purposes of the proposed experiment, the state of present development over the entire field of activity is sufficient so that no new technology is envisioned. For example, the required astronaut activity is straightforward though vital in nature, thus requiring minimum effort and instruction. Additionally, a prototype of the suggested instrumentation has been employed in a number and variety of high altitude rocket experimental programs designed to measure vacuum ultraviolet (VUV) airglow in the earth atmosphere. For the present application, the only requirements involve simple instrumental size reduction, operational compatibility with the lunar environment, and the design of a removable film casette for subsequent return to earth.

The Apollo mission experiment discussed herein involves the employment of a simple, light weight, automatically operated, dual spectrograph designed to perform observations in two spectral regions, i.e. $\lambda\lambda$ 2500-4500Å and $\lambda\lambda$ 500-2500Å. The experiment is to be performed on the

lunar surface in the protective shade of the LEM vehicle. The astronaut will initiate the pre-programmed experimental sequence of tasks which the instrument is designed to perform automatically. Subsequent to automatic shutdown, the astronaut will remove the capsule containing the roll film spectroscopic data for return to earth for development, data reduction, and analysis and interpretation. This initial experiment should be considered in terms of a general survey in that an extensive spectral region will be covered wherein the presence or absence of signals owing to resonance scattering from solar illuminated species in the lunar atmosphere can be detected with relatively high sensitivity. The recommended experimental technique will yield data which can represent meaningful inputs to the definition of relevant mechanisms producing the measured species number densities. The proposed experiment will be performed with existing state-of-the-art instrumentation and minimum, although vital, astronaut activity. The experimental objectives and results can be applied and correlated with other experiments performed under the Apollo mission program. Finally, on the basis of the derived experimental results, the location of a permanent astronomical airglow observing site on the lunar surface may be indicated which would operate essentially continuously and in direct communication with the earth.

A meaningful experiment designed to determine the constituency and extent of the lunar atmosphere must operate within the constraints of the accepted upper limit values of 10^6 cm^{-3} and 10^3 cm^{-3} for total surface number densities for neutral and ionic species, respectively (Refs. 120-123). Within these limits, several theoretical investigations have been performed, the results of which are described in the literature (Refs. 126, 128-131) so that a detailed discussion is not included herein. Suffice it to note that a number of representative possible lunar atmospheric constituents have been selected for the purposes of illustrating the present experimental capability and its applicability to the present state of knowledge. This species tabulation is presented in column 1 of Table 14 with corresponding relevant resonance wavelengths. Present theory does not allow one to estimate the inventories of the individual species which may be resident in the lunar atmosphere which represents the general rationale for the importance of the proposed general survey experiment. In lieu of this specific knowledge, the expected signal brightness values in Rayleighs (where 1 Rayleigh = 10^6 photons/cm^2 sec emitted in 4π steradians), are tabulated in column 3 of Table 14 for surface number densities, n_o, of only 1 cm^{-3} for the individual constituents. This sensitivity is expressed in an alternative fashion in column 4 of Table 14 in terms of minimum detectable n_o-values for an assumed detectability of 1.0 Rayleigh. Finally, the last column of Table 14 lists the major possible source functions of individual constituents considered as extracted from the literature (Refs 122-126). The above tabulation has been separated into two spectral categories, i.e. $\lambda\lambda$ 2500-4500Å, and $\lambda\lambda$ 500-2500Å, since the proposed investigation will be performed using two spectrograph systems consistent with this spectral

TABLE 14

SELECTED LUNAR ATMOSPHERIC SPECIES, POSSIBILITIES AND ASSOCIATED SPECTROGRAPHIC DETECTION CAPABILITIES

Species	λ(Å)	Expected Signal Brightness (Φ, Rayleighs) for Surface Number Density (n_o, cm^{-3})=1	Minimum Detectable n_o-Value for Φ=1R	Major Sources of Constituent in Lunar Atmosphere**
		λλ 2500-4500Å		
Ca I	4227	9.3(0)* Rayleigh	1.1(-1)* cm^{-3}	SW-ME
***K I	4044	5.9(0)	1.7(-1)	SW-ME
Ca II	3934	1.2(1)	8.3(-2)	SW-ME
Fe I	3441	6.1(-1)	1.6(0)	SW-ME
Ni I	3370	6.5(0)	1.5(-1)	SW-ME
Ti I	3342	3.4(1)	2.9(-2)	SW-ME
***Na I	3302	2.6(0)	3.9(-1)	SW-ME
***Li I	3233	3.8(0)	2.6(-1)	SW-ME
Aℓ I	3082	8.7(0)	1.1(-1)	SW-ME
Mg I	2852	1.2(1)	8.3(-2)	SW-ME
Mg II	2796	3.8(0)	2.6(-1)	SW-ME
Fe II	2599	2.1(0)	4.8(-1)	SW-ME
Si I	2514	6.3(-1)	1.6(0)	SW-ME
		λλ 500-2500Å		
C I	1657	1.4(-2)	7.1(1)	SW-ME-VO-FC
Xe I	1470	9.2(-5)	1.1(4)	SW-RA-PR
O I	1304	9.0(-5)	1.1(4)	SW-ME-VO-FC
H I	1216	4.9(-1)	2.0(0)	SW-VO-FC
N I	1200	2.6(-4)	3.8(3)	SW-ME-FC
Kr I	1165	4.9(-6)	2.0(5)	SW-RA
Ar I	1048	1.1(-5)	9.1(4)	SW-RA-PR
Ne I	736	4.0(-6)	2.5(5)	SW
He I	584	1.8(-4)	5.6(3)	SW-RA

*number in parentheses denotes power of ten, i.e. 1.0(2) = 1.0×10^2

**SOURCE FUNCTIONS:
SW, solar wind; ME, meteoric bombardment; VO, volcanic activity; RA, radioactive decay; PR, original atmospheric residua; FC, fuel contaminants

***the tabulated wavelengths pertain to second resonance lines of the species; the first resonance lines are K I (7665), Na I (5890), Li I (6708).

dichotomy. The instrumentation is duscussed in greater detail in the following section where it is demonstrated that system detectabilities can be achieved which correspond to signal intensities between about 1 to 10 Rayleighs. On this basis, the data in Table 14 indicate that this instrumentation capability will result in high probability of detecting and identifying (or alternatively, establishing meaningful upper limit surface density values) a large number and variety of possible lunar atmospheric species.

The proposed experiment is predicated on the employment of a simple design spectrograph of reasonable resolution which is both compact and light weight. An optimum design for the present experimental purpose is shown in Figure 71 which illustrates the optical configuration of a simple normal incidence spectrograph. In Figure 71 the housing geometry is indicated in order to illustrate the compact nature of the resultant spectrograph. The entrance slit, grating and plate holder positions indicated in the figure lie on the Rowland circle so as to achieve sufficiently good focus for an extended wavelength region. An existing prototype for the present application has been designed, fabricated, and calibrated by McPherson Instrument Co. (a division of GCA Corporation) and utilized in a variety of rocket experiments designed to obtain vacuum ultraviolet spectra in the earth upper atmosphere is shown in Figure 72. A technique of stacking the two module assemblies for compactness is also illustrated in the figure. Further details of the basic spectrograph instrument are not included herein since these are available in the literature (Ref. 132). The recommended optical configuration involves overall unit assembly spectrograph dimensions of 4 inches depth by 8 inches width by 10 inches length (i.e., 320 in^3) with a weight of less than 5 lbs./instrument. Finally, it can be seen from the schematic of Figure 72 that the option is available to incorporate either a single spectrograph or the dual instrument on any specific Apollo mission.

The critical instrumental parameters are listed in Table 15 for both spectrograph designs wherein the indicated values have been assigned tentatively on the basis of a preliminary analysis of the present problem. It should be stressed at this point that all of the parametric requirements stipulated in this tabulation can be accomodated by off-the-shelf and state-of-the-art components. Brief discussions are presented below of the individual parameters included in Table 15 for both instrumental designs.

The indicated gratings are available from Bausch and Lomb (Ref. 133) and other suppliers. The overall instrumental transmissivity estimate of 0.5 for $\lambda\lambda$ 2500-4500Å is considered conservative owing to the high reflectivity of materials and grating efficiencies of this spectral region. Alternatively, for the spectral region $\lambda\lambda$ less than 1500Å, it is well-established (Ref. 133) that reflectivities can be enhanced significantly by employing stock item platinum coated gratings which have been overcoated with magnesium fluoride. Therefore, an overall transmissivity of

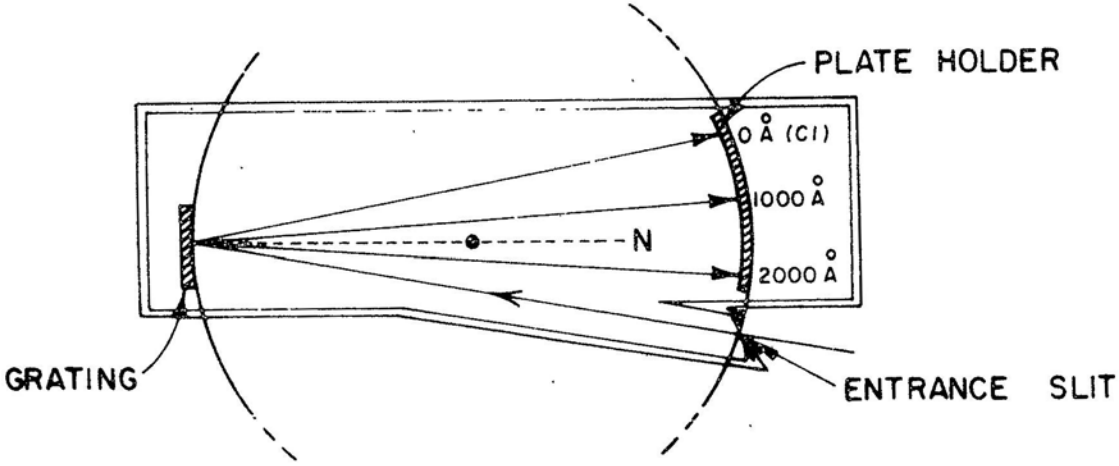

FIGURE 71 An optical configuration of a normal incidence spectrograph. The housing geometry is shown to illustrate the compact nature of this configuration. The dotted portions represent extension of Rowland circle.

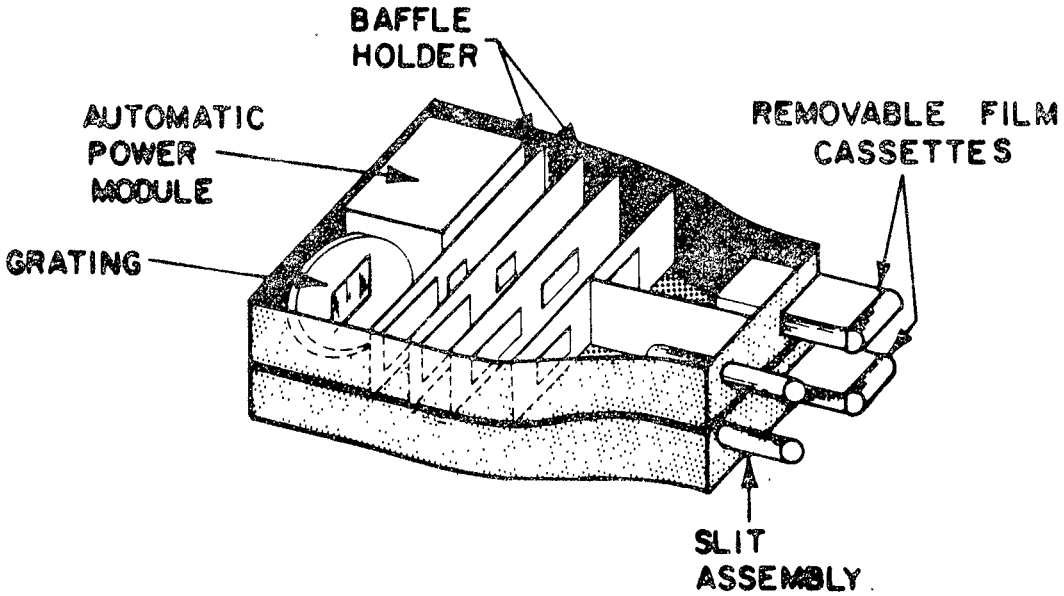

FIGURE 72: Detailed drawing of existing prototype. The overall dimensions are 4 x 8 x 10 inches

TABLE 15

INSTRUMENTAL PARAMETERS FOR PORTABLE SPECTROGRAPHS

	Spectrograph #1 λλ 2500-4500Å	Spectrograph #2 λλ 500-2500Å
Optical Specifications		
Grating Specifications		
Grating Type	Concave blazed reflecting	Concave blazed reflecting
Focal Length, cm	20	20
Grating blaze, Å	3200 (first order)	1200 (first order) 600 (second order)
Grooves/mm	1200	1200
Ruled area, mm	53 x 56	53 x 56
Reciprocal dispersion Å/mm	~40	~ 40
Omega, Ω, steradians ($x10^{-2}$)	7.4 (FOV ~15°)	7.4 (FOV ~15°)
Slit width, cm	0.10	0.10
Slit length, cm	1.0	1.0
Overall Transmissivity	0.5	0.5
Film Specifications		
Type	Kodak 2485	Kodak 101-01
Wavelength sensitivity, Å	2200-6700	50-4000
Exposure Required for minimum density E, ergs/cm^2 ($x 10^4$)	5.0	4.2
Mean E value, photons/cm^2 ($x 10^{-7}$)	8.0 (λ = 3200Å)	2.5 (λ = 1200Å)
Reciprocity Failure	Negligible	Negligible
Availability	Roll Form	Roll Form
Instrument Overall Specifications		
Size, inches	4 x 8 x 10	4 x 8 x 10
Weight, lbs.	5	5
Power requirements	None	None
Data measurements requirements	None	None
Data support requirements	None	None

0.5 was selected throughout the entire spectral region for the purposes of the present discussion. In practice, it is planned to establish the transmissivities of the individual spectrographs on the basis of a laboratory measurement program.

The rationale for the film selections of Table 15 can be discussed in terms of Figures 73, 74, and 75. Specifically for λλ 2500-4500Å Kodak 2485 film was selected on the basis of the spectral sensitivity curves of Figure 73 which was extracted directly from the appropriate Kodak data sheet. These published data were employed to obtain the corresponding E-values shown in Table 15. In the present experimental mode, it can be anticipated that relatively long exposure times may be involved so that the role of reciprocity failure must be considered. In this regard, it should be stressed that Lewis and James (Ref. 134) have concluded recently that reciprocity failure was negligible when the film was employed under vacuum conditions. The resultant behavior is summarized in Figure 74 which was extracted directly from the cited paper. In addition, the results of the figure indicate that an increase in sensitivity occurs under vacuum conditions although this conclusion should be considered tentative. In any case, for the present purposes reciprocity failure was assumed to be negligible so that the sensitivity curves of Figure 73 are applicable for exposures up to about 10^4 seconds.

For the spectral region λλ 500-2500Å, the Kodak 101-01 film selection was predicated on the following rationale. An investigation was performed recently by W. K. Fowler, et al (Ref. 135) on the absolute calibration of SC-5 film employed for far ultraviolet rocket spectroscopy. A series of exposures of SC-5 film at a wavelength of 1200Å is shown in Figure 75 which has been extracted directly from the cited paper (Ref. 135). It can be seen that, even for an exposure time of 1/20 of one second and a beam intensity of 1.7×10^{-2} ergs/second, sufficient film exposure was obtained (for the indicated development process) as shown in the lower left slit image in Figure 75. On the basis of more recent experimental results, it is now recognized (Ref. 136) that Kodak 101-01 film is both about 50 percent faster than the SC-5 film and also results in a clearer background upon proper development. Additionally, it has the further advantage of being available in roll form. On the basis of this increased capability, as well as the degree of darkening observed in the lower left slit image of Figure 75 estimates were derived for the exposure required for the minimum operating density of Kodak 101-01 film which are presented in Table 15. With respect to reciprocity failure, Fowler, et al (Refs. 135,136) have concluded that for SC-5 and 101-01 film, it is completely negligible. Therefore, it is appropriate to apply the tabulated E-value to the calculation of exposure times required for the purposes of the present experiment.

It is suggested that the dual assembly spectrograph be operated within the protective shadow of the LEM. The optical axis of the instrument should be pointed about 10° above the lunar horizon with the slit oriented in the anti-solar position in order to minimize any degradation introduced

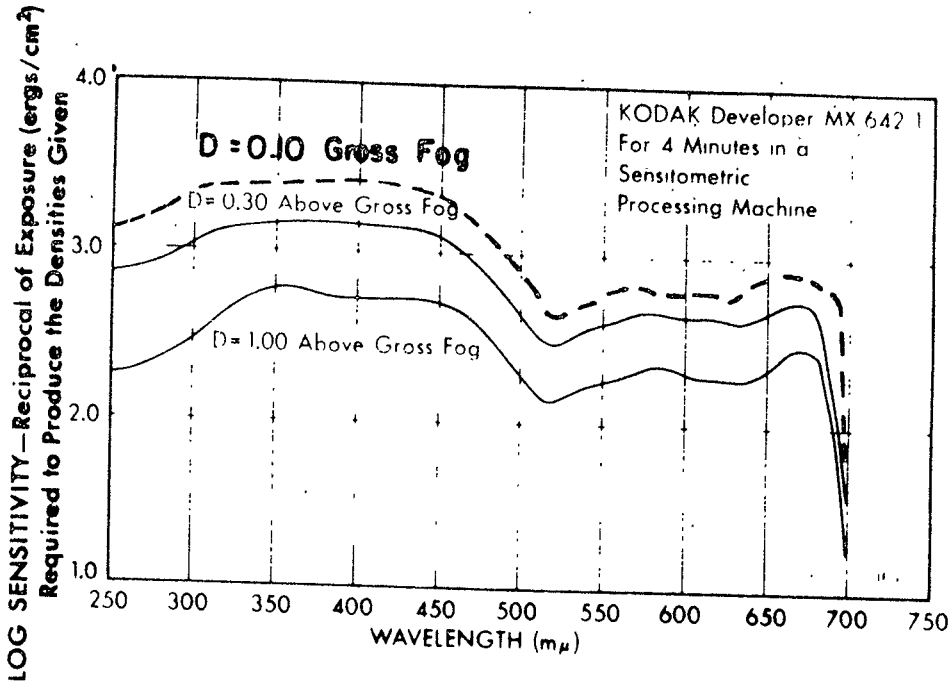

FIGURE 73 Spectral sensitivity of Kodak 2485 high speed recording film. The dotted curve obtains for D = 0.10.

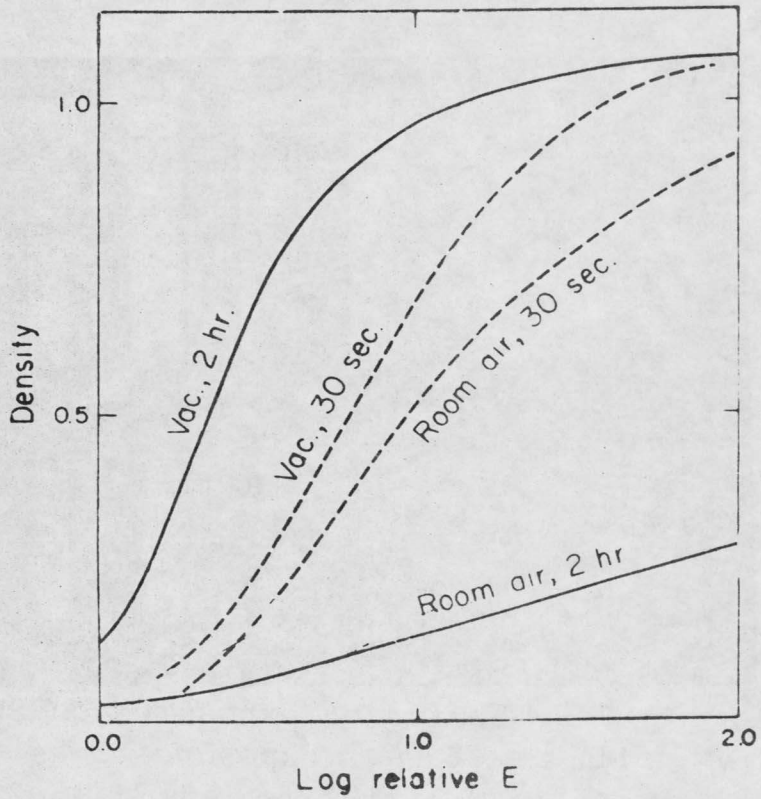

FIGURE 74 Characteristic curves for blue light exposure in room air and vacuum of pure bromide emulsion without deliberate chemical sensitization. Exposure times are noted on each curve.

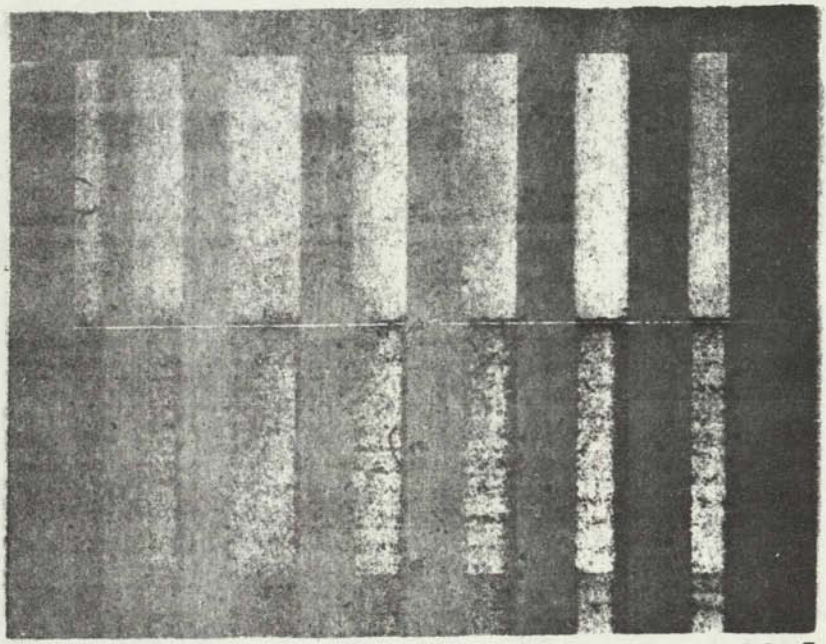

Figure 75. Series of exposures on SC-5 film at 1200Å. Exposure times were 1/20, 1/10, 1/5. 1/2. 1, 2, 4, & 8 sec to a beam of 1.7×10^{-2} ergs/sec total flux. After exposure the film was cut in two and the upper half developed in DK-20 for 12 min while the lower half was developed in D-19b for 2 minutes.

by surface scattered radiation. This observational configuration can be instituted by the astronaut either by means of a built-in tripod arrangement or by simply suspending the dual spectrograph from a pre-selected location on the bottom section of the LEM vehicle. The astronaut would then initiate the instrumental operation mode wherein the entire sequence of pre-programmed exposures would be performed automatically through equipment shutdown (which occurs after several hours of operation). The only other required astronaut activity involves removal of the portable roll film holder for return to earth for subsequent film processing and data reduction and analysis. Thus, it is evident that although minimum astronaut activity is involved in the conduct of the proposed experiment, his role is vital to its successful performance.

As indicated previously, meaningful constituence data will be obtained for a system detectability of between 1 and 10 Rayleighs as shown in Table 14. On this basis then, a number of suggested exposure times have been selected employing the parametric instrumentation values discussed above and listed in Table 15. At this point, it is convenient to define the following useful parameters:

X_B = the brightness value for the background radiation contained within the spectral resolution of one slit element. For convenience, this is given in units of Rayleighs (see Figure 76).

X_s = the brightness for the spectrally discrete signals falling on the entrance slit. For convenience this is given in units of Rayleighs (see Table 14)

A = slit area, cm^2

Ω = viewing solid angle, steradians

T = overall transmissivity, 0.50

t = time of exposure, seconds

Φ = integrated exposure relevant to one slit area element image on photographic film. ergs/cm^2-slit area and/or photons/cm^2-slit area

E = Φ/A; integrated exposure relevant to 1 cm^2 image of photographic film (see Figures 73 and 74).

It is appropriate now to evaluate the exposure times required to achieve a 1 to 10 Rayleigh detection capability. This can be estimated in the following manner:

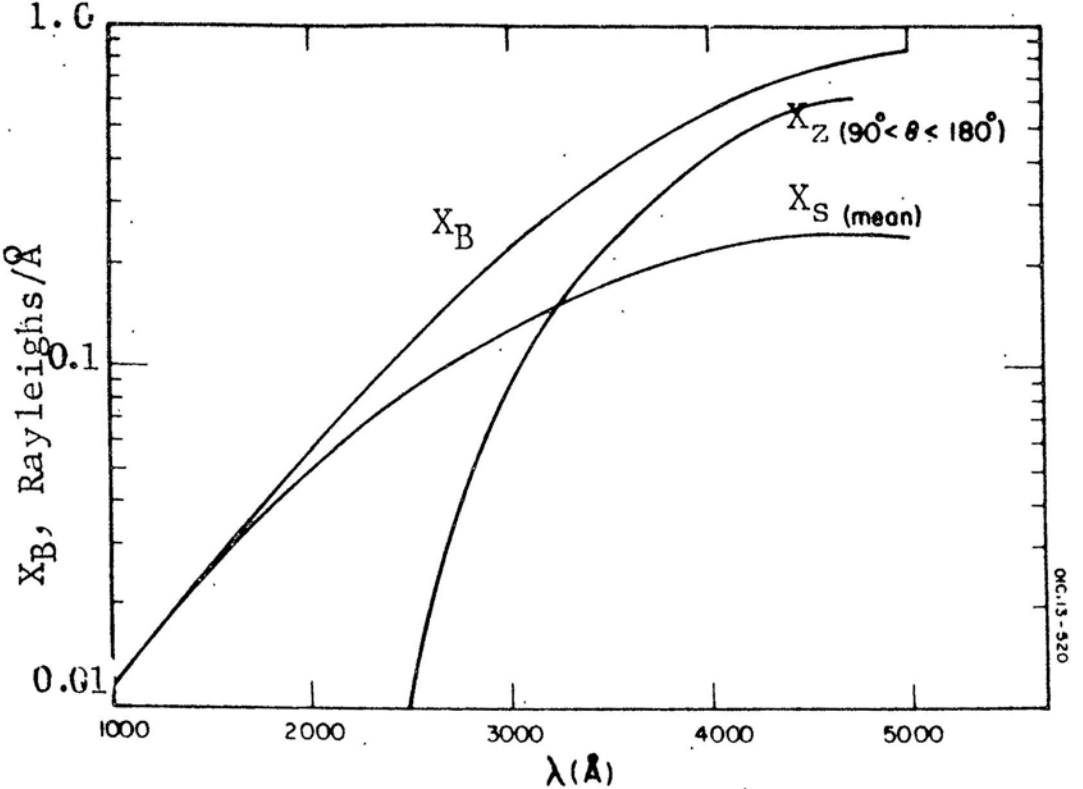

FIGURE 76 Total background intensity $X_B = (X_S+X_Z)$ as a function of wavelength for mean galactic sky conditions and average

$$\Phi = (A\Omega)\ T\ \frac{[(X_s + X_B)\ t]}{4\pi} \tag{53}$$

so that

$$E = \frac{\Omega\ T\ [X_s + X_B)\ t]}{4\pi} \tag{54}$$

substitution from Table 15 yields:

$$E = 3.0 \times 10^{-3}\ [(X_s + X_B)\ t] \tag{55}$$

Equation (53) is plotted in Figure 77 where E-values of between 10^7 and 10^8 photons/cm^2 (see Table 15) are plotted as a function of exposure times (t) in the range between 10 and 300 minutes. For future reference a number of selected $(X_S + X_B)$-values are included which range between 0.5 and 40 Rayleighs. On the basis of these data, the background data shown in Figure 76, and the instrumental characteristics listed in Table 15, it will be demonstrated that a 1-10 Rayleigh signal brightness detectability can be achieved by proper operation of the dual spectrograph on the lunar surface.

The results of Figure 77 demonstrate the exposure time is selected on the basis of the anticipated $(X_S + X_B)$-value. It is important to stress here that the X_B-value is pertinent to the determination of the proper exposure time. Specifically, it is evident from the data in Figure 76 that the X_B-value exhibits significant variation over the spectral regions suggested for the two spectrograph instruments. Specifically, for $\lambda\lambda$ 2500-4500Å, X_B-values of between 4 and 40 Rayleigh (spectral resolution ~ 40Å) obtain. Alternatively for the spectral region $\lambda\lambda$ 500-2500Å, the background contribution can be ignored for the most part. For this reason, exposure estimates are obtained individually for the two spectrograph systems.

With respect to $\lambda\lambda$ 2500-4500Å, a practicing rule of thumb of photography involves successful image detection against a strong background when the brightness of the image amounts to at least 10 percent of the background, i.e. $(X_S + X_B)/X_B \geq 1.1$. However, this rule prevails for photographic systems operating on the straight portion of the film gamma curve. This is illustrated in Figure 78 where $X_S = X_B$ for which the resultant discrimination of signal against background is readily apparent. Owing to the lack of relevant information on the gamma curves of the presently considered film systems, a conservative approach is adopted wherein it is assumed that spectral discrimination can be achieved when $(X_S + X_B)/X_B \geq 1.25$. On this basis, it is evident that proper exposure time selection must be predicated on the basis of the magnitude of the applicable background brightness rather than the signal brightness for $\lambda\lambda$ 2500-4500Å. Thus, according to Figure 77, for an E-value of 8.0×10^7 photon/cm^2

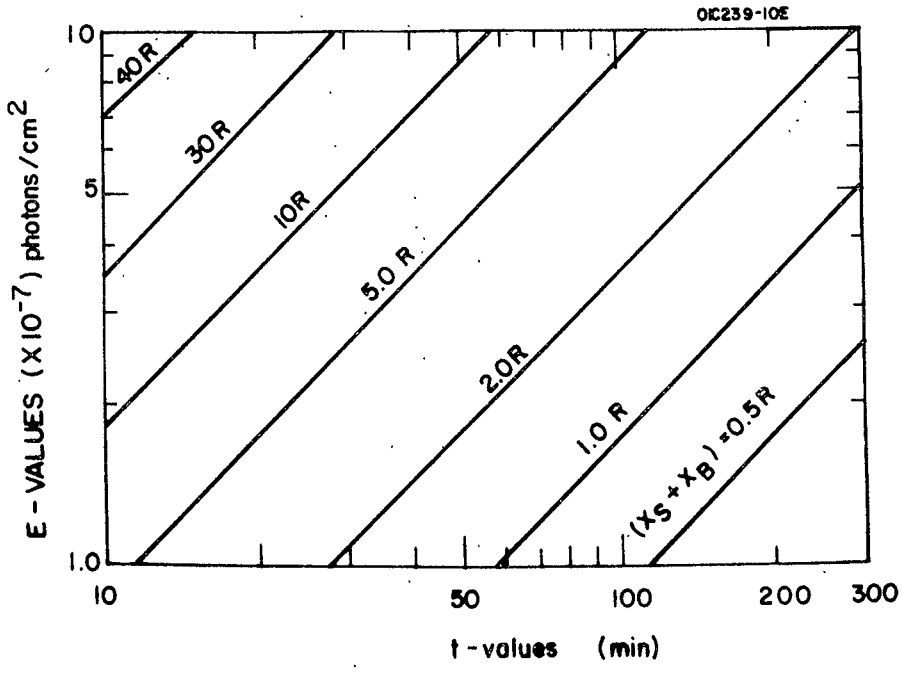

FIGURE 77 Plot of E-values in photons/cm^2 vs. t-values in minutes for a number of selected ($X_s + X_B$) - values. These data can be employed to relate required exposure times to desired detectivity.

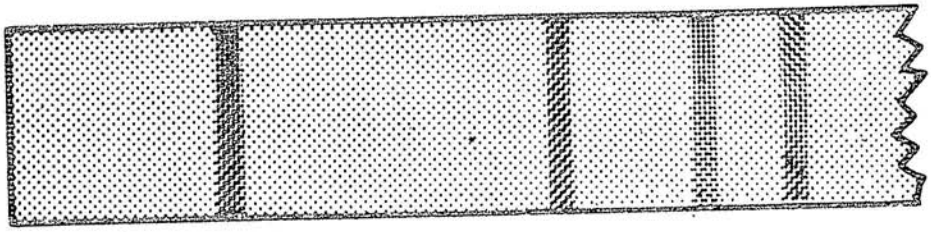

FIGURE 78 Schematic of typical photographic spectra wherein the signal and background film densities are equal.

presented in Table 15, exposure times of between 10 and 100 minutes are required for X_B-values of 40-4 Rayleighs, respectively. According to the detection criterion discussed above, a corresponding signal detection capability would be realized of between 10 and 1 Rayleigh, respectively. As a consequence, a recommended program of exposures would be employed in practice which includes exposure times of 1-300 minutes.

In contrast to the above situation, the spectral region λλ 500-2500Å involve no significant background contributions according to Figure 76. For this case, exposure time selection is predicated only on the basis of the magnitudes of the expected X_B-values. In this regard, the data of Figure 77 suggest that for the derived E-value of 2.5×10^7 photons/cm^2 similar exposure times as those derived above for the λλ 2500-4500Å spectral region obtain for a 1-10 Rayleigh signal detection capability for the λλ 500-2500Å spectral region. Accordingly, it is recommended that an exposure time sequence identical to that obtained previously for λλ 2500-4500Å of between 10 and 300 minutes be selected for this lower spectral region.

Relevant to the above discussion, it may be noted that a well-established practice involves the controlled pre-exposure (to threshold) of fast film in order to enhance its speed characteristics.

The above suggested exposure time sequences should be regarded as tentative estimates since the final selection will be determined both on the basis of the specific prevalent background conditions as well as laboratory calibration of the optical components and films in the individual spectrograph systems. In this regard, an alternative instrumental configuration which would involve the employment of image intensification has not been considered herein owing to the additional instrumental complexities which would be introduced. However, in the event that such lower exposure times are necessary, this alternative could be applied to this experiment.

The photographic spectra obtained in the conduct of the proposed experiment require minimum analysis, since the film format intrinsically yields the unambiguous spectral locations of resonance scattering of the individual species. Alternatively, detailed interpretation of these results is expected to involve a considerable effort. For example, it is anticipated that the explanation of positive results will involve a detailed investigation to identify the major processes contributing to the existence of specific species in the lunar atmosphere. In addition, any measured time variation of the content of a given species will involve the identification of specific phenomenological sink and source functions such as solar wind activity, meteoric impact, LEM fuel contaminants, etc. It should be emphasized, however, that even negative results can be employed to establish meaningful upper limit values for a large number and variety of possible lunar atmospheric constituents. These data can then be utilized

to preclude or evaluate the roles of several suggested mechanisms contributing to the lunar atmosphere. Finally, the overall experimental results can be employed to evaluate the validity and feasibility of establishing a permanent astronomical-airglow lunar surface station to monitor selected lunar atmospheric species and communicate these data routinely to earth.

Successful performance of the proposed experiment would be assisted greatly by the performance of parallel, theoretical and laboratory investigations. The theoretical effort should involve an investigation of the relationship between specific lunar atmospheric species and appropriate source and sink functions as well as the mechanisms involved in generating steady-state concentrations. The laboratory investigation should involve the measurement of the optical characteristics of the two suggested spectrograph systems as well as absolute calibration of the films for employment herein. These supporting data would then be employed in the cogent interpretation of the derived experimental results.

III. MISCELLANEOUS TOPICS

This section contains brief summaries of the scientific material generated under the present program and presented at scientific and/or professional meetings. In addition, there is included other miscellaneous topics of interest in the performance of the current contract commitments.

During the current reporting period, Dr. James A. R. Samson attended the IAGA symposium on "Laboratory Measurements of Aeronomic Interest" held at the University of York, Toronto during 3-4 September 1968 and also to visit the laboratories of Dr. Marmet at the University of Laval, Quebec City, Canada.

Of particular interest to the present contract was the paper presented by Dr. R. Schoen on Photoelectron Spectroscopy, Photoionization and Photoabsorption Measurements. He pointed out that the absorption cross sections of CO_2 vary widely from observer to observer and although he believed the values obtained at GCA were the best available he felt that they should be remeasured. He also brought up the importance of the angular distribution of the photoelectrons in photoelectron spectroscopy experiments. Independently of the work produced at GCA, he also arrived at the look angle of $54^{o}44'$ for observations in order to eliminate any confusion of the results due to varying angular distributions.

McElroy brought out the fact that the abundance of atomic nitrogen produced by dissociative ionization appears to be too small to account for what he expects to exist in the upper atmosphere. The discussions on this point suggested that electron impact collisions with N_2 may be the major instrument for producing dissociative ionization.

Dr. Hoffman of the AFCRL, gave an excellent review of the present state of absorption cross sections of atmospheric gases and pointed out the need for continued measurements at higher wavelength resolution.

At Laval University, Dr. Marmet described his new ideas for measuring the kinetic energies of photoelectrons. His new analyzer is basically a 127^{o} cylindrical deflection analyzer with a modification to provide a higher transmission of electrons. The device looks extremely promising for photoelectron work. However, it has not been tested as yet and we propose to hold off making this type until such time as Dr. Marmet has more information on its energy resolution and other characteristics. Dr. Marmet has had many years of experience dealing with electron and ion optics and he was able to provide invaluable suggestions about the techniques in working with electrons, especially in methods to remove local magnetic fields.

Dr. James A. R. Samson attended the 21st Annual Gaseous Electronic Conference held at the University of Boulder, Boulder, Colorado, 16-18 October 1968. Dr. Samson presented a paper entitled "Higher Ionization Potentials of Molecules Determined by Photoelectron Spectroscopy." This paper was received with considerable interest since there is an accelerating

activity in the new field of electron spectroscopy. Historically, this conference deals with photon-atom interaction, atom-atom interactions, ion-molecule reactions and electron-molecule interactions. Many of these areas are of direct interest to the performance of the current contract commitments. Of particular interest to some current problems in photo-electron spectroscopy was a paper entitled "Configuration Mixing of Continuum States" presented by A. J. Mendez. This theoretical paper has been of significant importance in defining future pertinent experimental measurements. For example, it was pointed out that it would be of significant importance to measure the coefficients A and B for the angular distribution of photoelectrons in wavelength regions wherein auto-ionization and overlapping continuum states occur. With the experimental values availalbe, the theoretician could then determine the proper wave functions of the states involved.

During the conference local visits were made to NCAR and ESSA. E. Ferguson (ESSA) deomonstrated laboratory evidence for the reaction $He^+ + N_2 \rightarrow N_2^+ + h\nu$ ($\approx$ 2000Å). This was of special interest to our laboratory effort, since GCA has previously observed "fluorescence" in He at wavelengths shorter than those corresponding to the ionization potential. On the basis of Ferguson's data it would appear then, that these emissions could have been due to N_2 impurities in the gas sample.

Dr. Frederick F. Marmo attended the COSPAR meeting at Prague, Czechoslovakia, for the purposes of presenting a paper entitled, "On the Presence of Carbon Atoms in the Upper Atmosphere of Venus." A rather large number of other papers presented at the meeting were relevant to the task requirements included in the present contract. As such a significant amount of valuable input data were obtained and will be incorporated in forthcoming reports as required.

The the First Annual Meeting of the Division of Electron and Atomic Physics of the American Physical Society on 17-19 November 1969 a paper entitled "Angular Distributions of Photoelectrons and Partial Photoionization Cross Sections" was given by Dr. James A. R. Samson of GCA Technology Division, Bedford, Massachusetts. An experimental arrangement was given for measuring the angular distribution of photoelectrons. The asymmetry coefficient, β, was found to be 0.3 for argon, and 0.3 and 0.12 for molecular nitrogen at 584Å when the residual ion core is left in its $X^2\Sigma$ and $A^2\Pi$ states, respectively. The partial photoionization cross sections were given for O_2 at 186, 209, 247, 330 and 460Å. New ionization potentials for O_2 were found at 23.5, 24.6 and 27.3 eV $\pm$ 0.3 eV.

REFERENCES

1. Calcote, H. F. and D. E. Jensen. Advan. Chem. Ser. 58, 291 (1966).

2. Miller, W. J., Symp. Combust. 11th Univ. California, Berkeley, Calif. 1966, 311 (1967)

3. Fontijn, A., W. J. Miller, and J. M. Hogan, Symp. Combust. 10th Univ. Cambridge, Cambridge, England, 1964 545 (1965).

4. Fite, W. L., A. Rutherford, W. R. Snow and V. A. T. van Lint, Ion-neutral collisions in afterglows, Discussions Faraday Soc. 33, 264 (1962).

5. Saporoschenko, M., Ions in nitrogen, Phys. Rev. 111, 1550 (1958).

6. Varney, R. N., Drift velocities of ions in oxygen, nitrogen, and carbon monoxide, Phys. Rev. 89, 708 (1953).

7. Kovar, F. R., E. C. Beaty, and R. N. Varney, Drift velocities of ions in nitrogen at various temperatures, Phys. Rev. 107, 1490 (1957).

8. Warneck, P., Laboratory rate coefficients for positive ion-neutral reactions in the ionosphere, J. Geophys. Res. 72, 1651 (1967).

9. Asundi, R. K., G. J. Schulz, and P. J. Chantry, Studies of N_4^+ and N_3^+ ion formation in nitrogen using high-pressure mass spectrometry, J. Chem. Phys. 47, 1584 (1967).

10. Warneck, P., Studies of ion-neutral reactions by a photoionization mass spectrometer technique, J. Chem. Phys. 46, 502 (1967).

11. Varney, R. N., Discussion of letter by Peter Warneck, "Laboratory rate coefficients for positive ion-neutral reactions in the ionosphere," J. Geophys. Res. 72, 5578 (1967).

12. Sun, H. and Weissler, G. L., J. Chem. Phys. 23, 1160 (1955).

13. Watanabe, K., Zelikoff, M. and Inn, E. C. Y., AFCRL Tech. Rept. No. 53-23, Geophys. Res. Paper No. 21 (1953).

14. Wilkinson, P. G., Can. J. Phys. 34, 596 (1956

15. Saporoschenko, M. Phys. Rev. 132, A 352 (1965).

16. Keller, G. C., Martin, D. W. and McDaniel, E. W., Phys. Rev. 140A 1535 (1965).

17. Curran, R. K., J. Chem. Phys. 38, 2974 (1963).

18. Samson, J. A. R. and Myer, J., Absorption Cross Sections of Minor Constituents in Planetary Atmospheres from 1050 to 2100Å, GCA TR 69-7-N (March, 1969).

19. McNesby, J. R., J. Atmos. Sci. 26, 594 (1969).

20. Sagan, C. E., Radiation Res. 15, 174 (1961).

21. Warneck, P., J. Chem. Phys. 46, 502 (1967).

22. Gorden, R. and Ausloos, P., J. Chem. Phys. 47, 1799 (1967).

23. Field, F. H., J. Am. Chem. Soc. 83, 1523 (1961); Wexler, S., A. Lifshitz, and A. Quaffrochi, Advan. Chem. Ser. 58, 193 (1966); Wexler, S. and J. Marshall, J. Am. Chem. Soc. 86, 781 (1964).

24. Botter, R., V. H. Dibeler, J. Walker and H. M. Rosenstock, J. Chem. Phys. 45, 1298 (1966).

25. Brehm, B., Z. Naturforsch, 21a, 196 (1966).

26. Schoen, R. I., J. Chem. Phys. 37, 2032 (1962).

27. Poschenrieder, W. P. and P. Warneck. J. Appl. Phys. 37. 2812 (1966).

28. Poschenrieder, W. P. and Warneck, P., Anal. Chem. 40. 385 (1968).

29. Dibeler, V. H., M. Krauss, R. M. Reese, and F. N. Harlee . J. Chem. Phys. 45, 1287 (1966).

30. Chupka, W. A., J. Chem. Phys. 48. 2337 (1968).

31. Watanabe. K., T. Nakayama. J. Mottl, J. Quant. Spectry. Radiat. Transfer 2, 369 (1962).

32. Herzberg, G., Proc. Roy. Soc. (London) A262 (1961)

33. Matthews, C. S. and P. Warneck. J. Chem. Phys. 51. 854 (1969).

34. Haney, M. A. and J. L. Franklin, Trans. Faraday Soc. 65. 1794 (1969).

35. Skinner, H. A. (Private communication).

36. Kerv, J. A., Chem. Rev. 66. 465 (1966).

37. Marmo, F. F. and Warneck, P. Final Report Contract NASw-1283, GCA Technical Report No. 68-7-N.

38. Warneck, P. J. Chem. Phys. 46. 513 (1967).

39. Huxley, L. G. H. and Crompton, R. W. in Atomic and Molecular Processes, ed. D. R. Bates, Academic Press, New York (1962) p. 337.

40. Biondi, M. A. and Chanin, L. M., Phys. Rev. 94, 910 (1954).

41. Beaty, E. C., Proc. Fifth Int. Conf. on Ionization Phenomena in Gases (North Holland Publishing Co., Amsterdam, 1961).

42. McAfee, K. B., Sipler, D. and Edelson, D., Phys. Rev. 160, 130 (1967)

43. Madson, T. M. and Oskam, H. J. Physics Letters 25A, 407 (1967).

44. Saporoschenko, M. Phys. Rev. 139A, 352 (1965).

45. Keller, G. C., Martin. D. W. and McDaniel, E. W., Phys. Rev. 140A, 1535 (1965).

46. Ogawa, M. and Tanaka, Y., Can. J. Phys. 40. 1593 (1962).

47. Samson, J. A. R. and Weissler, G. W., Phys. Rev. 137A, 381 (1965).

48. Varney, R. N., Phys. Rev. 89, 708 (1953).

49. U. S. Standard Atmosphere Supplements, 1966

50. Marmo, F. F., GCA Final Report NASW-1283 (July, 1968)

51. Schultz, E. D. and Holland, A. C., GCA TR 62-14-N (November, 1962)

52. Sullivan, J. O. and Holland, A. C., GCA TR 64-16-A (December, 1964)

53. Marmo, F. F., Quarterly Progress Report No. 1, NASW-1726, (August, 1968)

54. Chamberlain, J. W., Physics of the Aurora and Airglow, Academic Press, New York (1961)

55. Noxon, J. F. and Goody, R. M., Journal of Atmospheric Science, 19, 342 (1963)

56. Donahue, T. M., et al, Journal of Geophys. Res. 72, No. 11, 2803 (1967).

57. Narcisi, R. S., Cospar, Space Research VIII, Editors, Mitra, A. P., Jacchia, L. G. and Newmann, W. S., North Holland Publishing Co., Amsterdam (1967).

58. Vallance Jones, A., Planetary and Space Science, 10, 117 (1963).

59. Marmo, F. F. and Brown, H. K., GCA TR 63-4-N (March, 1963)

60. Aller, L. H., The Abundance of the Elements, Vol. VII, pps. 54-55 and 122-123, Interscience Publishers, Inc., New York (1961)

61. Allen, C. W., Astrophyskcal Quantities, Second Edition, Athlane Press, London (1963).

62. Marmo, F. F., et als, GCA TR 65-13-N (June, 1965)

63. Chamberlain, J. W. and Sobouti, Y., Astrophysical Journal, 135, 925 (1962)

64. Chandrasekhar, S., Radiative Transfer, Dover Publications, New York (1960)

65. Barth, C. A. U V Spectroscopy of Planets, JPL TR No. 32-822 (December 15, 1965)

66. Inn, E. C., Journal of Atmospheric Sciences, 21, 220 (1964).

67. Mahan, B. H. and Solo, R. B., Journal of Chemical Physics, 37, No. 11, 2669 (1962).

68. Clyne, M. A. A. and Thrush, B. A., Proc. Roy. Soc. 269A, 404 (1962).

69. Marmo, F. F. and Warneck, P., Quarterly Progress Report No. 4, NASW-840 (October 15, 1964)

70. Belton, M. J. S. and Hunten, D. M., The Astrophysical Journal, 153, 963 (1968)

71. Jonathan, N., and Doherty, G., GCA TR 63-1-N (February, 1963)

72. Evans, D. C., Science, 149, 969 (1965)

73. Calvert, J. G. and Pitts, J. N. Jr., Photochemistry, Wiley and Sons, Inc., New York (c.1966)

74. Cadle, R. D., Particles in the Atmosphere and Space, Rienhold Publishing Corporation, New York (1966).

75. Chapman, S., J. Atmos. Terr. Phys. 1, 121 (1950).

76. Spitzer, L. "Atmosphere of the Earth and Planets," (Ed. by G. P. Kuiper) p. 213, Chicago University Press.

77. Bates, D. R., Proc. Phys. Soc. (London) B64, 805 (1951).

78. Bates, D. R. Proc. Roy. Soc. (London) A236, 206 (1956).

79. McElroy, M. B., Ecuyer, J. L., and Chamberlain, J. W., Astrophys. J., 141, 1523 (1965).

80. Hunt, D. C., and Van Zandt, T. E., J. Geophys. Res. 66, 1673 (1961).

81. Mitchell, A. C. H., and Zemansky, M. W., Resonance Radiation and Excited Atoms, Cambridge University Press (1934).

82. Texas Instruments Scientific Instrument Product Bulletin C163.

84. Soberman, R. K., "Meteoritic Phenomena," USAF Handbook of Geo-Physics and Space Environment (ed. S. L. Valley), Ch. 14, AFCRL, Bedford, Massachusetts (1965).

85. Hawkins, G. S., "Interplanetary Debris near the Earth," Ann. Rev. Astron. & Astrophys. (ed. L. Goldberg, et al.) 2, 149 (1964).

86. Opik, E. J., "Interplanetary Dust and Terrestrial Accretion of Meteoric Matter," Irish Astron. J. 4, 84 (1956).

87. Hemenway, C. L. and Soberman, R. K., "Studies of Micrometeorites Obtained from a Recoverable Sounding Rocket," Astron. J. 67, 256 (1962).

88. Soberman, R. K. and Hemenway, C. L. "Meteoric Dust in the Upper Atmosphere," J. Geophys. Res. 70, 4943 (1965).

89. Shaffir, U. and Humi, M. "The Dynamical Interaction of Small Interplanetary Particles with the Earth's Upper Atmosphere, Paper presented at the International Symposium on the Study of Noctilucent Clouds as Indicators of Processes in the Upper Atmosphere, Tallinn, Estonian, SSR, March, 1966.

90. Shaffir, U. and Humi, M. "Interplanetary Particles and Noctilucent Clouds," J. Atmospheric Sci. 24, 577 (1967).

91. Shaffir, U., Abarbanel, S. and Humi, M. a note on the "Dynamical Interaction of Small Interplanetary Particles with the Earth's Upper Atmosphere," J. Atmospheric Sci. 24, 582 (1967).

92. Carr, M. and Gabe, H. J., "Micrometeorite Flux Determined from the 1967 Luster Sounding Rocket Collection," J. Geophys. Res. 72, 4007 (1967).

93. Gerloff, U., "Electron Microscopic Investigations to Collect and Analyze Chemically Cosmic Dust Particles," Ph.D. thesis, Ruprecht-Karl University, Grabengasse 1, Heidelberg (1966).

94. Weihrauch, J., "Collecting of Cosmic Dust with Luster Rockets and Gemini Satellites, Ph.D. tehsis, Ruprecht-Karl University, Grabengasse 1, Heidelberg, (1967).

95. Greenman, N. N., Asurmaa, S. K. and Ingersoll, R. G., "Study of Particles Collected by the 1966 Luster Rocket (Luster II), Final Report, Douglas Aircraft Tech. Rept. DAC62220, (April, 1968).

96. Whipple, F. L., "The Theory of Micrometeorites, Part I, In an Isothermal Atmosphere," Proc. Nat. Acad. Sci. 36, 687 (1950).

97. Whipple, F. L., "The Theory of Micrometeorites, Part II, In Heterothermal Atmospheres," Proc. Nat. Acad. Sci. 37, 19 (1951).

98. Whipple, F. L. and Hawkins, G. S. "Meteors," Handbuch der Physik , Band LII, Astrophysik III: Das Sonnen System,, (ed. S. Flugge), Springer-Verlag. Berlin (1959).

99. Allen, H. J., Baldwin, B. S. Jr.. and James, N. A., "Effect on Meteor Flight of Cooling by Radiation and Ablation," NASA Tech. Note TN D-2872 (1965).

100. Levin, B. I., Physical Theory of Meteors and Meteoric Matter in the Solar System, Ch. I-III, translated from Russian to German by N. Ricter, Academi-Verlag. Berlin (1961).

101. Herlofson, N., "The Theory of Meteor Ionization," Phys. Soc. Rep. Prog. Phys. 11, 444 (1948).

102. Opik, E. J., Physics of Meteor Flight in the Atmosphere, Interscience Pulb., Inc., N. Y. (1958).

103. Weiss, A. A., "Theory of the Radio-Echo Meteor Height Distribution in a Non-Isothermal Atmosphere," Austral. J. Phys. 12, 54 (1959).

104. Verniani. F., "On Meteor Ablation in the Atmosphere," Nuovo Cimento 19, 415 (1961).

105. Hawkins, G. S., Meteors, Comets and Meteorites, McGraw-Hill, New York (1964).

106. McKinley, D. W. R., Meteor Science and Engineering, McGraw Hill, New York (1961).

107. Verniani, F., "On the Density of Meteoroids II. The Density of Faint Photographic Meteors," Nuovo Cimento 33, 1173 (1964).

108. Jennison, R. C. and McDonnell, J. A. M. "Interpretation of the Interplanetary Dust Measurements in the Ariel II Satellite," Space Research VI (ed. R. L. Smith-Rose) Spartan Books, Washington, D. C. (1966).

109. Eshleman, V. R. and Gallagher, P. B., "Radar Studies of 15th-Magnitude Meteors," Astron. J. 67, 245 (1962).

110. Fialko, Ye. I., "On the Velocity Distribution of Meteoroids," Astron. Zhurn, 37, 354 (1960).

111. Verniani, F., "Physical Characteristics of 320 Faint Radio Meteors," J. Geophys. Res. 71, 2749 (1966).

112. McElroy, M. B., "The Upper Atmosphere of Venus," J. Geophys. Res. (in preparation) March (1968).

113. House, F., Ohring, G., Sherman, C., and Tang, W. "Study of the Martian Atmospheric Environmental Requirements for Spacecraft and Entry Vehicles," GCA-TR-67-12-G, GCA Corp., Bedford, Mass. (1967).

114. Dubin, M., "Meteor Ionization in the E-Region," in Meteors (ed. T. R. Kaiser), Special Suppl. (Vol. II) to the J. Atmos. Terres. Phys., p. 111, Pergamon Press, New York (1955).

115. Marmo, F. F. and Borwn, H. K., "Planetary Aeronomy XII: The Role of Interplanetary Debris in Planetary Atmospheres: 1. Sodium in theEarth's Atmosphere," GCA Tech. Rept. 63-4-N, GCA Corp, Bedford, Massachusetts (1963).

116. Narcissi, R. S., "Ion Composition Measurement and Related Ionosphere Processes in the D and Lower E-Region," Aeronomy Report #10, 2nd Conference on Direct Aeronomic Measurements in the Lower Ionosphere, December, 1965.

117. McElroy, M. B., "Structure of the Venus and Mars Atmospheres," J. Geophys. Res. 74, 29-41 (1969).

118. Bahr, J. L., A. J. Blake, J. H. Carver, and Vijay Kumar, "Photoelectron Spectra and Partial Photoionization Cross Section for Carbon Dioxide," University of Adelaide (Australia) Report ADP 67. January, 1969.

119. Henry, R. J. W. and M. B. McElroy, "Photoelectrons in Planetary Atmospheres." in The Atmosphere of Venus and Mars, Edited by J. C. Brandt and M. B. McElroy, Gordon and Breach Publishers, New York/ London, 1968.

120. Sytinskaya, N. N., The Moon, edited by A. V. Markov, University of Chicago Press (1962.

121. Lyot, B. and Dollfus, A., Compt. Rend. Acad. Sci., Paris, 220, 1173 1969

122. Dollfus, A. Compt. Rend. Acad. Sci., Paris, 234, 2046 (1952).

123. Elsmore, B. Phil. Mag. 2, 1040 (1957).

124. Herzberg, G., Pop. Ast. 54, 414 (1946).

125. Kuiper, G. P., The Atmospheres of the Earth and Planets, edited by G. P. Kuiper, University of Chicago Press, Chicago (1952).

126. Marmo, F. F. and Engelman, A., Ann. of the N. Y. Acad. of Sci. 140, 69 (1966).

127. Marmo, F. F. and Manring, E., "Measured Maximum Abundances of Na I, Ca I and Ca II in the Lunar Atmosphere," The Moon (D. Reidel Publishing Company, submitted for publication).

128. Michel, F. C., "Interaction between the solar wind and the lunar atmosphere," Plan. Space Sci. 12, #11, 1075 (1964).

129. Mirtov, B. A., "Materials of the Lunar Surface in the Lunar Atmosphere," Geomagnetism i Aeron. 9, #1. 143 (1969).

130. Herzog, L. F., et al, "The Analysis of the Lunar Atmosphere by a Mass Spectroscope." Technical Report under Contract No. NASw-1480 (1968).

131. Hinten, F. L. and Taeusch, D. F., "Variation of the Lunar Atmosphere," J. Geophys. Res., 69, 1341 (1964).

132. Jursa, A., etals, "Nitric Oxide and Molecular Oxygen in the Earth's Upper Atmosphere." Planetary and Space Sci., 1, 161 (1959).

133. Certified Precision Diffraction Gratings, Bausch and Lomb (April. 1968)

134. Lewis, W. C. and James, T. H., "Effects of Evacuation on Low Intensity Reciprocity Failure and on Desensitization by Dyes." Photo. Sci. and Engineering, 13, #2, 54 (1969).

135. Fowler, W. K., Rense, W. A. and Simmons, W. R., "Film Calibration for Rocket Ultraviolet Spectrographs." Applied Optics, 4, #12, 1596 (1965).

136. Fowler, W. K. (private communication).